

**Controlling  
the Magnetic Anisotropy  
in Ultrathin Metallic Films**

**Jan Kisielewski**

---

Copyright © 2013, by Jan Kisielewski

Printed by Ipskamp Drukkers B.V., Enschede, The Netherlands  
ISBN 978-94-6191-776-8

# Controlling the Magnetic Anisotropy in Ultrathin Metallic Films

**Doctoral thesis**

to obtain the degree of doctor  
jointly awarded by  
Radboud University Nijmegen  
on the authority of the Rector Magnificus prof. dr. S.C.J.J. Kortmann,  
according to the decision of the Council of Deans,  
and  
University of Białystok,  
on the authority of the Rector Magnificus prof. dr. hab. L. Etel,  
according to the decision of the Council of the Faculty of Physics,  
to be defended in public on Thursday, July 4, 2013  
at 10.30 hours

by

**Jan Kisielewski**

born on 15 April 1982  
in Pruszków, Poland





*to my wife, Monika*



---

## Preface

---

That was a good time... During the joint PhD studies, in Nijmegen and in Białystok, I have learned a lot, scientifically, personally and generally. Now this important chapter of my life is approaching its end. This is a perfect moment to look back and appreciate all the people who created this chapter with me.

First of all, I would like to thank my supervisors, prof. Theo Rasing, prof. Andrzej Maziewski and prof. Andrei Kirilyuk. Theo, thanks for giving me an opportunity to belong to your excellent group, for sharing your knowledge and experience with me, for a patient feedback to all my abstracts, posters, papers and finally the thesis. Thank you! Andrzej, thanks for offering me a position in your group just after my master studies, for teaching me science, physics, magnetism, for involving me in numerous projects – especially for initializing the idea of these joint PhD studies. For your patience and for stimulating my scientific career. Thank you! Andrei, thanks for fruitful discussions about principles of physics, planning experiments and interpretation of results. For teaching me the way of presenting the data, and particularly for forcing me to ask questions “why?”. Thank you! Thanks also to my co-supervisor, dr. Alexei Kimel, as well as my unofficial co-supervisor, dr. Andrzej Stupakiewicz. Alexei, Andrzej, thank you for your interest in my scientific progress and for your help with planning and carrying out my works.

Experimental research usually requires a big group of people. I am very grateful to those who helped me with all the issues connected with my experimental works, configuring the experimental set-ups, performing the measurements, as well as analyzing the data afterward: Albert van Etteger, Tonnie Toonen, André van Roij, Sam Khorsand, Ilie Radu, Maria Tekielak, Kamil Postava, Wojtek Dobrogowski, Zbigniew Kurant, Josif Sveklo, Piotr Mazalski and Paweł Trzciński, and also to Andrzej

Wawro and Lech Tomasz Baczewski from Polish Academy of Sciences, who prepared nice samples. Thanks a lot to all of you! You have a significant contribution to this work.

I would like also to thank to the people, who directly contributed to improving this thesis. Beside an inestimable impact of the supervisors and co-supervisors, I thank prof. Jacques Ferré and prof. Henryk Szymczak from my doctoral thesis committee. I really appreciate your comments and positive criticism. Thank you! Thanks also to Benny Koene, for a great help with Samenvatting. Thanks a lot!

During my PhD studies, especially for their joint character, there were a plenty of complicated formal issues to solve. Nevertheless, it was always possible with the secretary, Marilou de Wit. Marilou, thanks for your patient help in all of my endless "I have a question...". I received also a significant help in this field from Wiesiek Szweryn. Many thanks for teaching me the Dutch taxes, insurances, and other social and formal rules. Dziękuję!

Many thanks to all, with whom I met every day during my stay in Nijmegen. Addis, Alex, Asha, Bas, Benny, Boldizsar, Bowen, Chris, Davide, Dennis, Diana, Dima A., Dima M., Duncan, Ewelina, Fred, Hans, Ilie, Ilya, Jelena, Jeroen, Jing, Johan dJ., Johan M., Jonas, Joost, Joris, Jos, Kadir, Koen, Lars, Laura, Magnus, Marie-Louise, Mathieu, Matteo, Michiel, Minko, Monique, Oleg, Pieter, Raja G., Rajasekhar, Ruslan, Sam, Sasha, Sergey, Serhiy, Shoken, Siebe, Tahoor, Thomas, Wei-Ta, Weizhe and Yusuke, thank you for your friendliness and for any help in all minor and major issues. Thank you also for all events, like karting, bowling, playing football and volleyball, going out and drinking together. Many thanks also to all of my colleagues from Białystok. Andrzej, Josif, Jurek, Marek, Maria, Mikhail, Nadeem, Piotr, Ryszard, Sergii, Ula, Vladimir, Wiktor, Wojtek, Zbyszek, thank you for everything!

Finally I would like to thank all of my family and friends, for their support and care. Particularly I thank my wife Monika. Dziękuję za to, że jesteś, za wielkie wsparcie, za cierpliwość i siłę w czasie rozłąki. Kocham Cię!

**All of you, thank you very much!**

Jan Kisielewski

Białystok/Nijmegen, May 2013

---

# Contents

---

<b>1</b>	<b>Introduction</b>	<b>1</b>
1.1	Magnetization . . . . .	2
1.1.1	Temperature dependence . . . . .	2
1.1.2	Ultrafast demagnetization . . . . .	3
1.1.3	Magnetization and magnetic field . . . . .	4
1.1.4	Magnetization precession . . . . .	6
1.2	Magnetic anisotropy . . . . .	8
1.2.1	Anisotropy energy . . . . .	8
1.2.2	Ultrathin films . . . . .	9
1.2.3	Anisotropy field . . . . .	12
1.2.4	Preferred magnetization orientation . . . . .	12
1.3	Scope of the Thesis . . . . .	14
	References . . . . .	14
<b>2</b>	<b>Modifying the magnetic anisotropy</b>	<b>17</b>
2.1	Samples composition . . . . .	18
2.1.1	Interface anisotropy . . . . .	18
2.1.2	In-plane anisotropy . . . . .	21
2.2	Reversible modification . . . . .	21
2.2.1	Magnetic anisotropy vs. temperature . . . . .	21
2.2.2	Photo-induced anisotropy . . . . .	24
2.3	Irreversible modification . . . . .	24
2.3.1	Laser processing . . . . .	24
2.3.2	Ion-irradiation . . . . .	25

References . . . . .	26
<b>3 Experimental techniques</b>	<b>33</b>
3.1 Samples preparation . . . . .	34
3.2 Magneto-Optical Kerr Effect . . . . .	35
3.3 Kerr microscopy . . . . .	37
3.4 Kerr milli-magnetometer . . . . .	41
3.5 Time-resolved magneto-optical setup . . . . .	44
References . . . . .	47
<b>4 Ultrafast manipulation of magnetic anisotropy</b>	<b>49</b>
4.1 Experimental details . . . . .	50
4.2 Results . . . . .	52
4.3 Calculations . . . . .	53
4.3.1 Role of temperature . . . . .	55
4.3.2 Magnetization precession . . . . .	57
4.4 Discussion . . . . .	59
References . . . . .	68
<b>5 Manipulating the magnetic anisotropy by laser annealing</b>	<b>69</b>
5.1 Experimental details . . . . .	70
5.2 Quasi-continuous pulse laser annealing of Au/Co/Au structure . . . . .	72
5.3 Continuous laser annealing of Pt/Co/Pt structure . . . . .	77
5.4 Single pulse laser annealing of Pt/Co/Pt structure . . . . .	79
5.4.1 Remanence images of annealed magnetic structures . . . . .	79
5.4.2 PMOKE hysteresis curves . . . . .	82
5.4.3 LMOKE hysteresis curves . . . . .	87
5.4.4 Energy density profiles . . . . .	89
5.4.5 Phase diagrams . . . . .	90
5.4.6 Summary . . . . .	97
5.5 Discussion . . . . .	98
References . . . . .	102
<b>A Analysis of magneto-optical images</b>	<b>105</b>
A.1 Drift . . . . .	106
A.2 Inhomogeneity of illumination . . . . .	106
A.3 Influence of magnetic field on microscope objective . . . . .	108
References . . . . .	111

---

<b>B</b>	<b>Beam size determination</b>	<b>113</b>
B.1	Liu's method . . . . .	113
B.2	Knife-edge method . . . . .	115
	References . . . . .	119
<b>C</b>	<b>Calculations of laser-induced temperature dynamics</b>	<b>121</b>
C.1	Absorbed energy . . . . .	122
C.2	Temperature increase . . . . .	123
C.3	Heat equation . . . . .	124
	C.3.1 Perpendicular heat transfer . . . . .	125
	C.3.2 Planar heat transfer . . . . .	126
	References . . . . .	127
	<b>Summary</b>	<b>129</b>
	<b>Samenvatting</b>	<b>131</b>
	<b>Streszczenie</b>	<b>133</b>
	<b>List of Publications</b>	<b>135</b>
	<b>Curriculum Vitae</b>	<b>137</b>





# CHAPTER 1

---

## Introduction

---

Magnetism has been known for millennia. Years ago people wondered, why some pieces of stone attracted each other. They also wondered, why that piece of stone could spontaneously and magically orient with respect to the world's cardinal points. That observation was in fact crucial for the World's history, nevertheless compasses stayed the only practical use of magnetism until the 19th century. Serious studies on magnetism started with discoveries of Ørsted, Biot, Savart, Ampère, Maxwell and Faraday, who brought magnetism to life as a discipline of physics. Since that time magnetism has grown into a large tree, with numerous branches spreading over physics, as well as chemistry, biology and medicine.

As this Thesis modestly hopes to contribute to that tree as one of its leaves, in this very first chapter some basic ideas and definitions of magnetism will be reviewed, as a background for the Thesis. We discuss the basics of magnetization, magnetic fields and magnetic anisotropy, with a more detailed look at ultrathin films. At the end, we present the scope of the Thesis.

## 1.1 Magnetization

To describe magnetic phenomena and properties usually quantum physics is required. Electrons in atom possess spin and orbital angular momentum, adding up to the total angular momentum. The *magnetic moment* of an atom, classically treated as a loop with a current, according to quantum physics is proportional to that effective angular momentum. The unit of the magnetic moment is the *Bohr magneton* ( $\mu_B$ ), that corresponds approximately to the unitary total angular momentum. Macroscopically, the total magnetic moment per unit volume is called *magnetization*.

There is a relatively small group of materials, that exhibit spontaneously an alignment of their magnetic moments. They belong to one of the classes of magnetic materials: *ferromagnets*, *ferrimagnets* and *antiferromagnets*. In ferromagnetic materials the magnetic moments are aligned parallel. The ferrimagnetic materials are characterized by the existence of at least two ferromagnetic sublattices with a different magnetization, oriented in opposite directions. The antiferromagnetic media also consist of ferromagnetic sublattices, oriented in opposite directions, so that the total magnetization vanishes.

A dominant mechanism, that rules the alignment of the magnetic moments is the *exchange interaction*. This is a purely quantum effect, resulting from the Pauli exclusion for overlapping wave functions of interacting electrons. Depending on the sign of the *exchange integral*, a parallel (for a positive sign) or an anti-parallel (for a negative) orientation of spins may be preferred.

### 1.1.1 Temperature dependence

Thermal fluctuations tend to destroy the magnetic alignment, and therefore magnetic moments can stay ordered in a limited range of temperatures only. The magnetization of the ferromagnets decreases with increasing temperature to vanish at a critical temperature, called the *Curie temperature*,  $T_C$ . An analogous temperature for the antiferromagnets is called the *Néel temperature*,  $T_N$ . Above the  $T_C$  or  $T_N$  all respective materials become *paramagnetic*. The temperature dependence of the magnetization can be described with the Brillouin function  $B_J(x)$ , depending on the total angular momentum  $J$  of the magnetic atoms [1, 2]. The original derivation by Léon Brillouin concerned spins that were quantized in two orientations, i.e. for  $J = s = 1/2$ , and in fact the ferromagnetic metals, like Fe, Co, Ni follow closely this theory [1]. The earlier “macrospin” approximation by Paul Langevin (without a quantization assumed) agrees with the  $B_\infty(x)$  curve. The temperature dependence of the magnetization calculated with  $B_{1/2}(x)$  and  $B_\infty(x)$ , as well as the experimental one for bulk Co, taken from Ref. [3], are plotted in Figure 1.1.

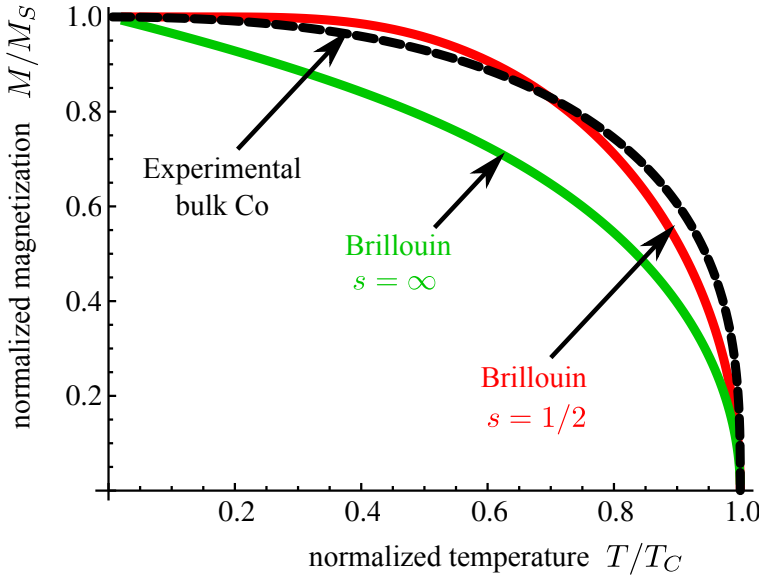


**Figure 1.1:** The temperature dependences of the magnetization, calculated with the Brillouin function, for the cases of  $B_{1/2}(x)$  and  $B_{\infty}(x)$  and measured for bulk Co [3].

### 1.1.2 Ultrafast demagnetization

According to the temperature dependence of the magnetization presented above, heating a magnetic material leads to reducing the magnetization length, i.e. *demagnetization* occurs. As long as the heating process is slow, the magnetization just follows the temperature changes of the material in a thermodynamic equilibrium. This process becomes more interesting, when the heating is very fast, faster than the interaction between the electrons and the lattice. At these conditions, certain non-equilibrium states in a material can be observed. Such processes can be realized with intense femtosecond laser pulses – in metals the absorption of the light is always accompanied by a redistribution of the energy over many degrees of freedom, which results in an increase of temperature.

The simplest description of the ultrafast heating of a material is the two-temperature model (2TM) [4, 5], which assumes an existence of two baths, electrons and the lattice. The baths have individual temperatures, individual heat capacities, they respond on different time scales and they are coupled to each other. The electrons are the ones which absorb the energy directly from the laser pulse on a time scale of tens of femtoseconds. Next they thermalize with the lattice, which is ruled by the electron-lattice coupling parameter and happens for metals on a few-picoseconds time scale.

In the case of magnetic materials, the magnetization is also involved in such ultrafast dynamics. Beaurepaire et al. [6] were the first who showed the ultrafast demagnetization process, induced by heating a ferromagnetic Ni film with an intense laser pulse of 60 fs duration. This result was very unusual, as the temporal behavior of the magnetization was much faster (several orders of magnitude) than any spin dynamics in a metallic ferromagnet reported before. To describe the system, they enriched the 2TM with the third temperature of the spins bath and the two extra electron-spin and spin-lattice coupling parameters. Using this 3TM they estimated the temperature dynamics of the electrons, the spins, and the lattice, resolving for the first time the effects of electron-spin and spin-lattice relaxations. The temporal dependence of the magnetization of the excited Ni film on a time scale of a few picoseconds, taken from their original paper, is presented in Figure 1.2. Figure 1.3 shows a comparison of the measured and calculated temperature dynamics of the electrons, spins and lattice.

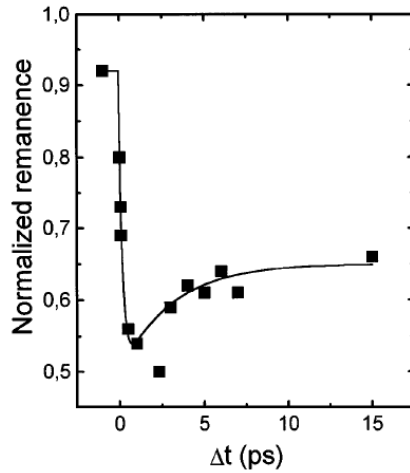


**Figure 1.2:** Ultrafast demagnetization process in an ultrathin Ni film, reported by Beaurepaire et al. [6].

### 1.1.3 Magnetization and magnetic field

A magnetic field acts on the magnetization, which can be expressed with the Zeeman's formula for the energy of that interaction:

$$E_Z = -\mu_0 \mathbf{M} \cdot \mathbf{H} = -\mu_0 M H \cos \theta_{\{\mathbf{M}, \mathbf{H}\}}. \quad (1.1)$$

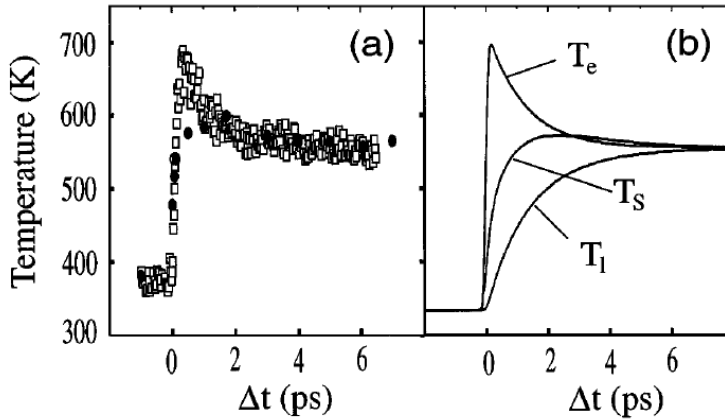


**Figure 1.3:** Dynamics of the electrons, spins and lattice temperatures, induced by 60 fs laser pulse, measured and calculated within the three-temperature model, reported by Beaurepaire et al. [6]

$\theta_{\{\mathbf{M}, \mathbf{H}\}}$  is the angle between the vectors  $\mathbf{M}$  and  $\mathbf{H}$ . A minimum of the energy corresponds to the parallel orientation of those vectors, i.e. the magnetization tends to orient along the magnetic field direction.

The behavior of a ferromagnetic sample in a magnetic field is usually studied probing one component of the magnetization as a function of the amplitude of the external magnetic field, applied along a certain direction – this way a *magnetization curve* is recorded. As a general rule, the magnetization state at certain conditions is determined by the minimal energy of the system – including Zeeman’s energy, as well as several other contributions, broadly discussed in the following Sections.

Magnetization may respond to the applied field in various ways, yielding in a broad variety of magnetization curve shapes. Some concrete mechanisms will be presented later, nevertheless to characterize a given curve, some useful parameters are often determined. The *saturation field*  $H_S$  is the field that is strong enough to overcome all other forces and to align all the magnetic moments along its direction. The sample is called to be *saturated* then (a  $M_S$  state). Decreasing the field to 0 there can remain some non-zero magnetization – this state is called a *remanence*,  $M_R$ . To make the magnetization equal to zero, some negative *coercive field*,  $H_C$  may be required. Applying  $-H_S$ , the sample becomes saturated in the opposite direction. However, increasing the field back to  $+H_S$ , the magnetization may follow not the same path, but one symmetrical to the previous one. Thus, the actual magnetization state depends on the sample’s history and in that sense the magnetization curve is often called a

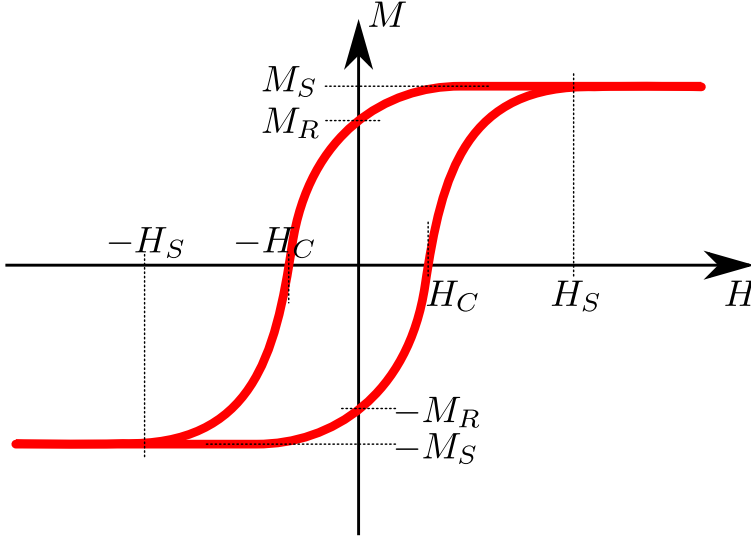


**Figure 1.4:** A general shape of the hysteresis curve of a bulk magnetic material, illustrating the meanings of the relevant parameters: saturation  $M_S$ , remanence  $M_R$ , coercive field  $H_C$  and saturation field  $H_S$ .

*hysteresis curve.* The meanings of the mentioned parameters are illustrated in Figure 1.4, with a “typical” shape of the hysteresis curve.

The process of magnetizing materials costs some energy, that is partially deposited as a potential energy of the magnetized media, and partially dissipated, what appears as heat. The heat or energy, that is lost in a one full cycle of the hysteresis loop, is called the *hysteresis loss*, and is proportional to the area inside the loop.

### 1.1.4 Magnetization precession

Homogeneous magnetic field interacts with a magnetic dipole  $\mathbf{m}$ , exerting a torque  $\mathbf{T} = \mathbf{m} \times \mathbf{H}$ , which affects the angular momentum vector  $\mathbf{L}$ , according to the classical Newton’s equation  $d\mathbf{L}/dt = \mathbf{T}$ . As the magnetic moment is connected to the angular momentum, the dynamics of the magnetic moment in the presence of the torque is ruled by the equation:

$$\frac{d\mathbf{m}}{dt} = \gamma \mathbf{T} = \gamma \mathbf{m} \times \mathbf{H}, \quad (1.2)$$

with the gyromagnetic ratio  $\gamma$  defined by

$$\gamma = -\frac{eg\mu_0}{2m_e}, \quad (1.3)$$

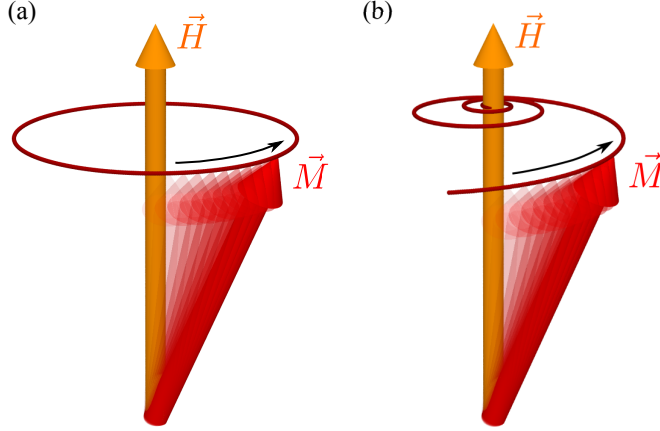


**Figure 1.5:** Precessional motion of the magnetization  $\vec{M}$  around direction of magnetic field  $\vec{H}$ : (a) an ideal case with no damping, described by Eq. (1.2); (b) attenuated precession, described by Eq. (1.4).

with the electron's charge  $e$  and mass  $m_e$ , vacuum permeability  $\mu_0$ , and the factor  $g$ . For the electron spin  $g = 2$ , for pure metals  $g$  deviates from 2 due to an orbital contribution to the magnetic moment (e.g. for Co  $g = 2.18$ ). Because  $\mathbf{T}$  is perpendicular to both  $\mathbf{m}$  and  $\mathbf{H}$ , the dynamics of the magnetic moment, i.e. the solution of the differential equation (1.2), is a precessional motion around the direction of  $\mathbf{H}$ . The frequency of the precession is proportional to the magnetic field amplitude,  $f = -\gamma H/2\pi$ , and typical values (for typical laboratory fields up to 1 T) are up to tens of gigahertz. The precessional motion is schematically shown in Figure 1.5(a). In reality there is always some damping, forcing the magnetization to orient along the field direction. It can be included by adding a damping term to Eq. (1.2). An extra torque should act towards the direction of  $\mathbf{H}$ , i.e. it should be perpendicular to both  $\mathbf{m}$  and  $\mathbf{T}$ :

$$\frac{d\mathbf{m}}{dt} = \gamma(\mathbf{m} \times \mathbf{H}) + \frac{\alpha}{|m|} \left( \mathbf{m} \times \frac{d\mathbf{m}}{dt} \right) \quad (1.4)$$

This equation is called the *Landau-Lifshitz-Gilbert* equation (LLG), originally presented in 1935 by Landau and Lifshitz [7] in a slightly different form, and later modified by Gilbert [8], to be able to describe correctly the dynamics with large damping.  $\alpha$  is called a dimensionless *Gilbert damping parameter*. The damped precession is shown schematically in Figure 1.5(b). Both Eqs. (1.2) and (1.4) describe the dynamics of a single magnetic moment. However, in the case of homogeneous behavior of all magnetic moments in the sample, one can use the magnetization vector  $\vec{M}$  instead of  $\mathbf{m}$  as well.

## 1.2 Magnetic anisotropy

Anisotropy is related to the fact that a property of matter or space depends on direction. Because of crystal structure and the presence of surfaces or interfaces, strains, etc., the properties of materials become anisotropic, which may also influence the magnetization.

### 1.2.1 Anisotropy energy

The spins of electrons are coupled to each other with the exchange interaction, which is isotropic. However, the spins are also coupled to the orbital angular momenta via the *spin-orbit interaction* [9]. Electron orbitals in crystals are bound by a periodical structure of the lattice, in particular the orbitals of neighboring atoms may overlap and even lead to a quenching of the orbital moment. Through the spin-orbit coupling the spins also favor some directions in space – a parallel mutual orientation of spins and orbital angular momenta is preferred rather than perpendicular.

This is the origin of the *magnetocrystalline anisotropy*, whose symmetry is the same as of the crystal structure. The magnetocrystalline anisotropy is defined by the energy it takes to rotate the magnetization from a preferred *easy direction* to a *hard direction*. That energy is given by a difference of the spin-orbit energies at each of those orientations. According to the *Bruno model* of the anisotropy [10], it is further proportional to the difference between the orbital moments along the easy and hard directions (the orbital moment is larger along the easy magnetization direction).

Microscopically it is usually difficult to calculate, so for a macroscopic treatment it is more useful to define the anisotropy energy by an expansion of trigonometric functions that determine the symmetry of the lattice, with phenomenological coefficients. In the case of cubic symmetry this gives:

$$E_{\text{cub}} = K_0 + K_1 (\alpha_1^2 \alpha_2^2 + \alpha_2^2 \alpha_3^2 + \alpha_1^2 \alpha_3^2) + K_2 \alpha_1^2 \alpha_2^2 \alpha_3^2 + \dots, \quad (1.5)$$

where  $\alpha_i$ 's are cosines of the angles between the magnetization vector and the axes of the Cartesian coordinate system ( $i = x, y, z$ ). If there is one specified symmetry axis of the structure, the *uniaxial anisotropy* can be used, with the anisotropy energy given by an expansion of even functions of  $\theta$ , the angle between the specified anisotropy axis and the magnetization, with phenomenological parameters  $K_i$ , called the anisotropy constants:

$$E_{\text{uni}} = K_0 + K_1 \sin^2 \theta + K_2 \sin^4 \theta + \dots, \quad (1.6)$$

Uniaxial anisotropy is usually a good approximation for hexagonal and tetragonal structures, and above all it is used for describing ultrathin film systems, therefore it is the most relevant for this Thesis.

The preferred magnetization orientation can be derived by minimizing the anisotropy energy. For the uniaxial anisotropy, with a  $K_1$ -only approximation, two cases can be



distinguished: for  $K_1 > 0$  the minimal energy corresponds to an axial orientation of the magnetization ( $\theta = 0^\circ$ , *easy axis*), for  $K_1 < 0$  on the contrary, the axial direction is *hard* and a planar orientation is preferred ( $\theta = 90^\circ$ , *easy plane*). Considering  $K_2$  too, the situation becomes more complicated, as for  $-2K_2 < K_1 < 0$  there is an *easy cone* state, i.e. the magnetization prefers to stay at some angle with the axis. On the other hand, for  $0 < K_1 < -2K_2$  two local minima exist, at  $\theta = 0^\circ$  and  $\theta = 90^\circ$ . Preferred magnetization states for uniaxial anisotropy, as a function of both  $K_1$  and  $K_2$  are shown as a phase diagram in Figure 1.6. Three-dimensional distributions of anisotropy energy, calculated according to Eq. (1.6), for certain values of  $K_1$  and  $K_2$ , are presented in Figure 1.7.

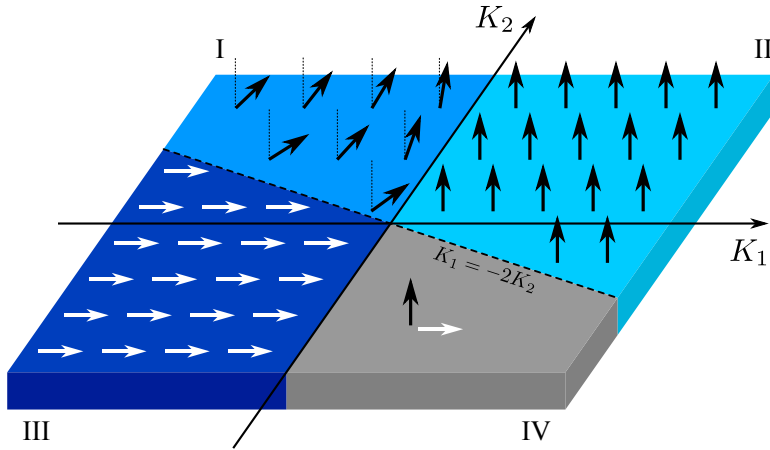


**Figure 1.6:** Preferred magnetization state for uniaxial anisotropy, as a function of  $K_1$  and  $K_2$ . Magnetization prefers to stay: perpendicularly to the plane, for  $K_1 > 0$  and  $K_1 > -2K_2$  (region II); in the plane, for  $K_1 < 0$  and  $K_1 < -2K_2$  (region III); making some angle with the axis, for  $-2K_2 < K_1 < 0$  (region I). For  $0 < K_1 < -2K_2$  (region IV) there are two local minima, so both  $\theta = 0^\circ$  and  $\theta = 90^\circ$  are preferred. Units of  $K_1$ ,  $K_2$  are arbitrary, as only the ratio between them is relevant for the diagram.

### 1.2.2 Ultrathin films

The shape of a sample can also impose a symmetry – this phenomenon is called *shape anisotropy*. The finite size of a sample leads to the existence of a *stray field* outside the sample, which results in the appearance of *demagnetizing field* inside the sample. If the shape of a sample is an infinite ultrathin plane, the stray field energy can be expressed as

$$E_{\text{dem}} = \frac{1}{2} \mu_0 M^2 \cos^2 \theta. \quad (1.7)$$

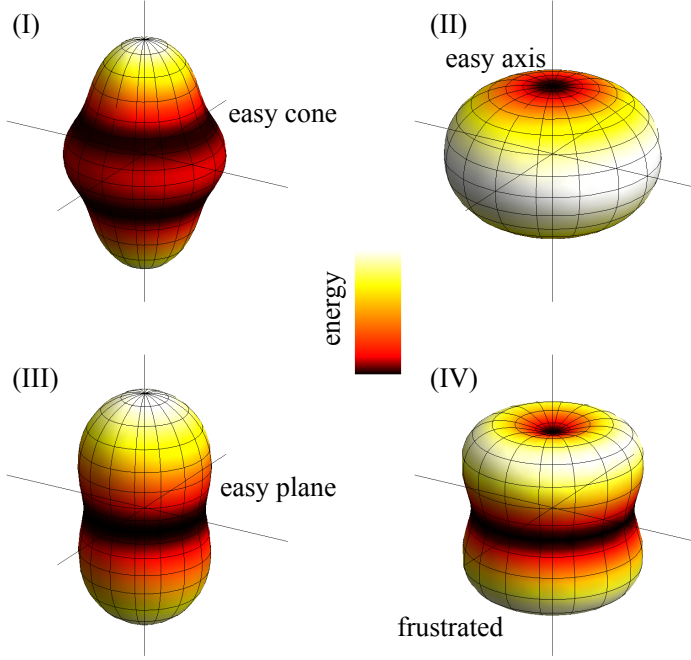


**Figure 1.7:** Distribution of the anisotropy energy, calculated for exemplary values of  $K_1$  and  $K_2$ , for four regions marked with Roman numbers in Figure 1.6: (I) easy cone state ( $K_1 < 0$ ,  $K_2 = -0.7K_1$ ); (II) easy axis state ( $K_1 > 0$ ,  $K_2 = 0$ ); (III) easy plane state ( $K_1 < 0$ ,  $K_2 = 0$ ); (IV) frustrated state with two local minima ( $K_1 > 0$ ,  $K_2 = -K_1$ ). The energy for a given magnetization orientation is coded as a distance from the axes origin, and additionally as a color.

In ultrathin structures the demagnetizing energy plays an important role and acts together with the magnetocrystalline energy. With the uniaxial magnetocrystalline anisotropy, the total anisotropy energy can be expressed as a sum:

$$E_{\text{ani}} = E_{\text{uni}} + E_{\text{dem}}. \quad (1.8)$$

The cosine from Eq. (1.7) can be converted into a sine with the Pythagorean trigonometric identity, and then we get an expression for  $E_{\text{ani}}$  of a “uniaxial form”, with new effective anisotropy constants:

$$E_{\text{ani}} = K_{0\text{eff}} + K_{1\text{eff}} \sin^2 \theta + K_2 \sin^4 \theta + \dots, \quad (1.9)$$

with

$$K_{1\text{eff}} = K_1 - \frac{1}{2} \mu_0 M^2. \quad (1.10)$$

In addition to the demagnetizing energy, the surfaces and interfaces of ultrathin films may contribute strongly to the magnetocrystalline anisotropy – at the interfaces the crystallographic symmetry is broken, atomic bonds are missing and orbital moments are quenched incompletely, resulting in a big difference between in-plane and out-of-plane orbital moments in the Bruno’s approach [10]. According to the phenomenological Néel formula [11, 12], the first anisotropy constant can be expressed as a sum of a volume (bulk) and a surface/interface contribution<sup>1</sup>:

$$K_1 = K_v + \frac{2K_s}{d} \quad (1.11)$$

Reducing the thickness of the film, the importance of the surfaces increases, as a larger fraction of the film is surface. Thus, the surface contribution to the anisotropy is thickness-dependent, proportional to  $1/d$ . Rewriting Eq. (1.10) with the new  $K_1$  dependence (Eq. (1.11)) we get:

$$K_{1\text{eff}} = K_v + \frac{2K_s}{d} - \frac{1}{2}\mu_0 M^2. \quad (1.12)$$

As a result of the competition between three contributions (the volume and surface anisotropies and the demagnetization term), the  $K_{1\text{eff}}$  constant can be either positive or negative, depending on thickness. In particular, for some critical thickness  $d_0$ , there is  $K_{1\text{eff}} = 0$  and, neglecting the  $K_2$  constant, a spin reorientation transition (SRT) occurs: the magnetization changes orientation from the in-plane (for  $d > d_0$ ) to the out-of-plane state (for  $d < d_0$ ). Experimental confirmation of the existence of the spontaneous perpendicular magnetization due to the Néel’s surface anisotropy was delivered in 1969 by Gradmann [13], with Ni-Fe alloy of a few atomic layers thickness. In the following studies [14–16] the thickness-driven SRT was observed in Co and Fe ultrathin films.

The formalism described above is commonly used, however it is not correct in the general case. It was demonstrated [17], that the separation of the induced anisotropy into volume and surface contribution is valid only for thick films. In the case of thin films (of a few nanometers) the surface-induced anisotropy is not strictly confined to the surfaces or interfaces, but extends into the depth of the magnetic layer. Nevertheless, if only the thickness-dependence of the anisotropy is observed in the experiment, analyzing the data one can introduce some effective parameters, responsible for the thickness-dependent and thickness-independent contributions, calling them as effective surface and bulk anisotropy constants.

---

<sup>1</sup> $K_s$  in this equation is an averaged surface contribution. Sometimes it is possible to distinguish the contributions corresponding to the top and bottom of the layer,  $K_{st}$  and  $K_{sb}$ , respectively.

### 1.2.3 Anisotropy field

The magnetic anisotropy can be treated either in terms of energy (Eq. (1.6)), or as an equivalent magnetic field vector. From thermodynamic relations we have:

$$\mathbf{H} = -\frac{1}{\mu_0} \frac{\partial E}{\partial \mathbf{M}}. \quad (1.13)$$

Applying this equation to the formula for anisotropy energy (Eq. (1.9)), we can calculate then the *anisotropy field*. Within a coordinate system with a  $\hat{z}$  axis oriented along the specified anisotropy axis, the uniaxial anisotropy energy depends on the  $\hat{z}$ -component of the magnetization only, as the sine square term in Eq. (1.9) can be rewritten as:

$$\sin^2 \theta = 1 - \cos^2 \theta = 1 - (M_z/M)^2. \quad (1.14)$$

Thus, performing differentiation, the anisotropy field can be expressed as an axial field:

$$\mathbf{H}_{\text{ani}} = \hat{z} \left[ \frac{2K_{1\text{eff}}}{\mu_0 M} \cos \theta + \frac{4K_2}{\mu_0 M} (\cos \theta - \cos^3 \theta) + \dots \right]. \quad (1.15)$$

Within the approximation of the first anisotropy constant only, we can write it in a simpler form:

$$\mathbf{H}_{\text{ani}} = \hat{z} H_{1\text{eff}} \cos \theta, \quad (1.16)$$

with  $H_{1\text{eff}}$ , connected with  $K_{1\text{eff}}$  (Eq. (1.12)):

$$H_{1\text{eff}} = \frac{2}{\mu_0 M} \left( K_v + \frac{2K_s}{d} \right) - M. \quad (1.17)$$

### 1.2.4 Preferred magnetization orientation

To calculate the preferred magnetization orientation in an anisotropic sample in the presence of an external magnetic field, the total magnetic energy of a sample, composed of the Zeeman energy (Eq. (1.1)) and the total anisotropy energy (Eq. (1.9)) should be minimized with respect to the angle  $\theta$ . An equivalent approach is to consider the total magnetic field vector affecting the sample (the external field plus the anisotropy field, which depends on the magnetization orientation). This method is called the *Stoner-Wohlfarth model* [18] and allows to reproduce the shape of the hysteresis curve for a magnetic field applied at a certain angle with respect to the anisotropy axis. In Figure 1.8 two simple cases are shown: the behavior of the sample with the field applied parallelly and perpendicularly to the axis (the easy axis and the hard axis cases, respectively).

Applying the external magnetic field along the hard direction has an additional useful property. We act then against the anisotropy field, which should be overcome to reach the magnetization saturation state. It means that the saturation field is equal to

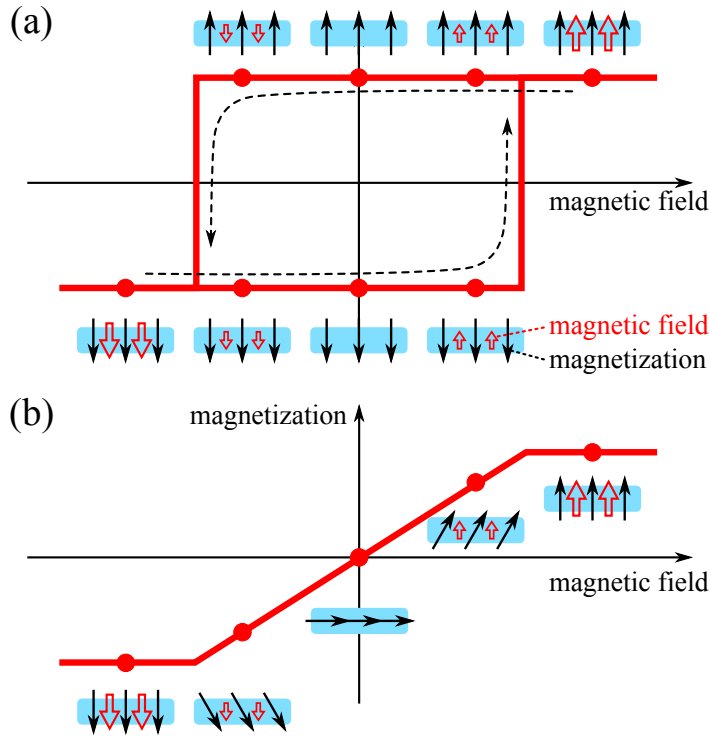


**Figure 1.8:** Hysteresis curves (the out-of-plane magnetization component vs. the amplitude of the applied magnetic field) for a sample with the uniaxial anisotropy of: (a) an easy-axis and (b) an easy-plane type, according to the Stoner-Wohlfahrt model. In both cases a magnetic field is applied perpendicularly to the sample plane, which is (a) the easy or (b) the hard direction.

the effective anisotropy field, and in fact this method is widely used for determination of the anisotropy constants, employing Eq. (1.17) and fitting procedures.

However, the Stoner-Wohlfahrt model has a serious limitation: it is assumed that the sample is small enough not to break down into *magnetic domains* and that the change of magnetization occurs via a coherent rotation only. A real sample of a finite size, being homogeneously magnetized, creates a very strong stray field, which can be reduced easily by the creation of magnetic domains. Under an external magnetic field, the magnetization in particular magnetic domains can respond in different ways: by coherent rotation, or by changing the domain size realized by domain wall motion. To predict the magnetization curve for a certain sample, usually micromagnetic simulations including all interactions between the magnetic moments are required.

### 1.3 Scope of the Thesis

Magnetic anisotropy is crucial in studies of magnetism in general, as well as for practical applications in magnetic devices, as it determines both static properties, such as the stability of magnetic bits persisting for years, and the switching dynamics of such bits on a sub-nanosecond time scale. Knowledge about the ways of modifying the magnetic anisotropy allows us to create new materials with desired magnetic properties, suitable for such devices, to reach higher quality, stability, capacity, and lower price.

This Thesis describes experimental studies concerning novel aspects of light-induced modification of the magnetic anisotropy in ultrathin Co systems. After this introductory chapter, which explains some basic ideas of magnetization and magnetic anisotropy, in Chapter 2 numerous techniques of modification the magnetic anisotropy, which have been applied in the last tens of years, are presented, focusing on methods which apply to ultrathin magnetic films. In Chapter 3 the experimental techniques employed in this work are explained, in particular the magneto-optical Kerr effect, and its applications in various experimental setups, probing either magnetization statics or dynamics.

The most general classification of the modification techniques, provided in Chapter 2, involves reversible and irreversible changes of the magnetic anisotropy. This classification can be found in the experimental part of this Thesis, in Chapters 4 and 5. In Chapter 4 the laser-induced magnetization precession in ultrathin Pt/Co/Pt systems is discussed. This process originates from the fully reversible thermal changes of the effective anisotropy field. The experimental results are supported with a novel method of modeling this phenomenon. In Chapter 5 similar ultrathin Co systems, treated with higher fluences of the laser light, are presented. Such laser-annealing leads to irreversible changes of the sample structure and thus also to irreversible changes of the magnetic anisotropy. In particular, a novel possibility of a creation of the out-of-plane magnetization phase is reported. At the end, three appendices are attached, to discuss some further details of experimental procedures or theoretical calculations, which were carried out in the frame of the Thesis.

### References

- [1] J. Stöhr and H. C. Siegmann, *Magnetism: From Fundamentals to Nanoscale Dynamics* (Springer-Verlag, Berlin, 2006).
- [2] M. Getzlaff, *Fundamentals of Magnetism* (Springer-Verlag Berlin / Heidelberg, 2008).
- [3] M. D. Kuz'min, Phys. Rev. Lett. **94**, 107204 (2005).

- 
- [4] M. I. Kaganov, I. M. Lifshitz, and L. V. Tanatarov, *Sov. Phys. JETP* **4**, 173 (1957).
  - [5] S. Anisimov, B. Kapeliovich, and T. Perelman, *Sov. Phys. JETP* **39**, 375 (1974).
  - [6] E. Beaupaire, J.-C. Merle, A. Daunois, and J.-Y. Bigot, *Phys. Rev. Lett.* **76**, 4250 (1996).
  - [7] L. Landau and E. Lifshitz, *Phys. Z. Sowietunion* **8**, 153 (1935).
  - [8] T. Gilbert, *IEEE Trans. Magn.* **40**, 3443 (2004).
  - [9] J. H. van Vleck, *Phys. Rev.* **52**, 1178 (1937).
  - [10] P. Bruno, *Phys. Rev. B* **39**, 865 (1989).
  - [11] L. Néel, *J. Phys. Radiat.* **15**, 225 (1954).
  - [12] P. Bruno and J. P. Renard, *Appl. Phys. A* **49**, 499 (1989), 10.1007/BF00617016.
  - [13] U. Gradmann, *J. Appl. Phys.* **40**, 1182 (1969).
  - [14] C. Chappert, K. L. Dang, P. Beauvillain, H. Hurdequint, and D. Renard, *Phys. Rev. B* **34**, 3192 (1986).
  - [15] R. Allenspach, M. Stampanoni, and A. Bischof, *Phys. Rev. Lett.* **65**, 3344 (1990).
  - [16] R. Allenspach and A. Bischof, *Phys. Rev. Lett.* **69**, 3385 (1992).
  - [17] A. Bogdanov, U. R. ler, and K.-H. Müller, *Journal of Magnetism and Magnetic Materials* **238**, 155 (2002).
  - [18] E. C. Stoner and E. P. Wohlfarth, *Philos. Trans. R. Soc. London* **240**, 599 (1948).





## CHAPTER 2

---

### Modifying the magnetic anisotropy

---

Magnetic anisotropy depends on numerous parameters. That makes it a complex and complicated phenomenon, but on the other hand, modifying some parameters or properties of a material, one can modify the magnetic anisotropy. However, the connections between the various parameters are not always trivial. In this Chapter some ways of modifying the magnetic anisotropy will be presented. At first, the anisotropy can be tuned at the stage of sample design. In Section 2.1 some interesting effects connected with sample composition and preparation will be discussed. Second, already-produced samples can be treated afterward with various techniques, which can result in modification of the anisotropy, classified in two main groups of processes: reversible and irreversible. Reversible processes are characterized by temporary changes of the magnetic properties, followed by a return to the initial state. In Section 2.2 the ways of modification the magnetic anisotropy, of both thermal and non-thermal origin, will be presented. With irreversible processes certain structural changes of the sample are induced, affecting the magnetic properties permanently. Section 2.3 shows some effects on magnetic anisotropy, obtained irreversibly with laser processing and ion-bombardment.

## 2.1 Samples composition

Ultrathin metallic films with a thickness of a few nanometers, described in Chapter 1, are usually too delicate to exist alone. For practical reasons, they must be deposited onto a substrate of at least several micrometers thick. The most popular substrates are  $\alpha$ -Al<sub>2</sub>O<sub>3</sub> (sapphire), MgO, Si, SiO<sub>2</sub>, SiN, mica and others. Very often a proper buffer layer (*underlayer*) must be deposited onto a substrate, to enable a correct growth of the “main” magnetic material. Finally, if the studied material reacts with the ambient air, which is the case of most of magnetics, also a capping layer (*overlayer*) of e.g. a noble metal is necessary for *ex-situ* measurements, to prevent a sample from oxidation.

On the other hand, all of these aspects have a huge influence on the magnetic properties of ultrathin systems: substrate, underlayer, overlayer – their type, thickness, crystallographic orientation, as well as method of production and conditions during growth, like temperature or pressure. In this Section several possibilities of tailoring the magnetic anisotropy at the stage of sample preparation will be presented.

### 2.1.1 Interface anisotropy

Interface anisotropy is represented by  $K_s$  in the phenomenological Néel model. It is extremely sensitive to the quality of interfaces, where the symmetry of magnetic interactions is broken. Neighboring atoms of different types possess different configurations of electron orbitals, and their overlapping, hybridization and partial quenching in a complicated manner may drastically affect the spin-orbit coupling and thus the magnetic anisotropy. In the 1980s and 1990s the systematical studies of the magnetic anisotropy in ultrathin metallic sandwiches were carried out and several combinations of a magnetic layer (Fe, Co, Ni) with underlayer and overlayer types (Ag, Au, Cu, Pd, Pt, Re, W) were examined [1–7]. The value for  $K_s$  is reported to change in a very broad range in a material-dependent way, moreover, very often there are some discrepancies for nominally identical compositions [8]. This is because the preparation process is also crucial [9] – pressure, temperature, deposition rate – they all determine the quality of the layers themselves, as well as the quality of the interfaces and their roughness, misfits, strains, stress, alloying, island-type or regular growth etc. It was shown, using the pair-interaction model proposed by Néel [10], that both roughness [11] and interdiffusion [12] between the neighboring layers reduce  $K_s$ , compared to a smooth interface. The value of the SRT thickness is closely related to the value of  $K_s$ . Putting in Eq. (1.12) a condition for the SRT,  $K_{\text{leff}} = 0$ , one can find a proportionality relation between the SRT thickness  $d_0$  and  $K_s$ . Thus, manipulating  $K_s$ , it is possible to shift  $d_0$ , i.e. to induce an out-of-plane or in-plane magnetization state, increasing or reducing the interface contribution to the anisotropy, respectively.

The dependence of the magnetic properties on the non-magnetic overlayer thickness was also observed. They were found to change non-monotonically: deposition of

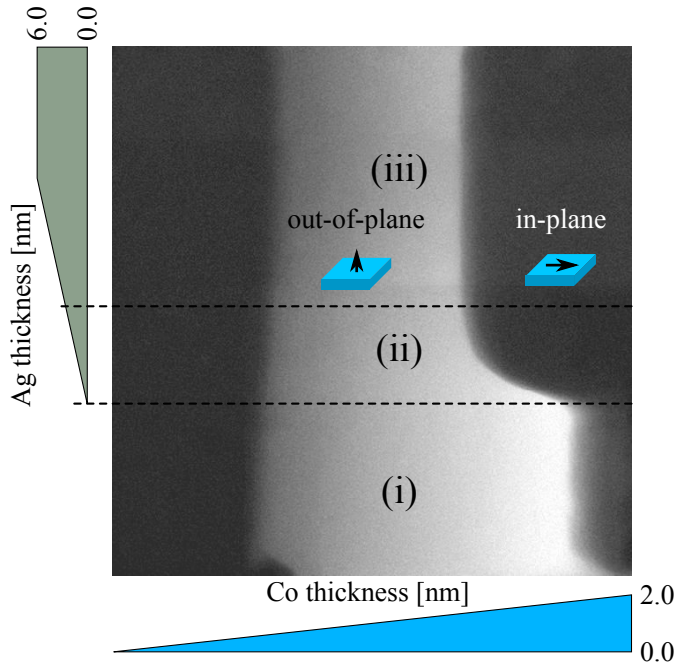


**Figure 2.1:** Preferred magnetization state, as a function of both Co and Ag thicknesses. Three regions: (i) Au/Co/Au; (ii) Au/Co/Ag/Au and (iii) Au/Co/Ag can be distinguished. The white color corresponds to the out-of-plane component of the magnetization. Figure was adapted from Ref. [14].

Ag, Au, Cu or Pd on ultrathin Co film leads to a peak in the magnetic anisotropy at about one monolayer coverage [4–6, 13]. Cu had the most pronounced effect, followed by Au, Ag, and Pd. The proposed explanation [7] is a hybridization between electrons of Co and the wetting monolayer (growing non-homogeneously), and subsequent dehybridization, when the nonmagnetic layer develops the bulk electronic structure.

Systematic studies of the influence of Ag and Au coverage on the magnetic properties of Co were done by Kisielewski et al. [14], with a double-wedged sample, which allowed to study simultaneously the dependencies on both Ag and Co thicknesses, changing continuously. The structure of the Co wedge with the Ag wedge overlayer were deposited on a Au film, and covered by an additional Au layer. The preferred magnetization state in that system is presented in Figure 2.1, coded with colors: the white color corresponds to the out-of-plane component of the magnetization. Three regions of the sample can be distinguished, dependent on the local structure: (i) Au/Co/Au system, with the SRT thickness of 1.8 nm; (ii) Au/Co/Ag/Au system

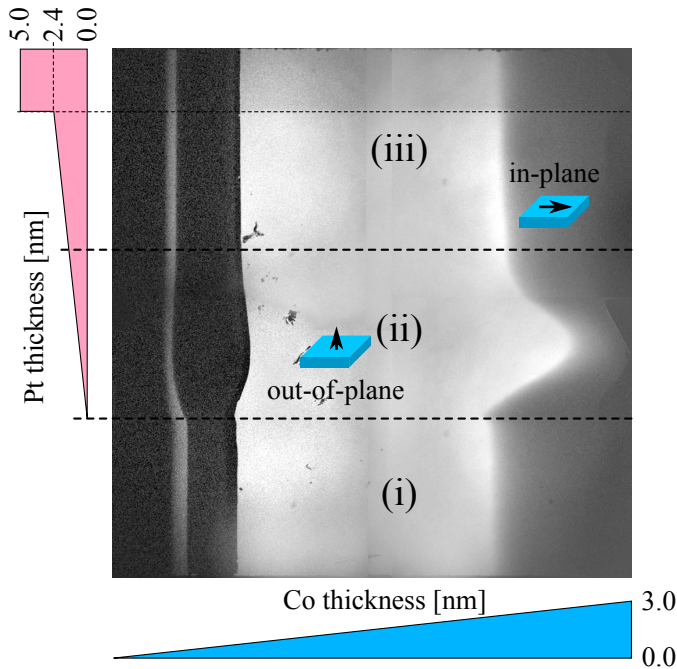


**Figure 2.2:** Preferred magnetization state, as a function of both Co and Pt thicknesses. Three regions: (i) Au/Co/Au; (ii) Au/Co/Pt/Au and (iii) Au/Co/Pt can be distinguished. The white color corresponds to the out-of-plane component of the magnetization. Figure was adapted from Ref. [15].

with gradually changing Ag thickness, and gradually decreasing the SRT thickness, down to 1.3 nm; the influence of Au is thus still visible; (iii) Au/Co/Ag system; a Ag thickness of about 3 nm is high enough to suppress any contribution from Au.

Within an analogous experiment, the Au/Co/Pt/Au system was also studied [15]. A similar double-wedged sample, with perpendicularly oriented wedges of Co with Pt overlayer, revealed an even more complicated influence of the Pt coverage on the magnetic anisotropy of the Co film. The corresponding magnetization phases are shown in Figure 2.2. Three regions can be also distinguished. Compared to the previously described structure, a thin Pt coverage drastically increases the range of Co thickness with the out-of-plane magnetization state, which is visible as a “bump” (region (ii)). For thick Pt, i.e. Au/Co/Pt system (region (iii)), the SRT occurs for a slightly higher Co thickness than for the reference Au/Co/Au (region (i)).

These two cases represent two distinctly different types of interface. In the first one, Co/Au and Co/Ag are known to be non-miscible [16–18] so the interfaces between

the Co film and the overlayer are rather sharp. Hybridization of electronic orbitals at the Co/Au and Co/Ag interface is different, resulting in different anisotropies and transition thicknesses. Due to mutual Ag-Au solubility [19], an alloy is formed at the Ag-Au interface, and the range where it interacts with the Co film, is manifested in the transient region (ii). In the latter case, on the contrary, Co and Pt like to make an alloyed interface [20]. Due to an orbital hybridization of intermixed atoms, a large magnetic moment may be induced on Pt atoms, up to about  $0.3 \mu_B/\text{atom}$  [21]. According to theoretical *ab-initio* calculations [22], both magnetic moments on Co and Pt may persist for high concentrations of Pt and for disorder alloys, too. Enhanced spin-orbit coupling of Pt atoms results in enhanced magnetic anisotropy [23, 24], which can explain the extended range of the out-of-plane phase. This picture becomes more complicated at the onset of the Pt wedge (region (ii)), where due to Pt/Au solubility [25], binary Pt/Au or even ternary Co/Pt/Au alloys may be formed.

### 2.1.2 In-plane anisotropy

In the above examples the hexagonal Co (0001) layer was deposited onto a Au underlayer of (111) orientation, so both layers exhibits similar six-fold crystallographic symmetries. Strains at interfaces, originating from slightly different lattice constants, are thus also of six-fold symmetry. In terms of magnetic interactions, various in-plane magnetization directions are equivalent in a reasonable approximation, and the magnetic anisotropy can be treated as uniaxial. A completely different situation occurs, if symmetries of underlayer and magnetic layer are different. Growing a hexagonal Co (0001) film on a Mo (110) underlayer creates anisotropic misfits and strains of two-fold symmetry, which results in an in-plane magnetic anisotropy [26, 27]. It shows up as an existence of an easy and hard axis, perpendicular to each other, both laying in the sample plane. However, the out-of-plane direction is still much “harder” than the hard in-plane one. To describe an in-plane anisotropy, usually an extra azimuth-dependent term is added to the expression for the anisotropy energy (Eqs. (1.6), (1.9)):

$$E_{\text{in}} = K_{\text{in}} \sin^2 \theta \sin^2 \phi. \quad (2.1)$$

A three-dimensional distribution of the anisotropy energy, calculated for the values of anisotropy constants reported in Ref. [26], is plotted in Figure 2.3.

## 2.2 Reversible modification

### 2.2.1 Magnetic anisotropy vs. temperature

The magnetic anisotropy is temperature-dependent and this dependence is closely connected to the thermal changes of the magnetization [28, 29]. Due to thermal fluctuations a parallel alignment of spins is destroyed and replaced by a “less-parallel”

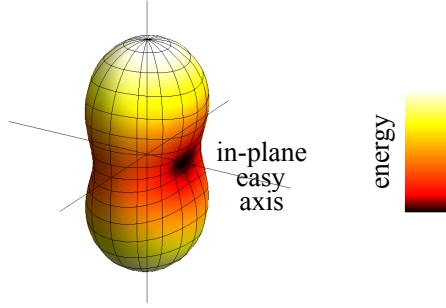


**Figure 2.3:** Distribution of anisotropy energy, calculated for the values of anisotropy constants reported in Ref. [26] for the Co thickness of 1.2 nm:  $K_1 = -0.07$ ,  $K_2 = 0.01$ ,  $K_{\text{in}} = 0.04\text{MJ/m}^3$ .

distribution. Through the spin-orbit interaction it affects electron orbitals and the anisotropy energy. In a classical approach for a cubic structure it is shown [28, 30], that the anisotropy energy (Eq. (1.5)), related to the easy/hard direction increases/decreases with increasing temperature, which makes the energy anisotropy distribution more isotropic and thus the anisotropy constant  $K_1$  lower, decreasing proportionally to the 10th power of magnetization. Similar calculations, repeated for the uniaxial case (Eq. (1.6)), yield a 3rd power in the dependence of  $K_1$ . A more general theoretical derivation [28], considering the spin-orbit interaction as a small perturbation of the exchange coupling, is based on an expression of the anisotropy energy in a series of spherical harmonics  $Y_{lm}(\theta, \phi)$  of even  $l$ 's. In the case of the uniaxial anisotropy, harmonics of a  $Y_{l0}(\theta)$ -type only are sufficient to describe the system:

$$E_{\text{uni}} = E_0 + \sum_{\text{even } l} \kappa_l(T) Y_{l0}(\theta). \quad (2.2)$$

The temperature-dependent coefficients are proportional to a certain power of magnetization:

$$\kappa_l(T) \propto M(T)^{l(l+1)/2}. \quad (2.3)$$

Spherical harmonics  $Y_{l0}$  of even  $l$  contain a series of cosines, with even powers up to  $l$ . Converting cosines to sines using standard trigonometric formulas, one obtains an expression for the uniaxial anisotropy energy (Eq. (2.2)) in a form which is similar to the classic formula (Eq. (1.6)). This way  $K_i$ 's constants can be determined by combination of  $\kappa_l$ 's and intrinsic coefficients of spherical harmonics. In the simplest case, to operate with the first anisotropy constant  $K_1$  only, one must cut the expansion after  $l = 2$ . Then

$$K_1(T) \propto M(T)^3. \quad (2.4)$$

To involve the second anisotropy constant  $K_2$ , the series should contain also the  $\kappa_4$  term, with the corresponding exponent  $n = 10$ , according to Eq. (2.3). However,  $\kappa_4$  appears then also in the  $K_1$  constant, whose temperature dependence is thus determined by a balance between  $\kappa_2(T)$  and  $\kappa_4(T)$ . Particularly, it may lead to an existence of a certain critical temperature  $T_{\text{crit}}$ , where  $K_1(T)$  changes sign. In fact, this property is observed e.g. in bulk cobalt [31].

In the case of ultrathin films the situation is even more complex. From the point of view of the first anisotropy constant  $K_1$  (Eq. (1.12)), the value of the exponent  $n = 3$  should work for both the  $K_v$  and  $K_s$  constants (as well as  $K_{\text{in}}$ ), as all of them are of the first order-anisotropy (represent a two-fold symmetry). However, several papers, both experimental [32–34] and theoretical [35–37], refer the temperature dependence of the surface magnetic anisotropy to vary in a more complicated manner. Like the anisotropy constant itself (see Section 2.1.1 above), also its temperature dependence depends on the type and thickness of the magnetic layer, as well as the type and crystallographic orientation of the substrate/underlayer/overlayer. Physically, there are several aspects of this diversity. One of them is the fact, that for the surface/interface anisotropy, a different temperature-dependence of the magnetization  $M_{\text{surf}}(T)$  may be applicable [29, 38] – due to a lower number of magnetic neighbors, atoms at the surface are more susceptible to thermal fluctuations and thus the  $M_{\text{surf}}(T)$  dependence is expected to be more rapid. Another point is that the situation strongly depends on stress [11, 39]: two neighboring metallic layers of different thermal expansion coefficients result in a non-trivial temperature-dependence of stress at the interfaces. Effectively, very often the observed  $K(T)$  dependence for thin films does not satisfy the Callens’ law. Nevertheless, sign changes in  $K(T)$  are often noticed, and the occurrence of  $T_{\text{crit}}$  results in a temperature-driven spin reorientation transitions, either from the out-of-plane to in-plane [40], or from in-plane to out-of-plane state [41], with increasing temperature.

Anyway, changing the temperature of the sample leads then to a reversible change of the magnetic anisotropy. Like in the case of thermal changes of the magnetization length, described in Chapter 1, the situation becomes particularly interesting, when the process becomes fast. Ultrafast heating the sample with ultrashort laser pulses, resulting in ultrafast demagnetization (Chapter 1.1.2), is accompanied by a sudden change of the demagnetizing field and/or the anisotropy field. At certain conditions this process may result in a change of the direction of the effective magnetic field, so the magnetization suddenly appears to be in a non-equilibrium orientation and it starts to precess (Chapter 1.1.4). The precession occurs around the effective magnetic field direction, that gradually changes its orientation back to the initial position, during cooling down of the sample.

Laser-induced precession of a thermal origin became possible to be studied in recent years, with the development of femtosecond pulsed lasers. It was observed mainly in metallic systems [42–44], employing visible or infrared laser light, as metals

exhibit large absorption coefficients in this spectral range, so the light-induced heating process runs effectively. The frequency and damping of the all-optically triggered magnetization precession, probed in the time-domain, are consistent with the ones derived with the classical ferromagnetic resonance (FMR) method, probed in the frequency-domain. However, a big advantage is the spatial resolution, limited by the size of the focused laser beam. Thus, the method is useful to study nanostructures or non-homogeneous samples, and mostly, to study the dynamics of the spin waves [42]. Due to its thermal character, the process generally does not depend on the polarization of the light, unless due to dichroism, the absorption and thus the temperature increase become polarization-dependent [45].

### 2.2.2 Photo-induced anisotropy

Magnetic properties of materials can be influenced by light non-thermally (i.e. without a temperature change) as well. A general class of phenomena, called *photomagnetic effects*, includes photo-induced changes of various magnetic properties, observed in several rather non-metallic materials [46–51]. In particular, the magnetic anisotropy itself can be modified this way. A mechanism of magnetic anisotropy change, described in Refs. [52, 53], occurring in Co-doped yttrium-iron-garnet (YIG), is based on a photo-induced redistribution of electrons, resulting in changing the valency of the Co ions which are responsible for the anisotropy. The development of pulsed lasers allowed to study the ultrafast dynamics of such processes [54, 55]. A laser pulse changes the magnetic anisotropy ultrafast, which results, similarly as mentioned above, in sudden changes of the effective magnetic field and thus in magnetization precession. The photo-induced anisotropy is usually polarization-dependent, so the amplitude of precession also depends on the plane of linear polarization of the light. As garnets are more transparent than metals, the light absorption and thus the thermal effects play a negligible role.

## 2.3 Irreversible modification

### 2.3.1 Laser processing

Light, absorbed in metals, as was mentioned, can lead to an increase of the temperature. In the case of low energies and thus low induced temperatures, it may bring reversible changes of magnetic properties – the demagnetization, eventually followed by the magnetization precession.

Interesting effects occur for higher energy densities. It may happen, that at elevated temperatures, because of an enhanced diffusion between neighboring layers or even partial melting, the sample structure changes, and this change persists after cooling down to the initial temperature. The effects of thermally-induced changes



at interfaces can be observed for a classical furnace annealing as well. The results depend strongly on materials involved. For instance, the Co/Pt interface tends to degrade upon annealing – atoms intermix, making alloys [56], due to a large negative enthalpy of alloy formation at elevated temperatures [57]. On the contrary, Co and Au are not-miscible [17, 18], and diffusion occurring due to annealing may lead to an improvement and ordering of the interface [58]. As the magnetic anisotropy is extremely sensitive to small changes of the interface quality, this opens a very wide field for the modification of the magnetic properties of materials, which can be done using laser light with sub-micrometer precision. Degradation of the interfaces due to the atomic intermixing results in decreasing the magnetic anisotropy [12]. This effect was studied e.g. for the Co/Pt multilayer structures [59, 60], allowing to create planarly magnetized nanostructures on an out-of-plane background.

With energies even higher, resulting in induced temperatures above the melting point, the material can melt, which creates some further interesting possibilities. Using phenomena occurring in liquids, like surface tension and dewetting, it is possible to create nanostructures from solidified drops [61–63]. Particularly, within magnetic materials, the magnetic properties of such nanostructures drastically change compared to continuous films. For instance, depending on the size of a cobalt dot, an in-plane or out-of-plane magnetic anisotropy appears, with a mono- or multi-domain structure of magnetization [64]. Possibilities of changing in this way the magnetic anisotropy were also observed e.g. in magnetic metallic glasses [65].

In the case of extremely high light energy densities of several  $\text{J}/\text{cm}^2$ , the induced temperature is far above the boiling point of a material, what results in evaporating the material and etching the sample [66–68].

The obtained effects depend, as was listed, on the amount of deposited energy, but also on the way it is deposited – the use of pulses or continuous light; various pulse duration or repetition rate may result in various effects. Because of the rather local character of the laser treatment, they may also depend on the pulse geometry – in particular, employing the interference of two (or more) pulsed laser beams, one gets an energy distribution on the sample surface according to a distribution of interference fringes, with typical sizes of  $\lambda/2$ . Nanostructures produced with such *pulse laser interference lithography* [69–72] can be controlled by the number and geometry of interfering beams, as well as by their wavelengths, polarizations or phases.

### 2.3.2 Ion-irradiation

In 1998 Chappert et al. demonstrated a new technique of modifying the magnetic anisotropy [73]. Pt/Co/Pt systems with various Co thicknesses were bombarded with  $\text{He}^+$  ions of energies of 30 keV with various fluences (number of ions per area unit). The magnetic anisotropy was found to decrease, which resulted in a change of the preferred magnetization orientation from out-of-plane to in-plane for Co thicknesses just

below the SRT. Additionally, as the irradiation was done through a lithographically-made resist mask, micrometer-size lines with changed magnetic properties were created. In several subsequent experiments sub-50 nm planar magnetic nanostructures fabricated by ion irradiation were demonstrated [74]. The structural origin of this change was explained, again, in terms of the mixing at interfaces [75].

Ferré et al. [76] demonstrated phase diagrams of the magnetization state, as a function of the ion fluence and the temperature. The Co-thickness range of an out-of-plane magnetization state was found to shrink with increasing He<sup>+</sup> ion fluence, replaced by an oblique and an in-plane state. Also, the Curie temperature was found to decrease with the ion dose.

Quite intuitively, the efficiency of the irradiation increases with the mass of the bombarding ions [77–79]. However, irradiation with Ga<sup>+</sup> ions surprisingly induces an effect opposite to the one mentioned above: the magnetic anisotropy increases and the magnetization changes orientation from the in-plane to the out-of-plane direction [80]. More systematic studies on the Pt/Co/Pt systems with wider ranges of the Co thickness and fluence, showed a more complicated sequence of transitions between magnetization states [81], with two “branches” of re-entrant out-of-plane magnetization states, obtained subsequently with increasing fluence. Adapted from Ref. [81], a two-dimensional diagram of the remanence, as a function of Co thickness and the fluence, is displayed in Figure 2.4.

On the other hand, the mechanism of the irradiation-induced structural changes responsible for the appearing perpendicular anisotropy is not clear yet. Explanations given by Maziewski et al. [81] concern the creation of ordered CoPt and CoPt<sub>3</sub> alloys, exhibiting high perpendicular anisotropy. However, another possible explanation is the appearance of some extra stresses, created at interfaces by bombarding ions [82].

## References

- [1] U. Gradmann and R. Bergholz, *Phys. Rev. Lett.* **52**, 771 (1984).
- [2] E. Bergter, U. Gradmann, and R. Bergholz, *Solid State Commun.* **53**, 565 (1985).
- [3] H. J. Elmers and U. Gradmann, *Appl. Phys. A* **51**, 255 (1990).
- [4] B. N. Engel, M. H. Wiedmann, R. A. Van Leeuwen, and C. M. Falco, *Phys. Rev. B* **48**, 9894 (1993).
- [5] P. Beauvillain, A. Bounouh, C. Chappert, R. Mégy, S. Ould-Mahfoud, J. P. Renard, P. Veillet, D. Weller, and J. Corno, *J. Appl. Phys.* **76**, 6078 (1994).
- [6] B. N. Engel, M. H. Wiedmann, and C. M. Falco, *J. Appl. Phys.* **75**, 6401 (1994).
- [7] T. Duden and E. Bauer, *Phys. Rev. B* **59**, 468 (1999).

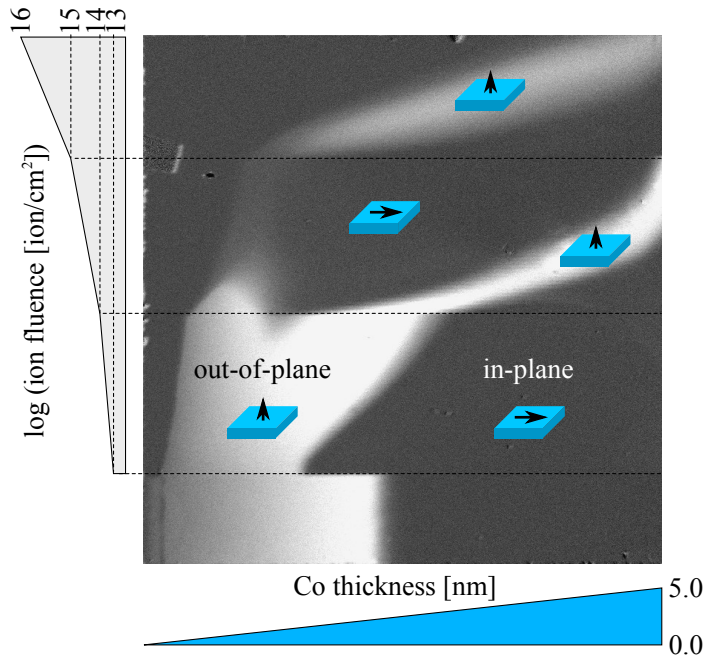


**Figure 2.4:** Preferred magnetization orientation in  $\text{Ga}^+$  ion-irradiated Pt/Co/Pt structure, as a function of the Co thickness (and the ion fluence). The white color corresponds to the out-of-plane component of the magnetization. For a certain range of Co thicknesses the out-of-plane magnetization state within the two branches can be induced by increasing the ion fluence. Adapted from Ref. [81].

- [8] W. J. M. de Jonge, P. J. H. Bloemen, and F. J. A. den Broeder, *Ultrathin Magnetic Structures* (Springer-Verlag, 1994), chap. Experimental investigations of magnetic anisotropy.
- [9] G. A. Bertero, R. Sinclair, C.-H. Park, and Z. X. Shen, *J. Appl. Phys.* **77**, 3953 (1995).
- [10] L. Néel, *J. Phys. Radiat.* **15**, 376 (1954).
- [11] P. Bruno, *J. Phys. F* **18**, 1291 (1988).
- [12] H. J. G. Draaisma, F. J. A. den Broeder, and W. J. M. de Jonge, *J. Appl. Phys.* **63**, 3479 (1988).
- [13] M. H. Wiedmann, C. Marliere, B. N. Engel, and C. M. Falco, *J. Magn. Magn. Mat.* **148**, 125 (1995).

- [14] M. Kisielewski, A. Maziewski, M. Tekielak, A. Wawro, and L. T. Baczewski, *Phys. Rev. Lett.* **89**, 087203 (2002).
- [15] J. Kisielewski, A. Maziewski, K. Postava, A. Stupakiewicz, A. Petrouchik, L. T. Baczewski, and A. Wawro, *J. Magn. Magn. Mat.* **322**, 1475 (2010).
- [16] *ASM Handbook Volume 03: Alloy Phase Diagrams* (ASM International, 1992).
- [17] M. Speckmann, H. P. Oepen, and H. Ibach, *Phys. Rev. Lett.* **75**, 2035 (1995).
- [18] N. Marsot, R. Belkhou, F. Scheurer, B. Bartenlian, N. Barrett, M. Delaunay, and C. Guillot, *Surf. Sci.* **377-379**, 225 (1997), ISSN 0039-6028.
- [19] T. B. Massalski, *Binary Alloy Diagrams* (Ohio, 1986).
- [20] C. Train, P. Beauvillain, V. Mathet, G. Pénissard, and P. Veillet, *J. Appl. Phys.* **86**, 3165 (1999).
- [21] F. Menzinger and A. Paoletti, *Phys. Rev.* **143**, 365 (1966).
- [22] O. Šipr, J. Minár, S. Mankovsky, and H. Ebert, *Phys. Rev. B* **78**, 144403 (2008).
- [23] D. Weller, H. Brändle, G. Gorman, C.-J. Lin, and H. Notarys, *Appl. Phys. Lett.* **61**, 2726 (1992).
- [24] D. Weller, H. Brändle, and C. Chappert, *J. Magn. Magn. Mat.* **121**, 461 (1993).
- [25] Z. Bastl and Š. Pick, *Surf. Sci.* **566-568, Part 2**, 832 (2004).
- [26] A. Stupakiewicz, Z. Kurant, A. Maziewski, L. Baczewski, A. Maneikis, and A. Wawro, *J. Magn. Magn. Mat.* **290-291, Part 1**, 242 (2005).
- [27] Z. Kurant, J. Jaworowicz, A. Maziewski, A. Stupakiewicz, V. Zablotskii, A. Petrouchik, L. Baczewski, and A. Wawro, *J. Magn. Magn. Mat.* **316**, e507 (2007).
- [28] H. Callen and E. Callen, *J. Phys. Chem. Solids* **27**, 1271 (1966).
- [29] M. Farle, *Rep. Prog. Phys.* **61**, 755 (1998).
- [30] N. Akulov, *Z. Phys.* **100**, 197 (1936).
- [31] C. Zener, *Phys. Rev.* **96**, 1335 (1954).
- [32] O. Fruchart, J.-P. Nozieres, and D. Givord, *J. Magn. Magn. Mat.* **165**, 508 (1997).

- 
- [33] M. Farle, W. Platow, A. Anisimov, B. Schulz, and K. Baberschke, *Journal of Magnetism and Magnetic Materials* **165**, 74 (1997).
- [34] A. Enders, D. Peterka, D. Repetto, N. Lin, A. Dmitriev, and K. Kern, *Phys. Rev. Lett.* **90**, 217203 (2003).
- [35] J. B. Staunton, L. Szunyogh, A. Buruzs, B. L. Gyorffy, S. Ostanin, and L. Udvardi, *Phys. Rev. B* **74**, 144411 (2006).
- [36] A. Buruzs, P. Weinberger, L. Szunyogh, L. Udvardi, P. I. Chleboun, A. M. Fischer, and J. B. Staunton, *Phys. Rev. B* **76**, 064417 (2007).
- [37] P. Asselin, R. F. L. Evans, J. Barker, R. W. Chantrell, R. Yanes, O. Chubykalo-Fesenko, D. Hinzke, and U. Nowak, *Phys. Rev. B* **82**, 054415 (2010).
- [38] P. Jensen, H. Dreyssé, and K. Bennemann, *Surf. Sci.* **269–270**, 627 (1992).
- [39] H. Fritzsche, J. Kohlhepp, and U. Gradmann, *Phys. Rev. B* **51**, 15933 (1995).
- [40] D. P. Pappas, K.-P. Kämper, and H. Hopster, *Phys. Rev. Lett.* **64**, 3179 (1990).
- [41] B. Schulz and K. Baberschke, *Phys. Rev. B* **50**, 13467 (1994).
- [42] M. van Kampen, C. Jozsa, J. T. Kohlhepp, P. LeClair, L. Lagae, W. J. M. de Jonge, and B. Koopmans, *Phys. Rev. Lett.* **88**, 227201 (2002).
- [43] J.-Y. Bigot, M. Vomir, L. H. F. Andrade, and E. Beaurepaire, *Chem. Phys.* **318**, 137 (2005).
- [44] S. Mizukami, E. P. Sajitha, D. Watanabe, F. Wu, T. Miyazaki, H. Naganuma, M. Oogane, and Y. Ando, *Appl. Phys. Lett.* **96**, 152502 (2010).
- [45] A. R. Khorsand, M. Savoini, A. Kirilyuk, A. V. Kimel, A. Tsukamoto, A. Itoh, and T. Rasing, *Phys. Rev. Lett.* **108**, 127205 (2012).
- [46] W. Lems, P. J. Rijnierse, P. F. Bongers, and U. Enz, *Phys. Rev. Lett.* **21**, 1643 (1968).
- [47] M. Ayadi and J. Ferré, *Phys. Rev. Lett.* **50**, 274 (1983).
- [48] E. L. Nagaev, *Phys. Status Solidi B* **145**, 11 (1988).
- [49] E. Mosiniewicz-Szablewska and H. Szymczak, *Phys. Rev. B* **47**, 8700 (1993).
- [50] M. Baran, S. L. Gnatchenko, O. Y. Gorbenko, A. R. Kaul, R. Szymczak, and H. Szymczak, *Phys. Rev. B* **60**, 9244 (1999).

- [51] D. A. Pejaković, J. L. Manson, J. S. Miller, and A. J. Epstein, *Phys. Rev. Lett.* **85**, 1994 (2000).
- [52] A. B. Chizhik, I. I. Davidenko, A. Maziewski, and A. Stupakiewicz, *Phys. Rev. B* **57**, 14366 (1998).
- [53] A. Stupakiewicz, A. Maziewski, I. Davidenko, and V. Zablotskii, *Phys. Rev. B* **64**, 064405 (2001).
- [54] F. Hansteen, A. Kimel, A. Kirilyuk, and T. Rasing, *Phys. Rev. Lett.* **95**, 047402 (2005).
- [55] F. Hansteen, A. Kimel, A. Kirilyuk, and T. Rasing, *Phys. Rev. B* **73**, 014421 (2006).
- [56] M. Galeotti, A. Atrei, U. Bardi, B. Cortigiani, G. Rovida, and M. Torrini, *Surf. Sci.* **297**, 202 (1993).
- [57] R. Oriani and W. Murphy, *Acta Metall.* **10**, 879 (1962).
- [58] F. J. A. den Broeder, D. Kuiper, A. P. van de Mosselaer, and W. Hoving, *Phys. Rev. Lett.* **60**, 2769 (1988).
- [59] A. Aktag, S. Michalski, L. Yue, R. D. Kirby, and S.-H. Liou, *J. Appl. Phys.* **99**, 093901 (2006).
- [60] C. Schuppler, A. Habenicht, I. L. Guhr, M. Maret, P. Leiderer, J. Boneberg, and M. Albrecht, *Appl. Phys. Lett.* **88**, 012506 (2006).
- [61] J. Bischof, D. Scherer, S. Herminghaus, and P. Leiderer, *Phys. Rev. Lett.* **77**, 1536 (1996).
- [62] C. Favazza, J. Trice, H. Krishna, R. Kalyanaraman, and R. Sureshkumar, *Appl. Phys. Lett.* **88**, 153118 (2006).
- [63] J. Trice, D. Thomas, C. Favazza, R. Sureshkumar, and R. Kalyanaraman, *Phys. Rev. B* **75**, 235439 (2007).
- [64] H. Krishna, C. Miller, L. Longstreth-Spoor, Z. Nussinov, A. K. Gangopadhyay, and R. Kalyanaraman, *J. Appl. Phys.* **103**, 073902 (2008).
- [65] M. Sorescu and E. T. Knobbe, *Phys. Rev. B* **49**, 3253 (1994).
- [66] P. Pronko, S. Dutta, J. Squier, J. Rudd, D. Du, and G. Mourou, *Opt. Commun.* **114**, 106 (1995).

- [67] A. Zoubir, L. Shah, K. Richardson, and M. Richardson, *Appl. Phys. A* **77**, 311 (2003), 10.1007/s00339-003-2121-9.
- [68] J. Klein-Wiele, J. Bekesi, and P. Simon, *Appl. Phys. A* **79**, 775 (2004).
- [69] W. W. Ng, C.-S. Hong, and A. Yariv, *IEEE Trans. Electron Devices* **25**, 1193 (1978).
- [70] J. P. Spallas, A. M. Hawryluk, and D. R. Kania, *J. Vac. Sci. Technol. B* **13**, 1973 (1995).
- [71] A. Fernandez, P. Bedrossian, S. Baker, S. Vernon, and D. Kania, *IEEE Trans. Magn.* **32**, 4472 (1996).
- [72] N. I. Polushkin, V. Oliveira, O. Conde, R. Vilar, Y. N. Drozdov, A. Apolinario, A. Garcia-Garcia, J. M. Teixeira, and G. N. Kakazei, *Appl. Phys. Lett.* **101**, 132408 (2012).
- [73] C. Chappert, H. Bernas, J. Ferré, V. Kottler, J.-P. Jamet, Y. Chen, E. Cambril, T. Devolder, F. Rousseaux, V. Mathet, et al., *Science* **280**, 1919 (1998).
- [74] T. Devolder, C. Chappert, Y. Chen, E. Cambril, H. Bernas, J. P. Jamet, and J. Ferré, *Appl. Phys. Lett.* **74**, 3383 (1999).
- [75] T. Devolder, *Phys. Rev. B* **62**, 5794 (2000).
- [76] J. Ferré, T. Devolder, H. Bernas, J. P. Jamet, V. Repain, M. Bauer, N. Vernier, and C. Chappert, *J. Phys. D* **36**, 3103 (2003).
- [77] T. Blon, P. Baules, G. B. Assayag, V. Kolinský, J.-C. Ousset, and E. Snoeck, *J. Magn. Magn. Mat.* **315**, 5 (2007).
- [78] M. J. Bonder, N. D. Telling, P. J. Grundy, C. A. Faunce, T. Shen, and V. M. Vishnyakov, *J. Appl. Phys.* **93**, 7226 (2003).
- [79] C. Vieu, J. Gierak, H. Launois, T. Aign, P. Meyer, J. P. Jamet, J. Ferré, C. Chappert, T. Devolder, V. Mathet, et al., *J. Appl. Phys.* **91**, 3103 (2002).
- [80] J. Jaworowicz, A. Maziewski, P. Mazalski, M. Kisielewski, I. Sveklo, M. Tekielak, V. Zablotskii, J. Ferré, N. Vernier, A. Mougin, et al., *Appl. Phys. Lett.* **95**, 022502 (2009).
- [81] A. Maziewski, P. Mazalski, Z. Kurant, M. O. Liedke, J. McCord, J. Fassbender, J. Ferré, A. Mougin, A. Wawro, L. T. Baczewski, et al., *Phys. Rev. B* **85**, 054427 (2012).
- [82] M. Sakamaki, K. Amemiya, M. O. Liedke, J. Fassbender, P. Mazalski, I. Sveklo, and A. Maziewski, *Phys. Rev. B* **86**, 024418 (2012).





## CHAPTER 3

---

### Experimental techniques

---

Experimental physics fully relies on techniques and approaches, that become increasingly complicated. Before getting some interesting information that can be analyzed from the physical point of view, the samples must be planned and prepared, experimental setups consisting of many sophisticated devices must be composed, measurements must be performed and the measured data must be treated and analyzed with complicated procedures. In this Chapter the technical details of the experiments carried out in the frame of this Thesis will be presented: details of sample preparation using molecular beam epitaxy (MBE), the concept of the magneto-optical Kerr effect (MOKE), basics of the Kerr millimagnetometer and microscopy and the principles of femtosecond lasers, employed in the stroboscopic pump-probe setup.

### 3.1 Samples preparation

Most of the samples used in this work were produced using a molecular beam epitaxy (MBE) setup at the Institute of Physics of the Polish Academy of Sciences in Warsaw. This technique [1] allows to grow high-quality monocrystalline ultrathin layers. In extremely low pressure of  $10^{-10}$  Torr, obtained with an ion pump, metal sources in effusion cells are heated up to sublimate. Beams of atoms are directed to the substrate, where they deposit with a very slow rate of about 0.05 nm/s. Sources can be closed and opened with computerized shutters to grow a desired sequence of layers. Depositing metals simultaneously, alloys can be obtained. An additional shutter can be moved parallel to the substrate surface during the growing procedure, to create layers with a thickness gradient, i.e. with a shape of a wedge, with a slope that depends on the speed of this moving shutter. Deposition can be done either at room-temperature or at an electronically regulated temperature up to 1100°C. The quality of the crystal structure of the grown films can be monitored *in-situ* using reflection high-energy electron diffraction (RHEED) and low-energy electron diffraction (LEED) with energies of 12 and 1 keV, respectively. A chemical analysis of the surface can be carried out with the Auger electron spectroscopy (AES) technique, with energies up to 2200 eV. "Riber", the MBE apparatus that was used for preparation of our samples, is shown in Figure 3.1.

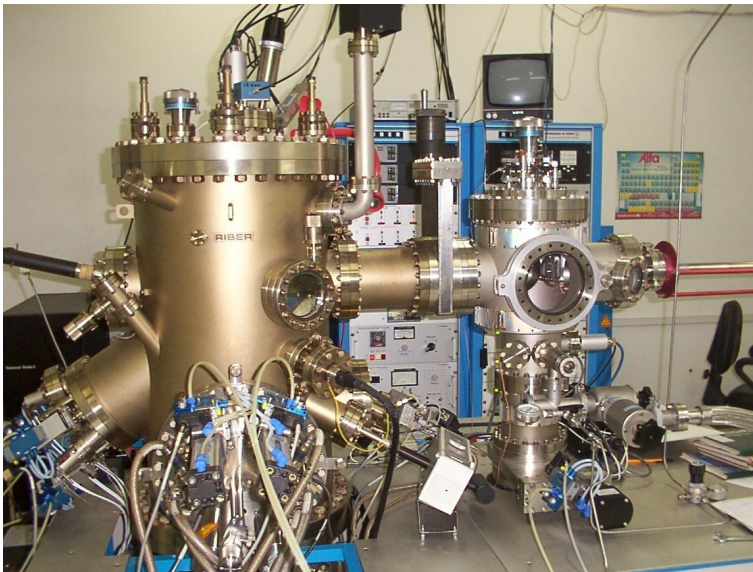


**Figure 3.1:** "Riber", the MBE apparatus at the Institute of Physics of Polish Academy of Sciences in Warsaw.

## 3.2 Magneto-Optical Kerr Effect

Magneto-Optics is a very broad branch of physics, describing the link between Magnetism and Optics, as the name itself may indicate – between light and magnetic materials. In general both the electric and magnetic components of the electromagnetic wave can interact with matter. However, for the optical frequencies of the light the interaction of its magnetic component is negligible, thus the magnetic permeability tensor is approximately equal to 1 [2]. A dominant influence of the electric component on matter is usually described with the *dielectric permittivity tensor* [3, 4]:

$$\hat{\epsilon} = \begin{pmatrix} \epsilon_{xx} & \epsilon_{xy} & \epsilon_{xz} \\ \epsilon_{yx} & \epsilon_{yy} & \epsilon_{yz} \\ \epsilon_{zx} & \epsilon_{zy} & \epsilon_{zz} \end{pmatrix}. \quad (3.1)$$

In the case of non-dissipative media this tensor is required to be Hermitian:

$$\epsilon_{ij} = \epsilon_{ji}^*. \quad (3.2)$$

Although a direct influence of the light magnetic component itself is negligible, in the presence of magnetic field or magnetization a situation changes. Due to the spin-orbit coupling, spins can affect electronic orbitals, inducing some asymmetry in the interaction with the light [5]. This asymmetry is described by the off-diagonal tensor elements. Their Hermiticity (Eq. (3.2)) requires that the real part of  $\epsilon_{ij}$  is symmetric and should be an even function of the magnetization (magnetic field), while the imaginary one is antisymmetric and odd. Thus, in the absence of magnetic field or magnetization, this results in a disappearance of the off-diagonal tensor components.

Depending on the geometry and the mutual orientation of the light and magnetization (or an external magnetic field, that orients the magnetization), several types of magneto-optical effects can be distinguished, named after the scientists who discovered and described them [3, 6, 7]: Michael Faraday (1845), John Kerr (1876), Woldemar Voigt (1902), Aimé Cotton and Henri Mouton (1907). If the field is applied perpendicularly to the light direction, it results in linear birefringence, observed in the Voigt and the Cotton-Mouton effects. In the case that the light and the field are parallel to each other, circular birefringence occurs, manifesting itself as a rotation of the plane of linear polarization, observed as the Faraday effect.

These three effects happen in transparent media and describe polarization changes of the light transmitting through the material. The Kerr effect, that concerns reflecting media, is more complex. The theory for both the Kerr and Faraday effects was developed by Argyres [5]. Depending on the direction of the field (or magnetization) with respect to the sample plane, three basic Kerr effect configurations can be distinguished:

- polar magneto-optical Kerr effect (PMOKE), sensitive to the magnetization that is normal to the sample plane;

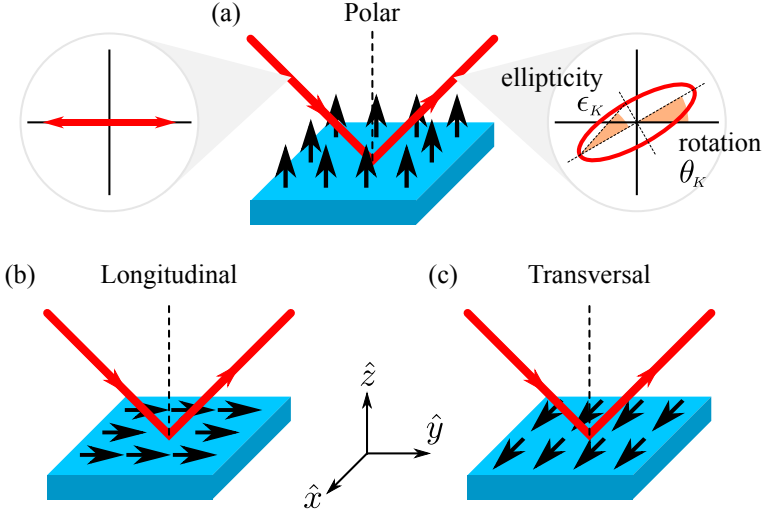


**Figure 3.2:** Three basic configurations of the magneto-optical Kerr effect, dependent on mutual configuration of the magnetic field or the magnetization direction and the plane of the light incidence: (a) polar; (b) longitudinal; (c) transversal. Figure (a) contains an explanation of the meaning of the rotation  $\theta_K$  and the ellipticity  $\epsilon_K$  of the polarization.

- longitudinal magneto-optical Kerr effect (LMOKE), magnetic field/magnetization parallel both to the sample plane and to the plane of incidence;
- transversal magneto-optical Kerr effect (TMOKE), magnetic field/magnetization parallel to the sample plane, but perpendicular to the plane of incidence.

The schemes for the polar, longitudinal and transversal MOKE's are shown in Figure 3.2. The fact, that the particular types of MOKE are sensitive to a certain orientation of the magnetization, means that each of them probes one component of the magnetization. For any general direction of the field or the magnetization, the respective effects can occur together, however in certain conditions it is possible to separate them. In the terms of the dielectric permittivity tensor, each component of the magnetization is represented by a proper off-diagonal tensor element. Additionally, for the case of a cubic symmetry of the media, the tensor can be simplified, as then the diagonal elements are identical and equal to a square of the refractive index of material:

$$\hat{\epsilon} = n^2 \begin{pmatrix} 1 & -iQm_P & iQm_L \\ iQm_P & 1 & -iQm_T \\ -iQm_L & iQm_T & 1 \end{pmatrix}, \quad (3.3)$$

where  $n$  is a complex refractive index of the media,  $Q$  is magneto-optical Voigt con-

stant,  $m_{P,L,T}$  are polar, longitudinal and transversal components of magnetization. For non-magnetic media  $Q = 0$ .

The PMOKE and LMOKE involve the change of the reflected light's polarization, i.e. Kerr rotation and Kerr ellipticity occurs (see Figure 3.2(a)), TMOKE involves the changes of the reflected light's intensity only. All the MOKE effects strongly depend on the angle of incidence. For normal incidence, PMOKE is the only observable effect. Increasing the incident angle it becomes less relevant whilst LMOKE becomes more dominant. For grazing incidence all the effects become weak due to the small penetration of a sample by the light.

Despite the fact, that the Kerr rotation and ellipticity are relatively small (typical values are of 1 millidegree (mdeg) up to 1 degree (or even more in some extreme cases [8]), such small changes can be measured quite easily and very precisely. Therefore, MOKE gives access to precise information about the actual magnetization state of a medium. The important property and the big advantage of the magneto-optical effects in practical use is that they happen exactly during the time when the light passes the sample. That makes magneto-optics an extremely useful technique, widely used in studies of magnetism, from quasi-statics to ultrafast magnetization dynamics. In the following Sections we present experimental applications of magneto-optics used in this work.

### 3.3 Kerr microscopy

To measure the Kerr rotation with the simplest version of the experimental setup, one needs only a light source, two linear polarizers and a photodiode. The light, going through the polarizer oriented at the angle of  $\phi_P$ , becomes linearly polarized. After reflection from the sample surface it gains some extra Kerr rotation  $\theta_K$  and ellipticity  $\epsilon_K$ , and next passes through the second polarizer (called an *analyzer*), oriented at the angle  $\phi_A$ , to be measured by the photodiode.

The final state of the polarization of the light, that hits the photodiode, can be expressed using the Jones matrices formalism [9]:

$$\mathbf{E} \propto \bar{P}(\phi_A) \cdot \bar{S}(\Theta_K) \cdot \bar{P}(\phi_P) \cdot \mathbf{E}_0. \quad (3.4)$$

Briefly speaking, the optical elements are represented by  $2 \times 2$ -matrices that affect the light, represented by a two-dimensional vector. Components  $x$ ,  $y$  of the vector are complex numbers, the absolute values and the arguments of which correspond to the amplitudes and phases, respectively, of the two orthogonal linear polarizations.  $\bar{P}$  is the Jones matrix for a linear polarizer oriented at an angle of  $\phi$  with respect to the horizontal direction ( $x$ ):

$$\bar{P}(\phi) = \begin{pmatrix} \cos^2 \phi & \cos \phi \sin \phi \\ \cos \phi \sin \phi & \sin^2 \phi \end{pmatrix}, \quad (3.5)$$

and  $\bar{S}$  is a matrix for the sample, as a magneto-optical medium. More details concerning the general form of this matrix can be found in Refs. [10–13]. Some symmetries occurring for PMOKE with normal light incidence [13], allow to use it in a simpler form:

$$\bar{S}(\Theta) = \begin{pmatrix} 1 & \Theta \\ \Theta & -1 \end{pmatrix}. \quad (3.6)$$

Here  $\Theta$  is a complex Kerr rotation angle, in the small-angle approximation expressed as  $\Theta = \theta_K + i\epsilon_K$ , with the Kerr rotation  $\theta_K$  and the Kerr ellipticity  $\epsilon_K$  as real and imaginary parts. The intensity probed by that photodiode is proportional to:

$$I \propto |\mathbf{E}|^2 = |E_x|^2 + |E_y|^2. \quad (3.7)$$

Let us assume that the analyzer and the polarizer are nearly crossed, i.e.  $\phi_A = \phi_P + 90^\circ + \delta_A$ , with a deviation of  $\delta_A$  of a few degrees from the fully crossed orientation. Using Eq. (3.4), with  $\phi_P = 0$  or  $\pi/2$  (that correspond to the  $p$  or  $s$  polarization of the light<sup>1</sup>, respectively), we get:

$$I \propto \cos^2 \delta_A (\theta_K^2 + \epsilon_K^2) + \sin^2 \delta_A - 2\theta_K \cos \delta_A \sin \delta_A \quad (3.8)$$

To simplify this calculation, we can make some further approximations. As the analyzer's deviation angle is small, typically  $\delta_A < 3^\circ$ ,

$$I \propto \theta_K^2 + \epsilon_K^2 + \delta_A^2 - 2\theta_K \delta_A. \quad (3.9)$$

Finally, taking the Kerr rotation and the Kerr ellipticity as the angles that are much smaller than  $\delta_A$ , i.e.  $\theta_K \ll \delta_A$  and  $\epsilon_K \ll \delta_A$ , we get

$$I \propto \delta_A^2 - 2\theta_K \delta_A. \quad (3.10)$$

The last term at the right hand side is proportional to the Kerr rotation. The change of polarization due to the Kerr effect is “converted”, using an optical system, into a proportional change of the light's intensity, that can be easily measured directly. Within the first term at the right hand side,  $\delta_A^2$ , the Malus' law in the small-angle approximation is manifested.

The Kerr effect can also be used for imaging, for example to visualize magnetic domains, replacing a photodiode with a two-dimensional detector. The scheme of a polar Kerr microscope is shown in Figure 3.3. As a light source a halogen lamp is used. After the polarizer, light is focused at the sample surface with the objective, it reflects back and after passing through the analyzer it goes to the CCD camera. The light intensity measured at the each pixel of the camera is proportional to the local

<sup>1</sup>Labels  $p$  and  $s$  of polarization determine its relation to the plane of light incidence:  $p$ arallel and  $s$ enkrecht=perpendicular (in German).

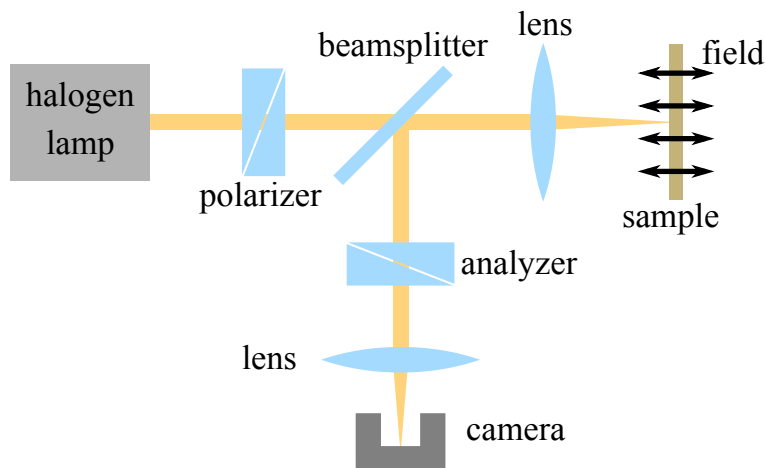


**Figure 3.3:** The scheme of the polar Kerr microscope. See the text for more details.

Kerr rotation, so it is possible to get a spatial dependence of the Kerr effect occurring at the sample, with the resolution defined by the optical system.

As was mentioned, a certain type of MOKE carries the information of the actual state of a respective component of the magnetization. The simplest configuration of a Kerr microscope is polar, and then for nearly normal incidence angle, the polar component of the magnetization is probed. However, there is also an LMOKE variant of the microscope, sensitive to the in-plane magnetization component. To probe the longitudinal component of the magnetization one needs to employ a peripheral part of the beam, which after focusing with the objective makes some acute incident angle. Such angle can be obtained with a system of diaphragms, which lets the light go only through a peripheral part of the objective, at its selected side. As most of the incoming light is cut this way, and as the longitudinal Kerr effect is usually much weaker than the polar one (an order of magnitude), this technique is more difficult than usual Kerr microscopy.

The kind of basic characterization of the magnetization state that can be done with the Kerr microscope is a *remanence image*. If a sample exhibits a remanence and a coercivity, the magnetization state depends on the sample's history. The two scenarios of the history are realized by field pulses applied in opposite directions (Figure 3.4). If there is any difference in the magnetization state at zero field after each of those pulses, the images taken then should be different. Any non-zero difference of the Kerr rotation and thus of the intensity recorded in those two pictures, is visible as a bright color at the differential image (Figure 3.4, upper loop). In the case of a lack of a remanence, there is no difference, which yields a dark color (Fig. 3.4,

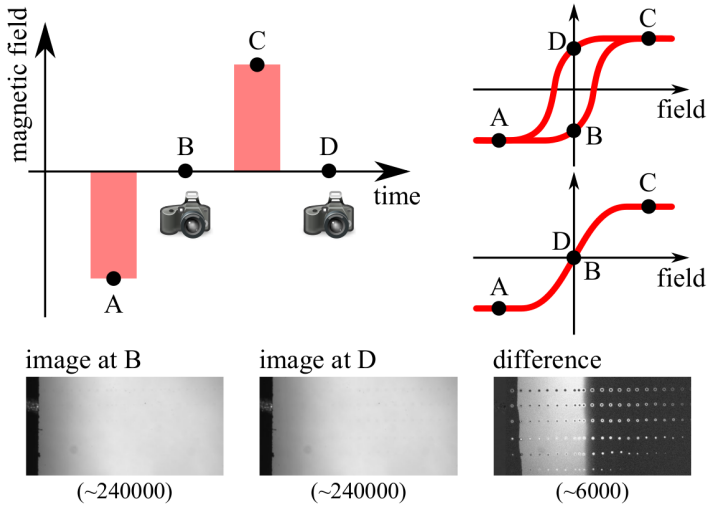


**Figure 3.4:** The idea of the technique called *remanence image*. The capital letters A–D denote states of the sample, obtained subsequently by field pulses. Images are taken at zero field, at points B and D. If the sample exhibits any remanence (upper loop), states B and D are different, which results in a difference in the respective images. At the bottom an example of two images and the difference between them is presented. Numbers of gray levels of the original images are indicated below. As the relative difference is rather low, for the presentation the contrasts were adjusted separately.

lower loop). One can extend this procedure as well, applying a field which is not limited to the two maximal values, but to take images after field pulses of gradually changing amplitude. In terms of Figure 3.4 it would mean, that after the field pulse A, saturating the sample in one direction, and taking a reference image B, a sequence of pulses C, E, ... is applied, followed by images D, F, ..., as it is shown in Figure 3.5. The very first image B is being subtracted from each following image, to increase the magneto-optical contrast. Sometimes this technique is called *remanence hysteresis*. It is very useful to visualize an evolution of the domain structure upon the changes of the magnetic field.

Another type of measurement is taking a series of images in the presence of a magnetic field – this way spatially-resolved hysteresis loops are recorded separately in each pixel of the camera. The difficulty of this technique lays in the usually strong influence of the magnetic field on the microscope objective (as paramagnetic glass is also subjected to magneto-optical effects), so the measured rotation does not come purely from the sample, but from the objective glass too. However, applying advanced image processing it is possible to get rid of that influence. Such procedures of image



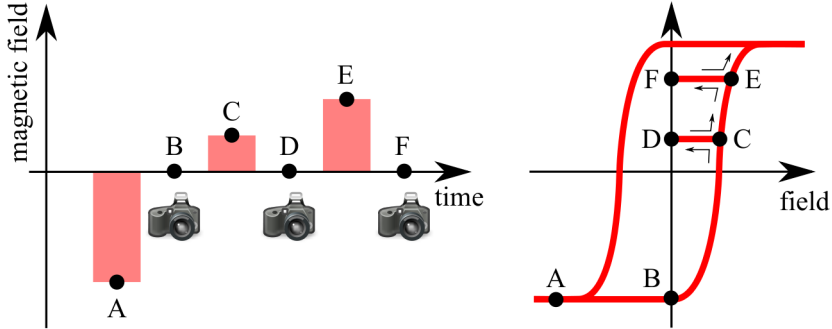


**Figure 3.5:** The procedure of recording the *remanence hysteresis*. Images are taken at zero field, after field pulses of gradually increasing amplitude. The first image *B* is being subtracted from each following images *D, F, ...*, to increase the magneto-optical contrast.

processing are presented in Appendix A.

### 3.4 Kerr milli-magnetometer

Principles of the Kerr milli-magnetometer are similar to the ones for the Kerr microscopy. The difference is the use of a laser as a light source and a photodiode instead of a camera, so the measured signal is averaged over a several micrometers area of the laser spot focused at the sample surface. Also, applying a modulation technique it is possible to get a much better signal-to-noise ratio. The *photoelastic modulator* (PEM) is a device that employs the photoelastic effect – due to a stress applied to a piece of crystal, its refractive index can change anisotropically, inducing some birefringence.

Again, employing Jones matrices, the final light polarization state in the Kerr milli-magnetometer setup can be written as:

$$\mathbf{E} \propto \bar{P}(\phi_A) \cdot \bar{S}(\Theta_K) \cdot \bar{R}(\varphi) \cdot \bar{P}(\phi_P) \cdot \mathbf{E}_0. \quad (3.11)$$

The light passes the polarizer and PEM, reflects from the sample, and goes through the analyzer.  $\bar{R}$  is the Jones matrix for the PEM as a retarder, as it introduces some

phase shift  $\varphi$  between the  $x$  and  $y$  components of light<sup>2</sup>:

$$\bar{R}(\varphi) = \begin{pmatrix} e^{i\varphi/2} & 0 \\ 0 & e^{-i\varphi/2} \end{pmatrix}. \quad (3.12)$$

For the configuration with an initial light polarization of  $\phi_P = \pi/4$  and the analyzer angle of  $\phi_A = \pi/2$ , in a similar way to the one presented in the previous Section, we get a formula for the intensity of the light recorded by a photodiode:

$$I \propto \frac{1}{2} - \theta_K \cos \varphi + \epsilon_K \sin \varphi. \quad (3.13)$$

The crucial fact in the modulation technique is that the retardation angle varies with time,  $\varphi(t) = \varphi_0 \sin \omega t$ , with a several kilohertz frequency and adjustable amplitude  $\varphi_0$ . Using the formulas for nested trigonometric functions:

$$\sin(\varphi_0 \sin \omega t) = 2 \sum_{k=1}^{\infty} J_{2k-1}(\varphi_0) \sin((2k-1)\omega t) \quad (3.14)$$

$$\cos(\varphi_0 \sin \omega t) = J_0(\varphi_0) + 2 \sum_{k=1}^{\infty} J_{2k}(\varphi_0) \cos(2k\omega t) \quad (3.15)$$

where  $J_i(x)$  are  $i$ -th order Bessel functions, we get, in development up to the second harmonic frequency:

$$I \propto \frac{1}{2} - \theta_K (J_0(\varphi_0) + 2J_2(\varphi_0) \cos 2\omega t) + \epsilon_K (2J_1(\varphi_0) \sin \omega t). \quad (3.16)$$

As was mentioned,  $\varphi_0$  is adjustable, so particularly it can be set to the value, where  $J_0(\varphi_0) = 0$  (this happens for  $\varphi_0 = 137.8^\circ$ ), to have clearly separated signals: the first harmonic oscillation is proportional to the Kerr ellipticity, the second one to the Kerr rotation.

Measuring the amplitude of a signal of a certain frequency is possible using a *lock-in amplifier*. This way, selecting the first or the second harmonic frequency, rotation or ellipticity can be easily studied. To get an absolute value of the Kerr rotation or the Kerr ellipticity angles, not a proportional quantity only, a simple operation could be done. The proportionality relation in Eq. (3.16) involves a certain constant to multiply all components at the right hand side. In particular, as this constant is identical in the  $dc$  component and the  $ac$  ones, dividing the measured amplitude of the first or the second harmonic oscillation by the measured  $dc$  component, the proportionality factor should vanish. The proper values of the Bessel function at  $\varphi_0$  could be also used.

<sup>2</sup>Typical examples of "static" retarders are: the *quarter-wave plate* with  $\varphi = \pi/4$ , the *half-wave plate* with  $\varphi = \pi/2$ , or compensators e.g. Babinet-Soleil's or Berek's, with an adjustable  $\varphi$ .

The described configuration with the given values of PEM, polarizer and analyzer angles is not the only one that allows to measure the Kerr effect. It is also possible to build set-ups in several different ways, that have been described and tested in Ref. [14].

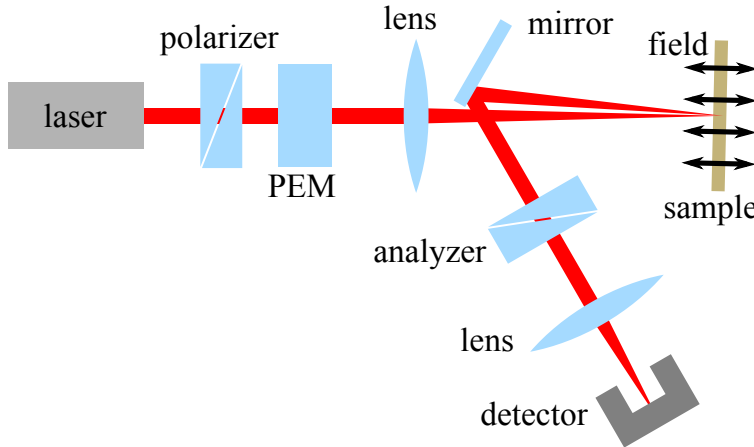


**Figure 3.6:** The scheme of the Kerr milli-magnetometer in the polar configuration. See the text for more details.

The setup used in our experiments exists in two main versions: for the PMOKE and the LMOKE/TMOKE measurements. The schemes are shown in Figures 3.6 and 3.7, respectively. In both cases the laser light is focused with a lens of a long focal length (to avoid the influence of a magnetic field on the optics) to a spot of about  $300 \mu\text{m}$  in diameter – this value is also a limit for the spatial resolution of the setups. The PMOKE configuration works with almost-normal light incident angle (less than  $1^\circ$ ), with the magnetic field perpendicular to the sample plane. In the LMOKE/TMOKE configuration the light comes at an angle of about  $45^\circ$  to the sample plane. The setup is equipped with two electromagnets perpendicular to each other, so the magnetic field can be applied in the light-incidence plane (LMOKE configuration) or perpendicular to it (TMOKE configuration), eventually in any direction in the sample plane, by a linear combination of the two orthogonal fields. In both setup configurations, for spatially-resolved studies, a sample can be moved in the plane perpendicular to the light direction, by two orthogonal motorized and computer-controlled translation stages. Additionally, a sample can be rotated around the axis parallel to the beam, what is relevant for the LMOKE/TMOKE configuration only. Rotation is realized by a motorized and computer-controlled rotation stage and owing to the two extra translation stages the pivot can be moved with respect to the sample.

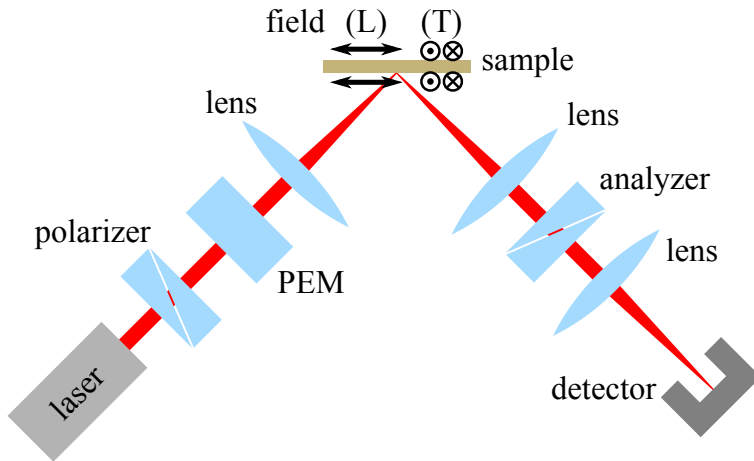


**Figure 3.7:** The scheme of the Kerr milli-magnetometer in a configuration used for longitudinal (L) and transversal (T) MOKE's studies, dependent on the direction of the applied magnetic field. See the text for more details.

### 3.5 Time-resolved magneto-optical setup

Ti:sapphire lasers are commonly used as a source of ultrashort (about 100 fs) laser pulses.  $\text{Ti}^{3+}$  ion dopants in an  $\alpha\text{-Al}_2\text{O}_3$  crystal have a very large gain bandwidth, which results in a wide wavelength tunability (typically 650 – 1100 nm, with the maximum of efficiency at 800 nm). Together with the mode-locking technique it allows to generate very short pulses, of duration down to tens of femtosecond, and a repetition rate of about 80 MHz. For pumping energy to the lasing medium, usually neodymium-doped gain media green lasers are used. Emitted femtosecond light pulses of average power of single watts, have a huge pulse power of tens of megawatt. Applying a regenerative amplifier it is possible to increase this power even further. The gain medium of the amplifier is pumped by multiple light passes and pulses, released with Pockels cells with repetition rate decreased to the kilohertz regime, have a peak power reaching several gigawatts, corresponding to energies of millijoules in a single pulse.

The basic idea of the time-resolved magneto-optical setup is splitting the laser pulses into a *pump* and a *probe*: the major part of energy travels with the pump beam to excite some process in a sample. The rest, with the probe one, reaches the sample after a certain delay time after the pump, probing the actual magnetization state with one of the magneto-optical effects mentioned before. Delay time is realized by simple mechanical changing the length of the light's path, taking advantage of the

speed of light:

$$\Delta t = \frac{2\Delta x}{c} \quad (3.17)$$

The factor of 2 comes from the fact, that with moving the stage with  $\Delta x$ , the light passes that distance twice (forth and back after reflection from a *retro-reflector* – a set of three mutually perpendicular mirrors, reflecting the light always back). Typical delay stages can be translated with sub-micrometer precision, so according to Eq. (3.17), a resolution of  $1\mu\text{m} \approx 7\text{ fs}$  can be reached, which is usually far better than the resolution limited by the pulse duration. As the dynamics in the pump-probe setup is studied stroboscopically, the most crucial condition is the full repeatability and reproducibility of processes triggered by subsequent incoming pump pulses.

In the pump-probe setup yet another method of probing the magneto-optical effects is often employed. Using a Wollstone prism, the probe beam after reflection from the sample is split into the two orthogonal polarizations, and recorded by two photodiodes separately. The relation of the detected signals to the Kerr effect can be shown with the Jones formalism, again. The initial equation has a form identical to Eq. (3.4), but involves different value of  $\phi_A$ . The Wollstone prism acts as two orthogonal polarizers, which in symmetrical “balanced” position of the prism are oriented at angles of  $\phi_A = +45^\circ$  and  $\phi_A = -45^\circ$  with respect to the initial polarization. Intensities recorded by the two photodiodes, employing Eqs. (3.4-3.6), are then:

$$I_{\pm} \propto \left( \frac{1}{2} \pm \theta_K \right) \quad (3.18)$$

with  $\pm$  signs for the diodes recording the  $+45^\circ$  and  $-45^\circ$ -polarized signals, respectively. The difference of these two signals is thus proportional to the Kerr rotation:

$$(I_+ - I_-) \propto 2\theta_K \quad (3.19)$$

To get an absolute value of the rotation instead of a proportionality relation, again a simple action can be performed. Dividing Eq. (3.19) by the sum of the intensities, the proportional constant vanishes and an equality is obtained:

$$\frac{I_+ - I_-}{I_+ + I_-} = 2\theta_K \quad (3.20)$$

To separate the effects of the pump beam exciting a sample from the static background, a chopper is mounted in the pump beam, to open and close it alternately with a certain frequency. This way the “excited” signal is referenced to the “not excited” one, when the chopper closes the pump, and they both alternate with the chopper frequency. The oscillating signal is treated by a lock-in amplifier as a sum of *ac* and *dc* components:

$$I_{\pm} = I_{\pm,dc} + \sqrt{2}I_{\pm,ac} \sin \omega t. \quad (3.21)$$

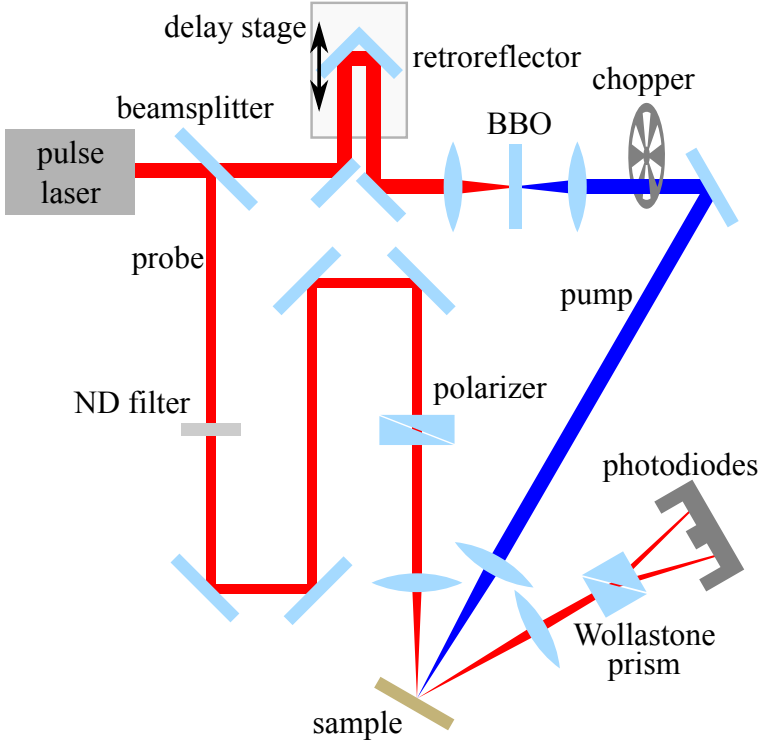


**Figure 3.8:** The scheme of the time-resolved pump-probe setup. See the text for details.

$I_{\pm,dc}$  and  $I_{\pm,ac}$  are the *dc* and *ac* signals that appear at the lock-in's outputs. An extra factor of  $\sqrt{2}$  comes from the fact, that a lock-in measures an *rms* signal, not the real amplitude. Further, we are interested in values of twice the amplitude of the *ac* signal, as this is the rotation change because of the exciting pump (difference between “excited” and “not excited”). In a balanced position of a Wollstone prism and the diodes the *dc* components for  $\pm$  are the same, so  $I_{+,dc} = I_{-,dc} =: I_{dc}$ . Taking all of these facts into account, the final form for the measured Kerr rotation is:

$$\theta_K = \frac{1}{\sqrt{2}} \frac{I_{+,ac} - I_{-,ac}}{I_{dc}}. \quad (3.22)$$

A scheme of the setup which was used in our work is shown in Figure 3.8. Laser pulses come from a regenerative amplifier with a repetition rate of 250 kHz. After a beamsplitter they split into the pump and the probe. The pump beam is the one that goes through the retro-reflector mounted on the delay stage. Both the pump and the probe meet together again focused with the lenses at the same place on the

sample surface, and after reflecting the probe goes further to the Wollstone prism and the photodiodes. Additionally, the pump beam wavelength (before the sample) is converted from 800 nm to 400 nm, using a  $\beta$ -barium borate (BBO) nonlinear crystal, to be able, using color filters, to cut out from the diodes any scattered pump light. The chopper, mounted in the pump beam, operates at a frequency of 300 Hz. An external magnetic field was applied to the sample with an electromagnet, making an angle with the sample surface in the range of  $\pm 10^\circ$ .

## References

- [1] A. Cho and J. Arthur, *Progress in Solid State Chemistry* **10, Part 3**, 157 (1975).
- [2] P. S. Pershan, *J. Appl. Phys.* **38**, 1482 (1967).
- [3] A. K. Zvezdin and V. A. Kotov, *Modern Magneto-optics and Magneto-optical Materials* (Institute of Physics Publishing, London, 1997).
- [4] Š. Višňovský, *Optics in Magnetic Multilayers and Nanostructures* (CRC Press/Taylor & Francis, 2006).
- [5] P. N. Argyres, *Phys. Rev.* **97**, 334 (1955).
- [6] M. Faraday, *Philos. Trans. R. Soc. London* **136**, 1 (1845).
- [7] J. Kerr, *Phil. Mag.* **3**, 321 (1876).
- [8] W.-K. Tse and A. H. MacDonald, *Phys. Rev. Lett.* **105**, 057401 (2010).
- [9] R. Azzam and N. Bashara, *Ellipsometry and Polarized Light* (Elsevier, Amsterdam, 1987).
- [10] P. Yeh, *Surf. Sci.* **96**, 41 (1980).
- [11] Š. Višňovský, *Czech. J. Phys.* **36**, 625 (1986).
- [12] Š. Višňovský, *Czech. J. Phys.* **41**, 663 (1991).
- [13] M. Nyvlt, Ph.D. thesis, Charles University, Prague (1996).
- [14] S. Polisetty, J. Scheffler, S. Sahoo, Y. Wang, T. Mukherjee, X. He, and C. Binek, *Review of Scientific Instruments* **79**, 055107 (2008).





---

## Ultrafast manipulation of magnetic anisotropy

---

In this Chapter we present the studies of light-induced reversible changes of the magnetic anisotropy in an ultrathin cobalt wedge-shaped film sandwiched between platinum layers. All-optically induced magnetization precession was used as a fingerprint of the ultrafast pulse-induced modification of the anisotropy. As in such wedged magnetic layer the static anisotropy changes continuously with the film thickness [1], it allowed us to clearly distinguish the contribution of the light-induced anisotropy change to the excitation process. Varying the applied magnetic field helped us further to separate the different contributions. Even though the light-induced changes of magnetic anisotropy have been already discussed [2–4], there was no universal approach that could be applied to its description. In this Chapter we therefore study this process in details, using a simple model that allows to describe the experimental results and derive the temperature dependence of the interface anisotropy contribution. The fact that the anisotropy changes at the same time scale as the magnetization, is found to be consistent with our data.

The results presented in this Chapter are published in J. Kisielewski, A. Kirilyuk, A. Stupakiewicz, A. Maziewski, A. Kimel, Th. Rasing, L. T. Baczewski and A. Wawro, *Laser-induced manipulation of magnetic anisotropy and magnetization precession in an ultrathin cobalt wedge*, Phys. Rev. B **85**, 184429 (2012).

## 4.1 Experimental details

### Sample

The sample studied in this Chapter was produced by the MBE technique. The following structure was grown on a sapphire ( $11\bar{2}0$ ) substrate: (i) buffer layer of 20 nm Mo(110) deposited at temperature  $1000^\circ\text{C}$ ; (ii) underlayer of 20 nm Pt(111); (iii) a wedge of Co(0001) of 0–3 nm thickness range; (iv) overlayer of 8 nm of Pt to prevent the Co film from oxidation. All the Pt and Co layers were deposited at room temperature. The structure of the sample is schematically shown in Figure 4.1.

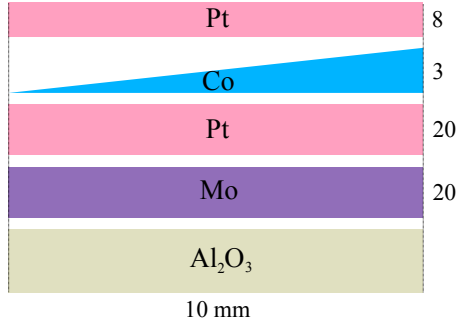


**Figure 4.1:** The scheme of the sample. Values of thicknesses are given in nanometers.

### Static measurements

The static magneto-optical and magnetic properties of the sample were initially characterized by Kerr milli-magnetometer, both in polar and longitudinal configuration. Using the PMOKE milli-magnetometer hysteresis curves were measured along the Co wedge with 0.2 mm-step, at room temperature. Selected loops, labeled with the numbers of measured points, are displayed at the top of Figure 4.2. Every loop was analyzed afterward in order to derive the values of the following parameters: Kerr rotation at saturation and at remanence, the coercive field and the saturation field. Profiles of these quantities are shown in Figure 4.2. Exploiting the measured thickness-dependence of the saturation field, the thickness of the spin reorientation transition (SRT),  $d_0 = 2.3$  nm and room-temperature value of the surface anisotropy constant  $K_s = (1.00 \pm 0.02)\text{mJ}/\text{m}^2$  were determined, keeping the value of the bulk anisotropy coefficient  $K_v = 0.41\text{MJ}/\text{m}^3$  for *hcp* bulk cobalt, taken from Refs. [1, 5].

The sample was examined also with LMOKE milli-magnetometer. The external magnetic field was applied in the sample plane and in the plane of beam incidence. The set of hysteresis curves was recorded rotating the sample around a certain point at the Co thickness of 2.8 nm, with  $10^\circ$  step. The shape of curves was found to be

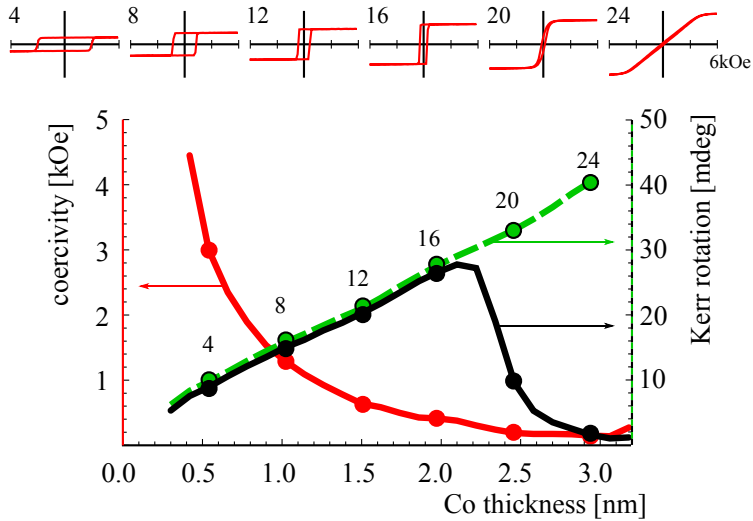


**Figure 4.2:** Thickness-dependence of coercive field (red), and Kerr rotation at remanence (black) and at saturation (dashed green), derived from a set of PMOKE hysteresis loops. The points labelled with the numbers correspond to the hysteresis loops shown at the top.

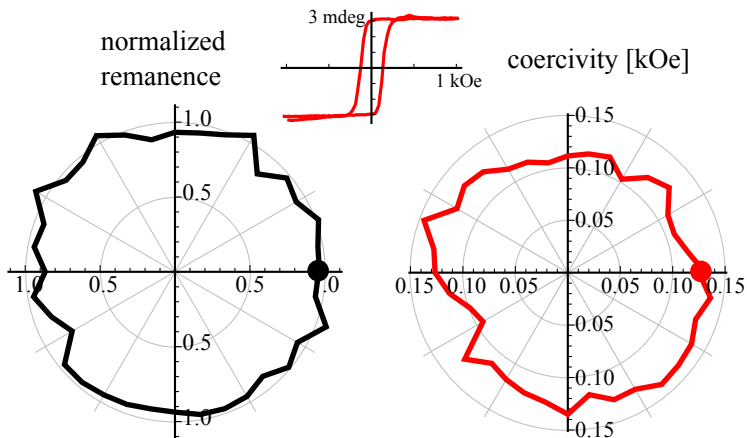


**Figure 4.3:** Normalized remanence and coercive field, derived from a set of LMOKE hysteresis loops, as a function of the sample orientation angle. Top: an example of a hysteresis loop at the selected point (at the orientation angle equal to 0).

angle-independent, which means an absence of an in-plane anisotropy. An example of the hysteresis curve and rotational profiles of normalized remanence (divided by the saturation value of the Kerr rotation) and coercive field are shown in Figure 4.3.

### Dynamics measurements

The magnetization dynamics was studied with the classical pump-probe setup. Focused beam diameters were equal to 60 and 30  $\mu\text{m}$  for pump and probe respectively, which was determined with a knife-edge method (see Appendix B), assuming a single Gaussian-shape of energy density distribution. The maximal value of the energy density of the focused pump beam was found to be  $(2.6 \pm 0.3)$   $\text{mJ}/\text{cm}^2$ . The angles of incidence were  $0^\circ$  for the pump and  $40^\circ$  for the probe and for that configuration PMOKE is still a dominant effect, so the perpendicular component of the magnetization was probed. The Kerr rotation was calculated using the formalism presented in Chapter 3.5 (Eq. (3.22)), and afterward it was divided by the maximal Kerr rotation derived from the static PMOKE measurements, in order to express the magnetization changes as a percentage of the total magnetization at room temperature. The delay stage was moved over a range of 10 cm, so according to Eq. (3.17) processes on a time scale up to 0.67 ns were available to be studied. An external magnetic field up to 3 kOe was applied to the sample, making an angle of  $\pm 10^\circ$  with the sample surface.

The dynamics of magnetization was studied as a function of the Co thickness (moving the sample along the Co wedge with respect to the laser beams) and the amplitude of the external magnetic field. For each used value of the Co thickness, the static hysteresis curve at that tilted field was checked initially, and the subsequent studies of the dynamics were confined to these fields being high enough to saturate the sample, to observe a homogeneous behavior in a monodomain state.

## 4.2 Results

Oscillations of the magnetization triggered by the pump pulse were found to occur, which can be interpreted as a laser-induced magnetization precession, described in Chapters 1.1.4 and 2.2.1. Although the magnetization precesses in three-dimensional space, with the PMOKE the perpendicular component was probed only.

To derive the parameters that characterize the measured oscillation, the function

$$m(t) = A \sin(2\pi ft + \phi) e^{-\delta t} + B e^{-\gamma t} \quad (4.1)$$

was fitted to the measured data. This equation describes the sinusoidal oscillation with amplitude  $A$ , frequency  $f$  and phase  $\phi$ , damped with the exponential term characterized by  $\delta$ , related to the Gilbert damping constant in the LLG equation as

$$\alpha = \frac{\delta}{2\pi f}. \quad (4.2)$$

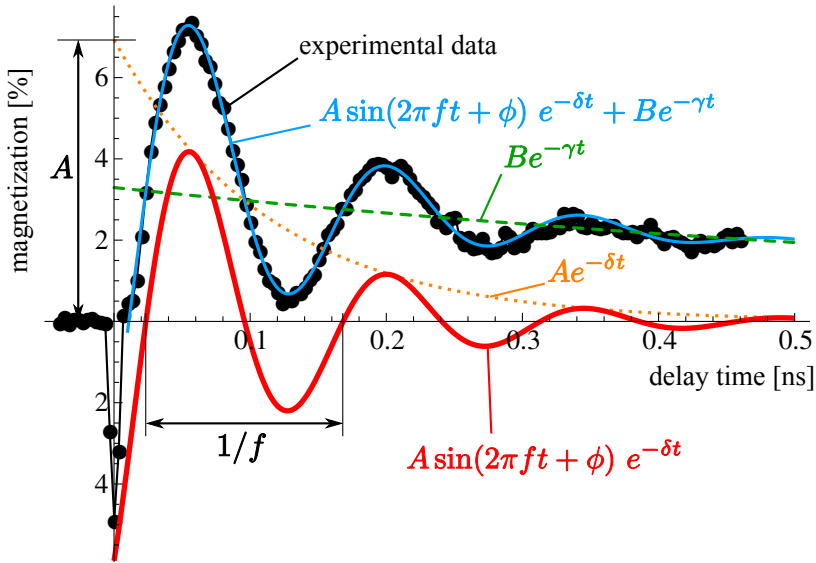


**Figure 4.4:** The measured precessional curve for the Co thickness of 2.28 nm and the external magnetic field amplitude of 1.45 kOe (black points). The out-of-plane magnetization component was probed, the field was applied making an angle of about  $10^\circ$  with the sample plane. With the color lines the data analysis is demonstrated: solid blue – the fit according to Eq. (4.1); dashed green – a nonmagnetic background; thick solid red – a pure precessional curve without the background; dotted orange – an envelope which represents the Gilbert damping. The magnetization changes are expressed as a percentage of the magnetization saturation value at room temperature.

The last term in Eq. (4.1) corresponds to a nonmagnetic background connected with pump-induced changes of the reflectivity. An example of measured curve is presented in Figure 4.4, together with a fit according to Eq. (4.1) and an explanation of the meaning of the parameters. In Figure 4.5 the dependence of the precessional behavior is shown, as a function of the Co thickness and the magnetic field amplitude. The nonmagnetic background has been already eliminated (see the red curve in Figure 4.4).

### 4.3 Calculations

To understand the non-trivial dependence of the laser-induced precession on various parameters, a theoretical model was developed. The magnetization precession with damping is governed by the Landau-Lifshitz-Gilbert (LLG) equation, already

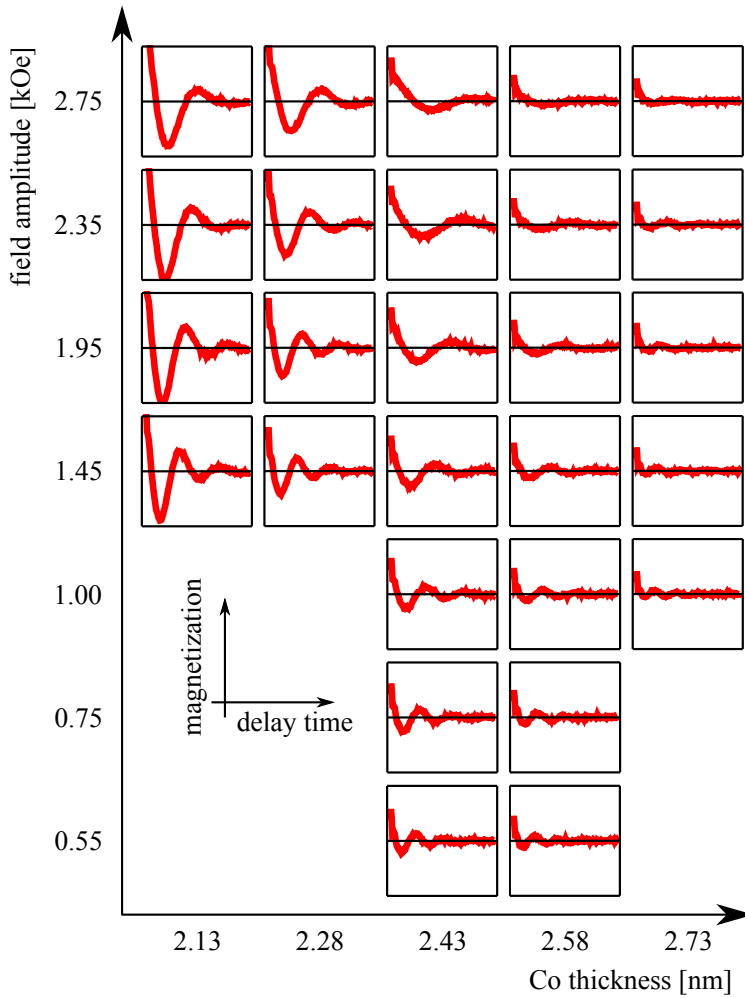


**Figure 4.5:** Measured oscillation of the magnetization, as a function of the Co thickness (columns) and magnetic field amplitude (rows). Scales of both axes for all the sub-plots are identical.

introduced in Chapter 1.1.4:

$$\frac{d\mathbf{M}}{dt} = \gamma (\mathbf{M} \times \mathbf{H}_{\text{eff}}) + \frac{\alpha}{|\mathbf{M}|} \left( \mathbf{M} \times \frac{d\mathbf{M}}{dt} \right). \quad (4.3)$$

$\mathbf{H}_{\text{eff}}$  is an effective magnetic field – a vector sum of all magnetic fields that affect the sample. In our case it consists of the externally applied magnetic field and the total anisotropy field:

$$\mathbf{H}_{\text{eff}} = \mathbf{H}_{\text{ext}} + \mathbf{H}_{\text{ani}}. \quad (4.4)$$

Laser-induced thermal changes of the total anisotropy field are considered as a trigger for the precession behavior, as was described in Chapter 2.2.1. All contributions to the anisotropy field,  $M$ ,  $K_v$  and  $K_s$  (see Eq. (1.17)) are supposed to be temperature-dependent. Due to the incoming pump pulse, that suddenly increases the temperature of the sample, their values change, making  $H_{1\text{eff}}$  (Eq. (1.17)) and thus  $\mathbf{H}_{\text{ani}}$  length also changed. Providing the external field  $\mathbf{H}_{\text{ext}}$  applied constantly at a direction different than  $\mathbf{H}_{\text{ani}}$ , this results in a sudden change of the effective magnetic field direction, thus a non-equilibrium orientation of the magnetization and a triggering of the precession.

### 4.3.1 Role of temperature

To calculate the temporal dependence of the temperature correctly, the three-temperature model (3TM), already mentioned in Chapter 1.1.2, should be involved. However, exact solution of the problem would require the use of numerous parameters, such as individual temperatures and heat capacities for electrons, lattice, and spins, and coupling parameters between the respective reservoirs. Moreover, thermalization between baths in adjacent layers happens with different efficiencies. In order to simplify this model, we made the following assumptions. The only difference in considering either the 3TM or the model with one temperature common for all baths (1TM), refers to the first few picoseconds, until the baths have thermalized. At longer times scales, calculations within both approaches should yield identical results. As we are interested in several (1–10) GHz dynamics, i.e. the processes that happen on the time scale of several tens of picoseconds, processes of the time scale of a few picoseconds are of less importance. Therefore we assume that all baths at a certain depth in the sample are described by the same temperature and the heating occurs immediately after the light pulse and simultaneously in all metallic layers.

The method of calculations of the temperature dynamics within this 1TM approach is described in Appendix C. The heat equation (Eq. (C.9)) is being solved numerically, with the values of the thermodynamical parameters (thermal conductivities  $\tau(z)$  and heat capacities  $C(z)$ ) taken for room temperature and for bulk materials. Additionally, some further simplifications can be assumed for the case of our studies.

As far as we are interested in the dynamics in a few-hundreds picoseconds, the influence of the ambient air can be neglected, as the mean collision time of air particles is, at normal conditions, about 100–200 ps – on such a time scale the air cannot substantially take part in cooling down the sample. Moreover, for the geometry of the sample given in the experiment, with a several micrometers-large beam size and a several nanometer-thick metallic layer, the planar heat transfer happens on a several microseconds time scale – orders of magnitude slower than the perpendicular one. Thus, for the calculation of the few hundreds of picoseconds dynamics involved in the experiment, the planar heat transfer can be neglected. A quantitative explanation is presented in Appendix C.3.

From the calculated depth-profiles of the temperature (shown in Figure C.4), the temperature dynamics in the Co layer itself was taken, as the one being important for the magnetization dynamics. It allowed to calculate the magnetization dynamics, using the experimental  $M(T)$  curve reported by Kuz'min [6]. Both temporal dependences, of the temperature and the magnetization in the Co layer are plotted in Figure 4.6. The values of the magnetization saturation at zero temperature

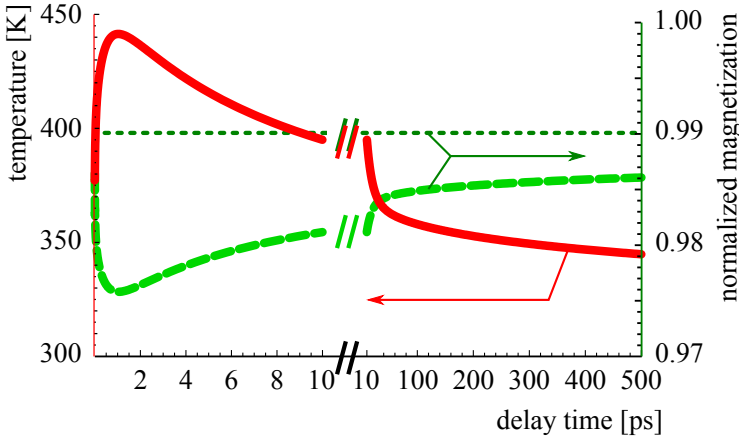


**Figure 4.6:** Temporal dependences of temperature in the Co layer (red) and the magnetization (dashed bright green), calculated using 1TM. Magnetization is normalized to its zero-temperature value. With a dashed dark green line a room temperature value of the magnetization, according to Kuz'min [6] is plotted.

$M(0) = 1.45 \times 10^6 \text{ A/m}$  and the Curie temperature  $T_C = 1388 \text{ K}$  were taken as for bulk cobalt [7], and were specified as thickness-independent, as the layer was thick enough [8]. The calculated changes of the magnetization are apparently small, what makes the LLG equation eligible, as in general it does not apply to situations with changing value of magnetization saturation [3].



Thermal changes of the anisotropy constants are more problematic, as was discussed in Chapter 2.2.1. In the simplest approach, using the first anisotropy constant only, the exponent in the temperature dependence of the anisotropy constants (Eq. (2.4)) should be  $n = 3$  for both  $K_v$  and  $K_s$ . In our studies, not to determine the surface magnetization or stresses, which in fact would be problematic, we assumed that  $K_s$  is proportional to a bulk magnetization with some effective exponent  $n$ , which stayed as a free parameter and was determined from the fitting procedure. Room temperature values of anisotropy constants were discussed in Section 4.1.

### 4.3.2 Magnetization precession

#### Boundary conditions

As a boundary conditions for the laser-induced magnetization precession, the initial (before the pump pulse) magnetization orientation was calculated. Before the excitation the magnetization is expected to point along the effective magnetic field (Eq. (4.4)), which in turn is magnetization orientation-dependent (Eq. (1.16)). That non-trivial equation was solved numerically, for given combinations of the magnetic field amplitude and the Co thickness. In Figure 4.7 the calculated initial magnetization orientations as values of  $\cos(\theta)$  are plotted with red dashed lines, as a function of Co thickness, for several values of external field amplitude, including zero (the abrupt change at the SRT). The red points correspond to the combinations of the parameters (thickness and field amplitude) which were used in the experiment. The real zero-field dependence, equivalent to the measured normalized remanence (remanence divided by saturation) is also presented with the black points. Apparently between the measured and calculated zero-field curves there is some disagreement just above the SRT thickness. That is the region, where the second anisotropy constant ( $K_2$ ), that was not involved in that calculations, could eventually play a role. As mentioned in Chapter 1.2.2,  $K_2$  is responsible for an easy-cone state, i.e. for orienting the magnetization at some angle with respect to the sample plane. However, in our case a tilted external magnetic field itself is the factor that pulls the magnetization out of the plane, regardless of  $K_2$  (above the SRT most of the red points overlap with the black ones). This means, that from the point of view of our dynamic experiment,  $K_2$  is insignificant, and the approximation with  $K_{1\text{eff}}$  only describes the observed effect well.

#### Solving LLG equation

As an input for the calculations, beyond the above-specified thermal and temporal dependencies, the experimental values of the external magnetic field orientation and amplitude, the Co thickness, and Gilbert damping were taken. All connections between the parameters are schematically depicted in Figure 4.8. The LLG equation

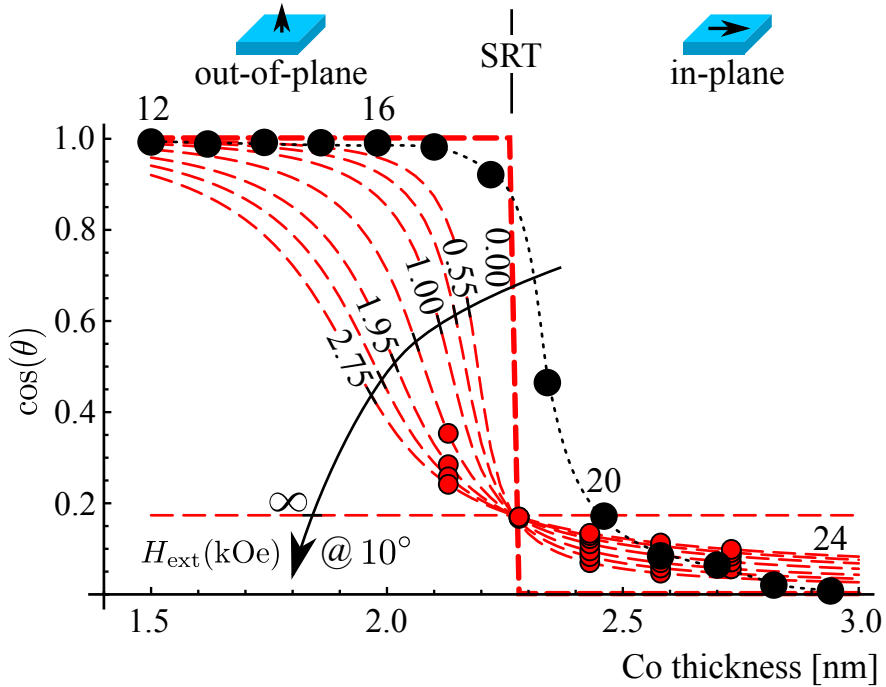


**Figure 4.7:** The static preferred magnetization orientation in the studied sample, as a function of Co layer thickness: at zero field (i.e. normalized remanence), measured (black points and dotted line as a guide to the eye) and calculated within the first anisotropy constant approximation (red thick dashed line). That dependence was also determined for the configuration of pump-probe measurements – at the presence of the external magnetic field applied at the angle of  $10^\circ$  to the sample plane (red dashed lines; field amplitude values: 0.55, 0.75, 1.00, 1.45, 1.95, 2.35, 2.75 kOe and additionally  $\infty$ ). The specified fields amplitudes and Co thicknesses were used in the dynamics measurement (red points).

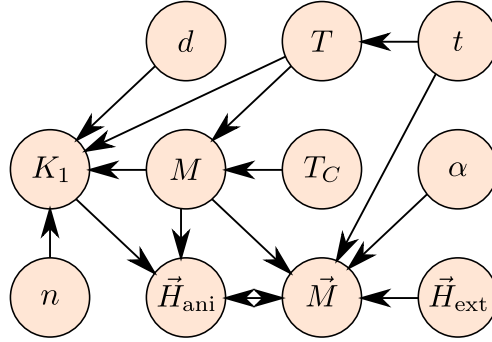


**Figure 4.8:** Scheme of connections between the main parameters used in calculations: Co thickness ( $d$ ), temperature ( $T$ ), time ( $t$ ), anisotropy constant ( $K_1$ ), magnetization saturation ( $M$ ), Curie temperature ( $T_C$ ), Gilbert damping ( $\alpha$ ), exponent in thermal dependence of anisotropy ( $n$ ), total anisotropy field ( $\vec{H}_{\text{ani}}$ ), magnetization vector ( $\vec{M}$ ) and external magnetic field ( $\vec{H}_{\text{ext}}$ ).

was solved numerically, using the author’s software, written in Wolfram Mathematica. For each combination of field amplitude and Co thickness, which was used in the experiment, the three-dimensional temporal behavior of the magnetization was obtained. In Figures 4.9 and 4.10 an example of the laser-induced precession is shown, calculated according to the presented model, with arbitrary values of parameters.

In order to compare the calculations directly with the experimental behavior, the out-of-plane component of the magnetization was taken into account for further proceeding. The exponent of the temperature dependence of the surface anisotropy constant (Eq. (2.4)) was the only free parameter. A single value of  $n$  was chosen to make all calculated curves fit the measured data simultaneously.

## 4.4 Discussion

The value of the exponent was found to be  $n = (3.2 \pm 0.4)$ , and it agrees well with the value of 3, derived according to Callen and Callen [9], considering the first anisotropy constant. Unfortunately, the temperature range, which was “tested” in the experiment (the temperature increase induced by the pump pulse) was rather narrow. Despite the above-mentioned agreement, it is rather hard to state any general dependence, bearing in mind all restrictions listed in Chapter 2.2.1. A confirmation using a broader temperature range would be problematic. Either in statics, applying elevated temperatures by a furnace, or in dynamics, increasing the pump beam intensity, it would be dangerous for the sample due to annealing effects – irreversible changes of the sample structure. In fact, such a kind of modification, influencing also the magnetic

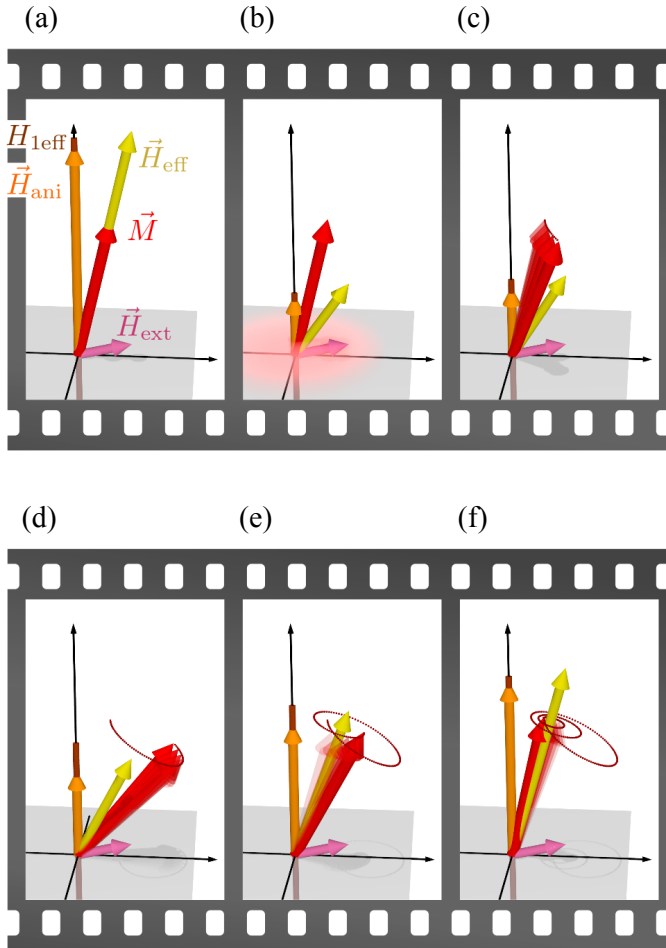


**Figure 4.9:** Demonstration of the process of the laser-induced magnetization precession, calculated according to the presented model using arbitrary values of all parameters – selected frames of the dynamics: (a) initial orientation of the magnetization  $\vec{M}$ , along the effective magnetic field direction  $\vec{H}_{\text{eff}}$ ; the anisotropy field vector  $\vec{H}_{\text{ani}}$  and  $H_{1\text{eff}}$  (see Chapter 1.2.3) are also specified; (b) the laser pulse changes suddenly the length of  $\vec{H}_{\text{ani}}$ ; (c) the laser pulse has already passed, but the temperature is still elevated and the effective anisotropy field length still reduced; the magnetization starts to precess; (d-f) the magnetization continues the precessional movement along the gradually changing direction of the effective magnetic field.

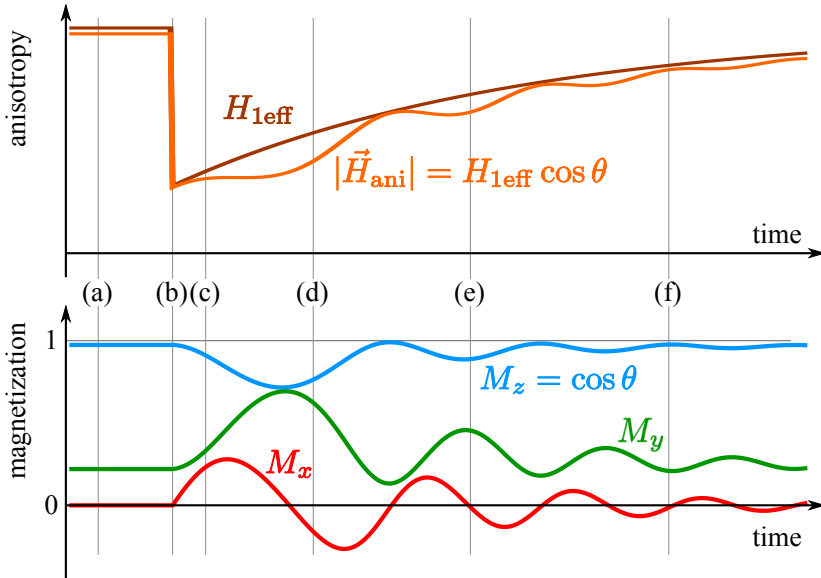


**Figure 4.10:** Demonstration of the process of the laser-induced magnetization precession, calculated according to the presented model using arbitrary values of all parameters – plots of temporal dependence of the anisotropy and magnetization components; the letters (a–f) refer to the respective frames in Figure 4.9.

properties, is the main goal of the next Chapter.

Comparison of the experimental precessional curves (with non-magnetic contribution subtracted) with the calculation performed within the presented model, for selected values of the Co layer thickness and magnetic field amplitude and the found exponent value of 3.2, is shown in Figure 4.11. All measured and calculated curves were represented by the derived frequencies and amplitudes of the precession. In order to derive parameters, the calculated curves were treated with the same method as the measured ones (Eq. (4.1)). A comparison is demonstrated in Figures 4.12 for frequency and 4.13 for amplitude. The experimental values, due to numerous measured points in the precessional curves, were determined quite precisely, and their error bars are smaller than the size of the points. On the contrary, the error bars of the calculated values are rather large, as numerous experimental parameters were involved in the calculations. Nevertheless, the general agreement is satisfactory, and the fact, that there was only one fitting parameter, should be emphasized here.

It is worth noting that the amplitude of the precession is the only  $n$ -sensitive parameter, and in fact it was used for the fitting procedure, while the frequency hardly

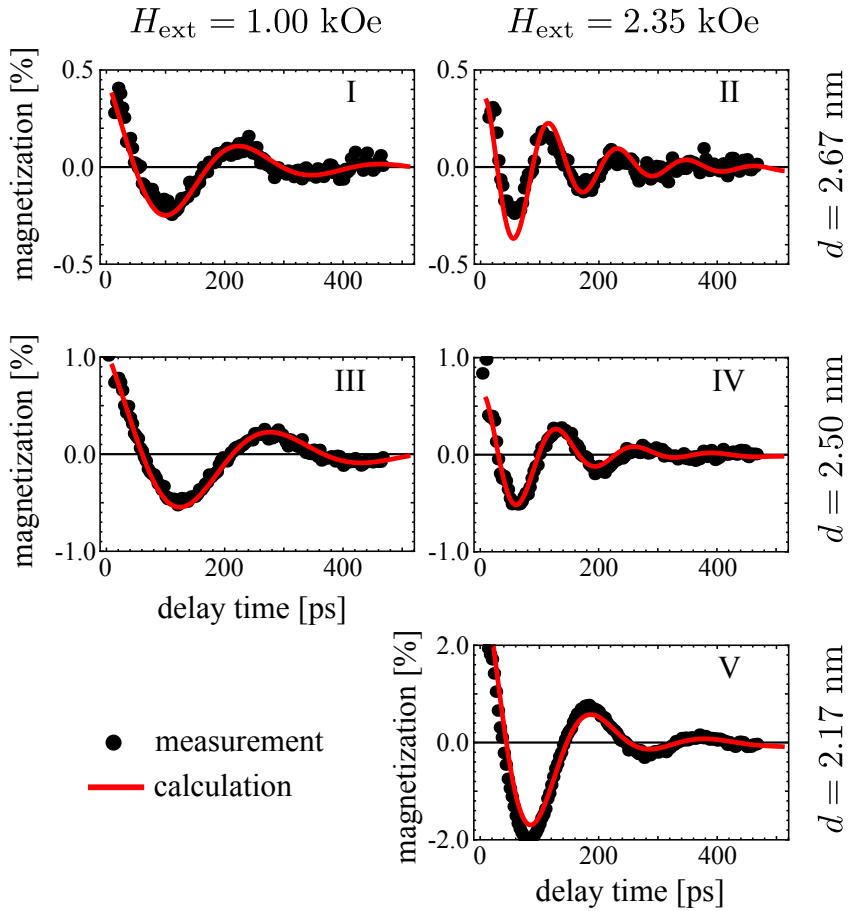


**Figure 4.11:** The measured (black points) and calculated (red lines) precession for selected thicknesses of the Co layer (rows) and magnetic field amplitude (columns). Units of vertical axes are expressed as percentage of magnetization saturation.

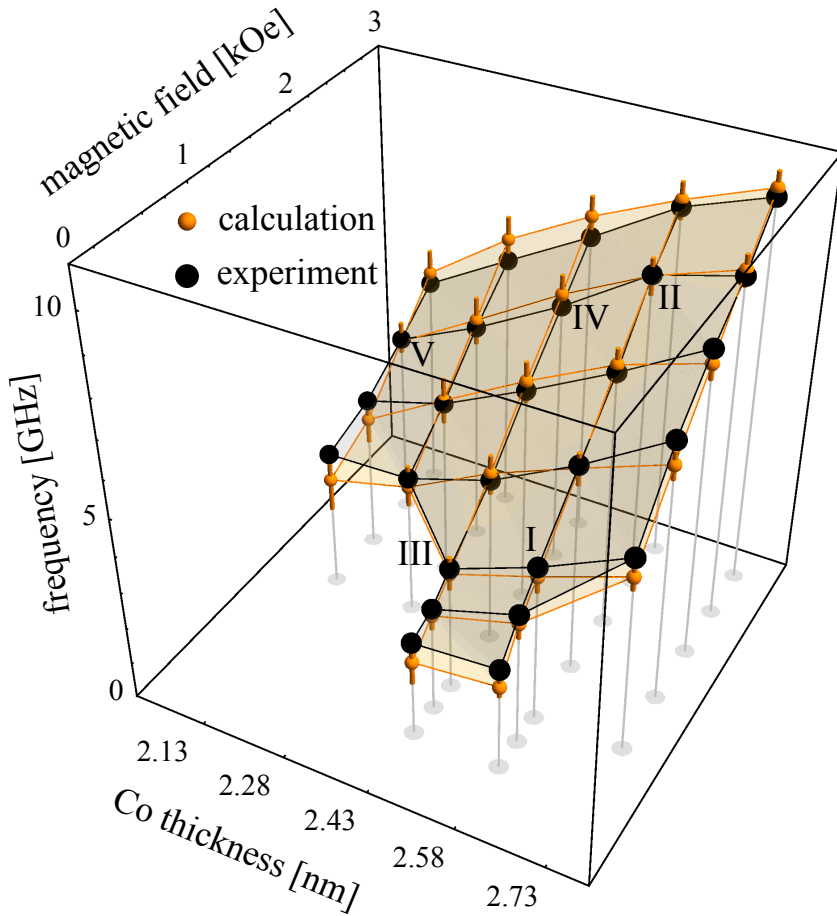


**Figure 4.12:** Frequency of measured (black) and calculated (orange) precession, as a function of Co layer thickness and magnetic field amplitude. Error bars: for the experimental points they are smaller than the size of the points; for the calculated points they are estimated from the errors of the particular experimental parameters involved in the calculations. Curves for points marked with Roman numbers I–V are plotted in Fig. 4.11.

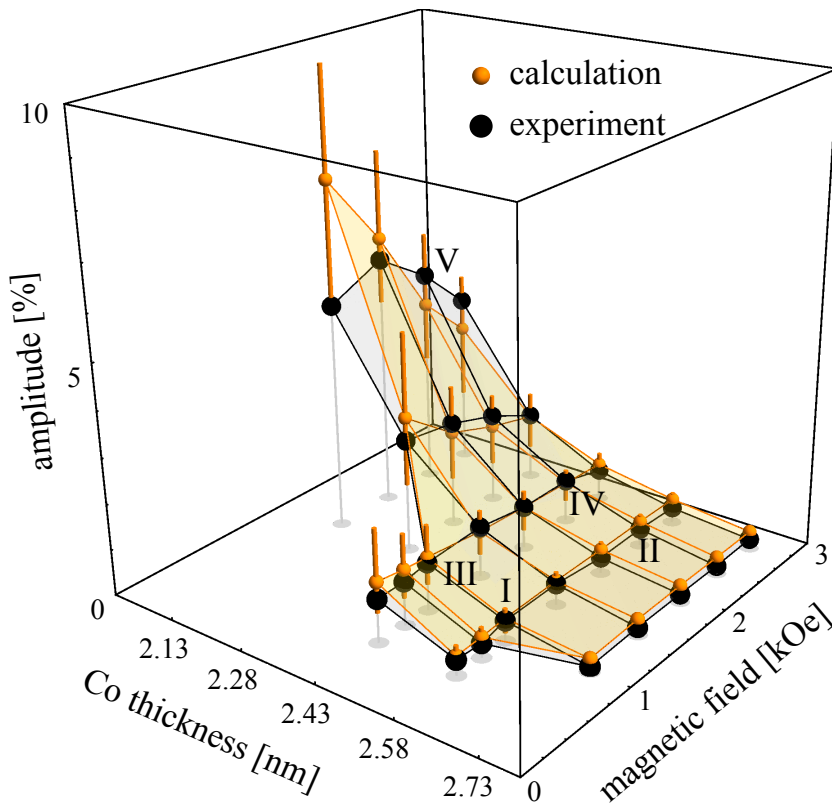


**Figure 4.13:** Amplitude of measured (black) and calculated (orange) precession, as a function of Co layer thickness and magnetic field amplitude. Units of amplitude are the percentage of magnetization saturation. Error bars: for the experimental points they are smaller than the size of the points; for the calculated points they are estimated from the errors of the particular experimental parameters involved in the calculations. Curves for points marked with Roman numbers I–V are plotted in Fig. 4.11.



changes with  $n$ . Analyzing the other parameters used in the model we found, that there are groups of parameters affecting either the amplitude or frequency more effectively. The amplitude of the precession depends on all the parameters playing a role in the dynamics: the temperature-dependent anisotropy field and magnetization saturation, the exponent, the Curie temperature and the incident energy intensity (which affects the initial temperature increase). Surprisingly, a negligible influence of the rate of temperature changes on the amplitude was found. On the other hand, the frequency is not sensitive to the above mentioned quantities, whereas it is very sensitive to the initial values of the anisotropy field. The phase of the oscillations is the same for all curves, both in the experiments and in the calculations. The explanation of this fact lays in the tendency of changes of the effective anisotropy field. According to Eq. (1.17), positive contributions of  $K_v$  and  $K_s$  compete with the negative demagnetization term, but they decrease faster with temperature than the demagnetization (see Eq. (2.4)). A positive effective anisotropy field (easy axis case) decreases with heating, while a negative one (easy plane case) – increases its length (and becomes “more” negative). In both situations it results in the same tendency of changes of the effective magnetic field with respect to the magnetization orientation. Thus the magnetization precesses always in the same direction, which naturally results in the observed constant phase. The Gilbert damping  $\alpha$  was not a subject of theoretical consideration, but as mentioned earlier, the measured values were used for the calculations. Nevertheless it did not affect the frequency and amplitude too strong. It changes from about 0.1 at the highest thickness to 0.4 at the smallest one, in agreement with the tendency already reported before [4].

The calculations within the developed model can be compared with existing theories, describing similar phenomena. The ferromagnetic resonance (FMR) precession in uniaxially-anisotropic ultrathin films is presented in [10]. However, to make a comparison as simple as possible, we approximate our configuration by an in-plane external magnetic field, instead of a tilted one. Then the formula for the FMR precession frequency becomes very simple [11] – rewritten in terms of our definitions, it appears as follows:

$$f = \frac{\gamma}{2\pi} \sqrt{H_{\text{ext}} (H_{\text{ext}} - H_{1\text{eff}})}. \quad (4.5)$$

Aiming at a qualitative comparison only, the static values of  $H_{1\text{eff}}$  (before the pump-pulse) can be used, as in fact their thermal changes with our experiment are estimated to be relatively small. In Figure 4.14(a) the values of precession frequency, experimental and calculated according to Eq. (4.5), are compared. The qualitative agreement is visibly good and the general tendency of changes is reproduced. Concerning the precession amplitude, there is no simple formula for a qualitative comparison. Speaking roughly, the observed amplitude is proportional to the angle between the effective magnetic field and the magnetization vector. The static orientation of the effective field is useless this time, as the magnetization vector points initially along this direc-

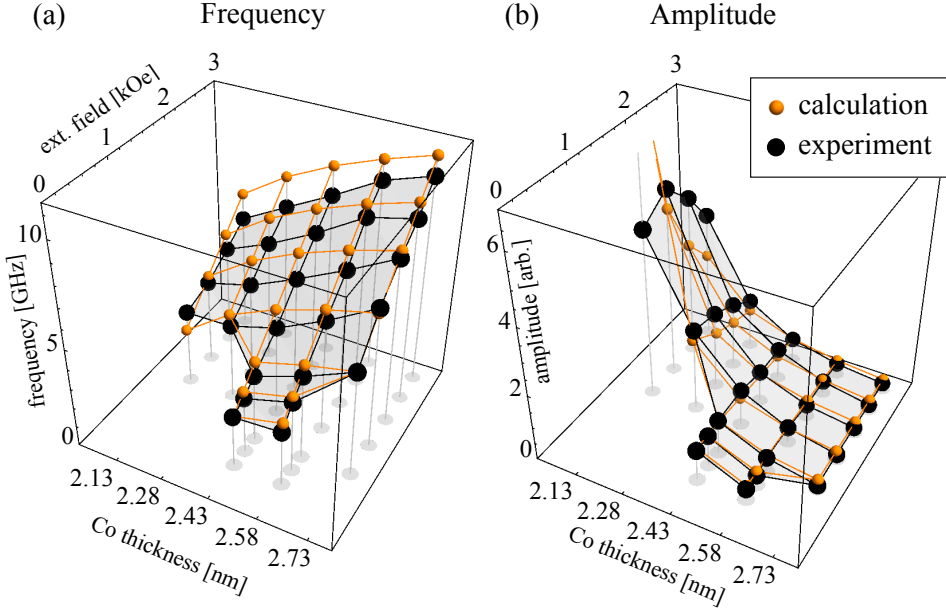


**Figure 4.14:** Comparison of frequency (a) and amplitude (b) of precession, derived from the pump-probe experiment and from simplified theories. See the text for details.

tion. Instead, we consider the situation when, according to our model of temperature dynamics, the change of the effective field is maximal and the magnetization has not yet started the precession, i.e. 1–2 ps after the pump pulse (see Figure 4.6). In Figure 4.14(b) the experimental values of amplitude and the calculated values of the angle  $\phi_{\{\mathbf{H}'_{\text{eff}}, \mathbf{M}\}}$  between the thermally-changed orientation of the effective magnetic field  $\mathbf{H}'_{\text{eff}}$  and the initial (static) magnetization  $\mathbf{M}$ , are presented. Due to the fact, that in the experiment we study the  $\hat{z}$ -component of magnetization, values of angle  $\phi_{\{\mathbf{H}'_{\text{eff}}, \mathbf{M}\}}$  were also multiplied by a cosine of the actual magnetization orientation angle. As a proportionality relation is presented, to show a qualitatively fair agreement, the calculated values were additionally multiplied by a certain constant number. Such a thickness dependence of the amplitude can be easily understood. For high Co thicknesses (above  $d_{SRT}$ ), the magnetization points nearly in-plane (it is slightly lifted up by the tilted external magnetic field). In this configuration the effective anisotropy field is low, as multiplied by a cosine of almost-right angle of magnetization orientation (see Eq. (1.16)), thus also its thermal changes and further the precession amplitude are low. For low Co thicknesses (below  $d_{SRT}$ ), on the contrary, a larger anisotropy field and its thermal changes contribute more significantly to the changes of effective magnetic field, yielding larger amplitudes of oscillations.

The proposed temperature dependence of anisotropy, as  $K(T) \propto M(T)^n$ , seems to be supported by a reasonable argumentation (see Chapter 2.2.1). Magnetic anisotropy, through the spin-orbit interaction coupled with the spins, is being weakened with the thermal fluctuations of the spin system. For this reason it is expected to follow the magnetization changes on the same timescale, i.e. according to the dynamics of the spin bath temperature (in terms of the 3TM) – on a few-picosecond time regime. On the other hand, the energy of visible (or near-visible) light, used to excite the magnetic systems in our pump-probe experiments, is too low to affect directly the electrons of deeper orbitals, which take part in mechanisms of anisotropy, so other channels of affecting the magnetic anisotropy by laser light are rather unavailable.

The found efficiency of the light-induced anisotropy changes, represented by the measured amplitude of the magnetization precession, is quite low. To make it higher – which can be eventually applied for the magnetization switching via half period precession [12] – a higher intensity of the pump pulse would be required. However, higher light intensities may lead to irreversible changes of the sample structure. Another way is to use materials of lower Curie temperature. Then, excitation with the same pump pulse parameters, resulting in the same temperature increase, would lead to more distinct changes of the magnetization and further the anisotropy constants. In our sample, of a relatively thick Co film, the bulk value of  $T_C$  was assumed for the calculations. Decreasing the thickness of the magnetic film to a few monolayers, a drastic decrease of the  $T_C$  is observed [8, 13]. Lower  $T_C$  can be also obtained by modifying the sample structure irreversibly, for instance by ion-irradiation [14]. However, to describe such dynamics with more relevant thermal changes of the magnetization length, a more sophisticated model would be required, involving the Landau-Lishitz-Bloch equation [15] instead of the classical LLG.

## Conclusions

Laser-induced magnetization precession in Pt/Co/Pt films was studied as a function of the Co layer thickness and the external magnetic field amplitude. A significant decrease of frequency (twice) and increase of amplitude (an order of magnitude) was observed for reducing the Co layer thickness by 0.6 nm only. To describe the measured dependencies we proposed a simplified model of laser-induced magnetization precession. We assumed that the mechanism that triggers precession in the sample is a thermal change of the magnetic anisotropy, proportional to a certain power of magnetization and following thermal changes of the magnetization on a picosecond time scale. Within the model the measured dependence of the precession frequency was reproduced with satisfactory accuracy. Using the measured dependence of the precession amplitude we were also able to determine the effective value of the exponent in the temperature dependence of the surface contribution to the anisotropy.

Keeping in mind the mentioned sensitivity of the amplitude or frequency to various parameters, the model seems to be appropriate for the fitting procedure. Using the

amplitude or frequency, depending on parameters that are known (or measured) and that are to be found, treating the other one as a reference, one can determine physical quantities that are hard to be studied locally. This would provide an opportunity to probe e.g. Curie temperature, magnetic anisotropy or thermodynamic parameters with micrometer resolution, which can be especially interesting for low-dimensional objects like patterned systems and nanostructures.

## References

- [1] W. J. M. de Jonge, P. J. H. Bloemen, and F. J. A. den Broeder, *Ultrathin Magnetic Structures* (Springer-Verlag, 1994), chap. Experimental investigations of magnetic anisotropy.
- [2] M. van Kampen, C. Jozsa, J. T. Kohlhepp, P. LeClair, L. Lagae, W. J. M. de Jonge, and B. Koopmans, *Phys. Rev. Lett.* **88**, 227201 (2002).
- [3] J.-Y. Bigot, M. Vomir, L. H. F. Andrade, and E. Beaurepaire, *Chem. Phys.* **318**, 137 (2005).
- [4] S. Mizukami, E. P. Sajitha, D. Watanabe, F. Wu, T. Miyazaki, H. Naganuma, M. Oogane, and Y. Ando, *Appl. Phys. Lett.* **96**, 152502 (2010).
- [5] R. Allenspach, M. Stampanoni, and A. Bischof, *Phys. Rev. Lett.* **65**, 3344 (1990).
- [6] M. D. Kuz'min, *Phys. Rev. Lett.* **94**, 107204 (2005).
- [7] J. Stöhr and H. C. Siegmann, *Magnetism: From Fundamentals to Nanoscale Dynamics* (Springer-Verlag, Berlin, 2006).
- [8] R. Rausch and W. Nolting, *J. Phys. Condens. Matter* **21**, 376002 (2009).
- [9] H. Callen and E. Callen, *J. Phys. Chem. Solids* **27**, 1271 (1966).
- [10] A. Morrish, *The physical principles of magnetism*, Wiley series on the science and technology of materials (Wiley, 1965).
- [11] J. Dubowik, F. Stobiecki, and T. Luciński, *Phys. Rev. B* **57**, 5955 (1998).
- [12] T. Gerrits, H. A. M. van den Berg, J. Hohlfeld, L. Bar, and T. Rasing, *Nature* **418**, 509 (2002).
- [13] P. Jensen, H. Dreyssé, and K. Bennemann, *Surf. Sci.* **269–270**, 627 (1992).
- [14] J. Ferré, T. Devolder, H. Bernas, J. P. Jamet, V. Repain, M. Bauer, N. Vernier, and C. Chappert, *J. Phys. D* **36**, 3103 (2003).
- [15] D. A. Garanin, *Phys. Rev. B* **55**, 3050 (1997).

---

## Manipulating the magnetic anisotropy by laser annealing

---

In this Chapter we present the studies of light-induced irreversible changes of the magnetic anisotropy in ultrathin metallic systems. We started our studies with the Au/Co/Au structure, bearing in mind the classical results of furnace annealing of such system [1]. The available light source was a pulse laser, however used in a semi-continuous way. Afterward, having known the interesting results obtained by our collaborators with ion-irradiation of Pt/Co/Pt systems [2, 3], we subjected this structure to annealing, using two types of laser sources: continuous wave and single femtosecond pulses. As was shown in Chapter 2, laser annealing of ultrathin magnetic structures brings a possibility of creating nanostructures by light-induced permanent decrease of magnetic anisotropy [4, 5]. Now we show a new and unique opposite possibility of increasing the anisotropy and creating perpendicularly-magnetized structures, for different ultrathin films, employing different light sources.

The presented results are described in two articles: J. Kisielewski, K. Postava, I. Sveklo, A. Nedzved, P. Trzciński, A. Maziewski, B. Szymański, M. Urbaniak and F. Stobiecki, *Magnetic Anisotropy of Co Films Annealed by Laser Pulses*, *Solid State Phenomena* **140**, 69 (2008) and J. Kisielewski, W. Dobrogowski, Z. Kurant, A. Stupakiewicz, M. Tekielak, A. Kirilyuk, A. Kimel, Th. Rasing, L. T. Baczewski, A. Wawro and A. Maziewski, *Irreversible modification of magnetic properties of Pt/Co/Pt ultrathin films by femtosecond laser pulses* (submitted).

## 5.1 Experimental details

### Samples

Three ultrathin metallic samples were studied in this Chapter: Au/Co-wedge/Au (#1), Pt/Co-plane/Pt (#2) and Pt/Co-wedge/Pt (#3):

- The sample #1 was produced using ultra-high vacuum magnetron sputtering, at the Institute of Molecular Physics of the Polish Academy of Sciences in Poznań. On a mica substrate with a 300 nm Au buffer layer, the following layers were deposited: (i) Au (1.5 nm); (ii) a Co wedge with the thickness ranging linearly from 0 to 2 nm over the 15 mm length of the sample; (iii) Au (3 nm) overlayer. Au films were (111)-textured, Co – (0001)-textured. The sputtering rates were 0.06 and 0.045 nm/s, for Au and Co, respectively. From the remanence image taken with the PMOKE microscope the spin reorientation transition (SRT) has been found to occur at the Co thickness of 0.93 nm.
- The sample #2 was produced with the MBE technique. The following films were grown on a sapphire (0001) substrate: (i) 5 nm of Pt(111) buffer layer; (ii) constant thickness of 3.3 nm Co(0001) and (iii) 5 nm of Pt(111) overlayer .
- The sample #3 was also produced with MBE, on a sapphire (0001) substrate. The following structure was deposited: (i) 5 nm of Pt(111) buffer layer; (ii) a Co(0001) wedge, with the thickness changing from 1.5 to 5 nm, with a reference step of 15 nm at the side of the sample; (iii) 5 nm of Pt(111) overlayer.

The structures of the samples are schematically depicted in Figure 5.1.

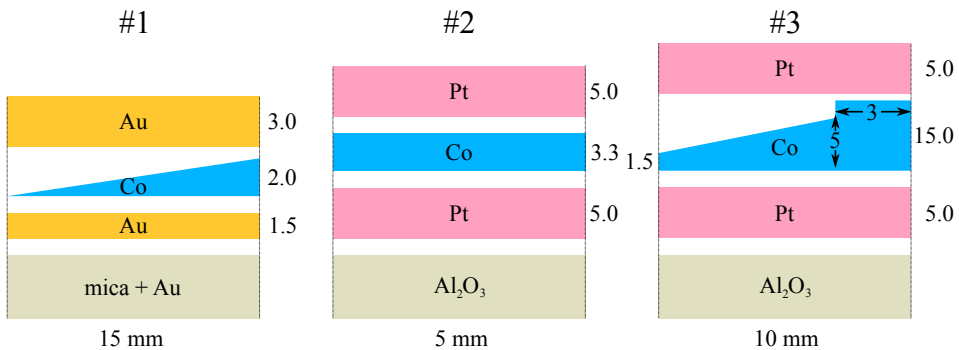


**Figure 5.1:** The structures of the samples. All vertical dimensions are given in nanometers, horizontal in millimeters.

The characterization of the static magnetic properties of the sample #3 was performed more systematically. Beside the PMOKE remanence image, using the

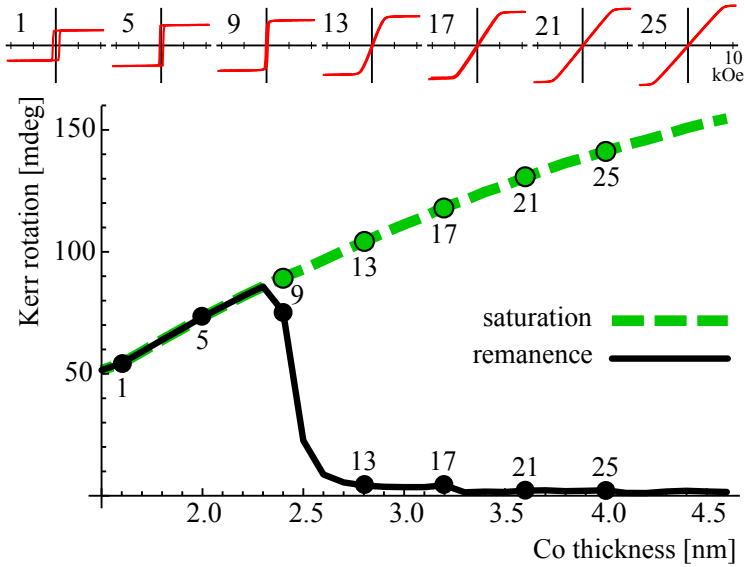


**Figure 5.2:** Top: the selected hysteresis loops recorded along the Co wedge of the sample #3, using the Kerr millimagnetometer. Main plot: the the Kerr rotation at saturation and at remanence, derived from a series of hysteresis loops. The points labeled with the numbers correspond to the values of the saturation and the remanence derived from the respective loops, shown at the top. The numbers count the original points of the scan.

PMOKE Kerr millimagnetometer a set of hysteresis loops was recorded by scanning along the Co wedge with a 0.2 mm step. From every loop the values of the Kerr rotation at saturation and at remanence were derived, as well as the coercive field and the saturation field. The saturation and the remanence as a function of the Co thickness are shown in Figure 5.2, with some examples of selected hysteresis loops, labeled with the numbers of measured points. The thickness of the SRT has been estimated to occur at  $d_0 = 2.4$  nm. Fitting to Eq. (1.17) the experimental dependence of the saturation field vs. Co thickness above the SRT (see Chapter 1.2.4), the surface anisotropy constants have been determined,  $K_s = 1.06$  mJ/m<sup>2</sup>, keeping the literature value of  $K_v = 0.41$  MJ/m<sup>3</sup> [6, 7].

### Annealing setups

Two main stages of the experiments should be distinguished. At first, the laser annealing was performed. A set of annealed spots was created irreversibly and permanently. In the subsequent part a series of magneto-optical techniques was used to characterize the magnetic properties of the laser-annealed spots.

Three samples were annealed with different types of lasers. Nevertheless, the general principles of all the three setups were similar: the laser light was focused at the sample surface with a lens. Samples, mounted on two orthogonal translation stages, were able to be moved in order to select a place to anneal. The shutter was used to open the light source for a desired exposure time. Schemes of the three setups are shown in Figure 5.3. Some details concerning each of them, as well as the respective annealing procedures, are as follows:

- **Quasi-*CW* pulse annealing.** The laser source delivered 140 fs laser pulses at a 90 MHz repetition rate, operating at the wavelength of 700 nm. A piece of glass was used to control focusing the light at the sample surface, by monitoring an optical image of the laser spot, projected on a distant screen. A computer-controlled shutter released “macro-pulses” of 0.1–30 s duration.
- ***CW* annealing.** The green light of the multi-wavelength mode of an argon laser was used. Power, regulated with internal laser settings, was calibrated before the annealing procedure, using the power meter. Shutter operated at the range of 1–30 s. The energy density was also changed by moving the sample out of the focus.
- **Single pulse annealing.** Technically the most advanced method. A Ti:sapphire oscillator with a regenerative amplifier of 1 kHz repetition rate was employed, producing laser pulses of 800 nm wavelength and a 60 fs duration. A mechanical chopper with a very thin slit let pass every hundredth pulse – this way the repetition rate was decreased to 10 Hz. To pick a single pulse, a shutter synchronized with the amplifier’s output reference signal was used, triggered manually. The laser pulses were focused at the sample surface with a lens of 10 cm focal length. The energy of the incoming pulses was monitored by a piece of glass, reflecting a few percent of the light to a sensitive power meter, working in the single-pulse energy mode. The system was initially calibrated by measuring simultaneously the energies of the pulses that were transmitted (through the lens) and reflected (from the glass) and a transmitted-to-reflected energy ratio has been determined. The energy was tuned in the range of 0–5  $\mu\text{J}$ , using neutral density optical filters.

## 5.2 Quasi-continuous pulse laser annealing of Au/Co/Au structure

Sample #1 (Au/Co-wedge/Au) was annealed with the quasi-*CW* method. The laser light of an average power of 1.5 W was focused onto a spot of about 20  $\mu\text{m}$  in diameter. A regular array of spots with exposure times ranging from 0.2 to 5 s, for varying Co



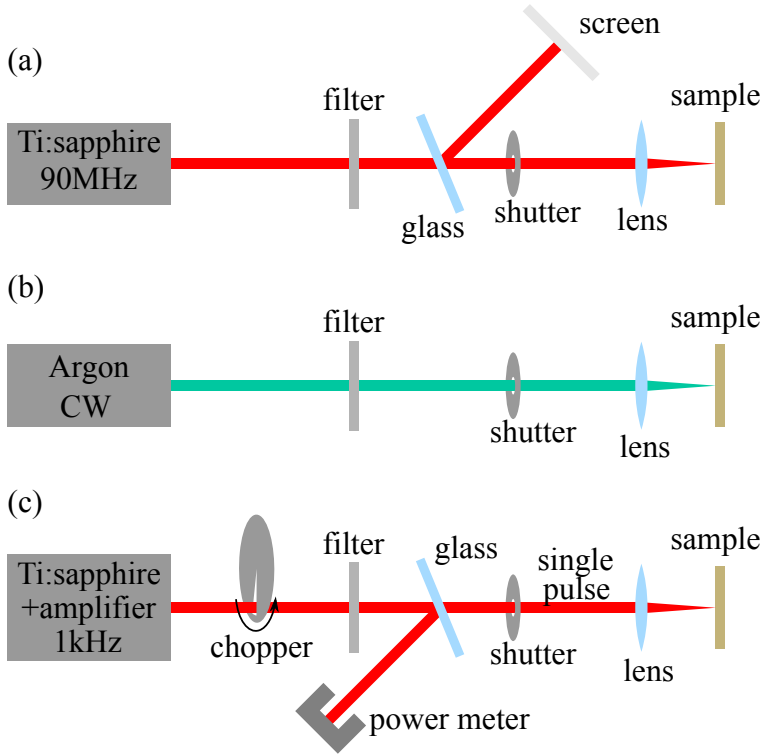


**Figure 5.3:** The schemes of the experimental setups used for the laser annealing: (a) quasi-CW pulse annealing; (b) CW annealing; (c) single pulse annealing. See the text for details.

thickness, was created. Additionally, four continuously irradiated lines were produced by a continuous motion of the sample with different speed for each line.

The annealed sample was studied with the Polar Kerr microscope with the perpendicular external magnetic field. The remanence image shows the results of the annealing procedure (Figure 5.4). The white color below the SRT thickness corresponds to the initial out-of-plane magnetization state. An appearance of the white color for Co thicknesses above the SRT is a clear evidence for the creation of a perpendicular magnetization state. More detailed observations are the following:

- Spots consist of a black dot inside and a white disk outside. Below the SRT the white disks are not visible in the white “background”;
- The size of the white disks decreases with increasing Co thickness, and increases

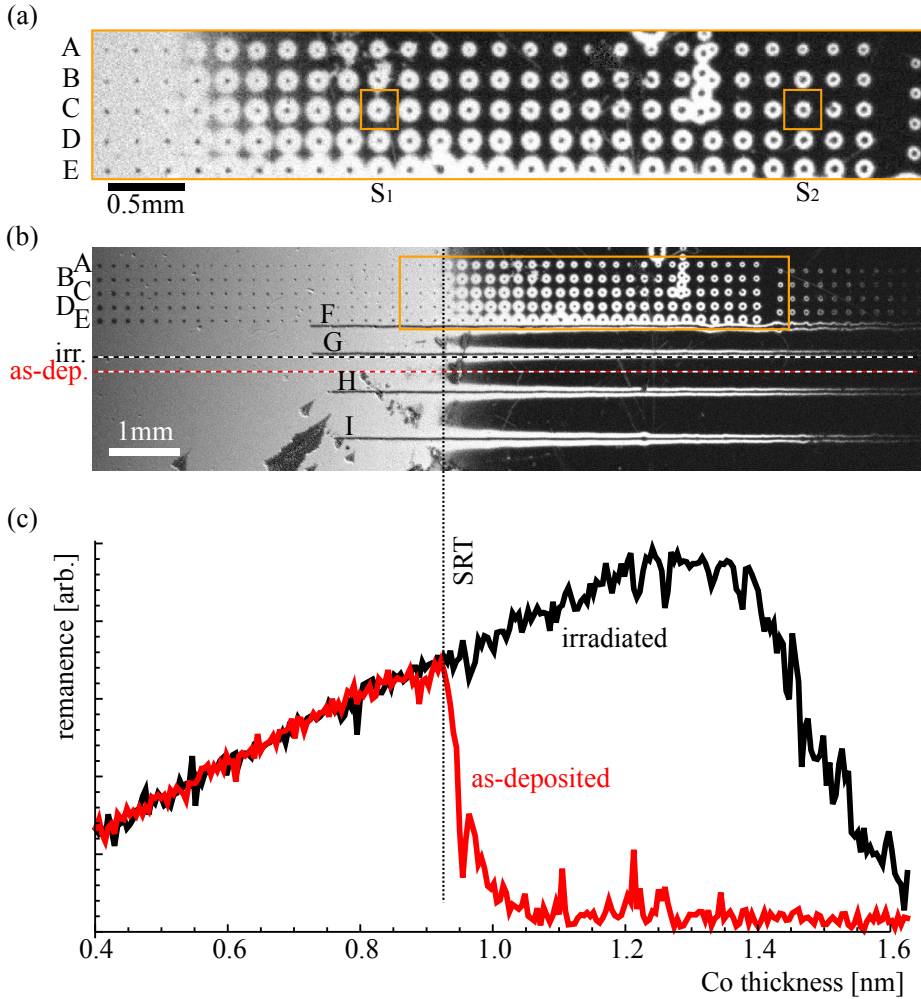


**Figure 5.4:** (a,b) The remanence image of the sample #1 after quasi-CW laser annealing. In (a) an enlarged region of the spots array is shown. The rows A–E of the array of spots were produced with different exposure times of 0.2, 0.5, 1, 2 and 5 s, respectively. The lines F–I were obtained by a continuous motion of the sample with speeds of 30, 150, 60 and 15  $\mu\text{m/s}$ , respectively. The orange frames mark two selected spots,  $S_1$  and  $S_2$  (see the text). Bottom: profiles of the remanence along the Co wedge, derived from the remanence image, for the irradiated (the line G, black) and as-deposited (red) area.

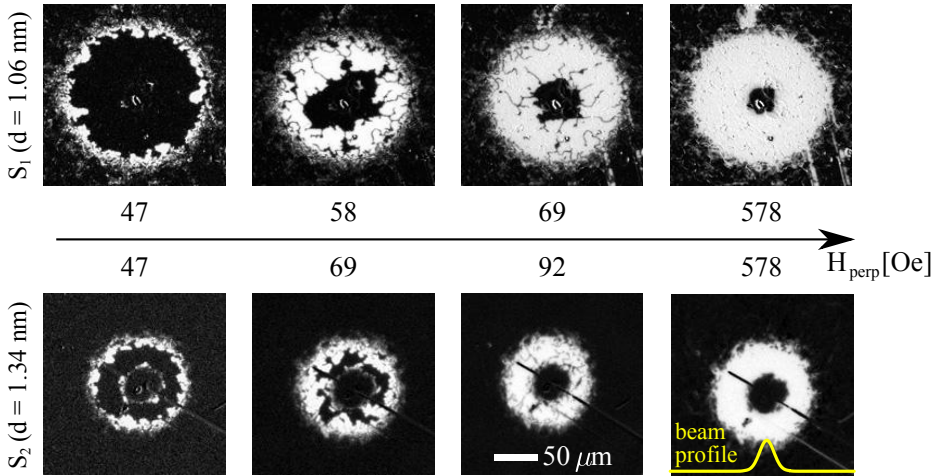


**Figure 5.5:** The sequence of differential images, taken after field pulses of indicated amplitudes, for the two selected spots,  $S_1$  and  $S_2$ . The last images at the right hand side, taken after the field pulses of maximal amplitude, are remanence images. With the yellow curve the approximate beam profile is plotted, compared with the size of spots.

with the increasing exposure time;

- The lines look like “infinitely-stretched” spots, with the black color inside and the white outside;
- Increasing the Co thickness the white color becomes brighter, however above a certain critical thickness it fades.

The last observation is more clear, plotting the gray-level profiles along the two selected lines for the irradiated and as-deposited regions, i.e. the thickness-dependence of the remanence (the bottom of Figure 5.4). A non-zero remanence of the irradiated area spreads over the higher thicknesses, hence one can conclude that as a result of the laser annealing procedure, the SRT thickness is shifted from 0.93 nm to about 1.35 nm,

A closer view at some selected spots can reveal more about the magnetic properties of the annealed area. A sequences of images, taken at zero field after the field pulses of changing amplitude, for the two selected spots  $S_1$  and  $S_2$  (marked in Figure 5.4 with the orange frames), are displayed in Figure 5.5. The following conclusions can be formulated:

- The black area shrinks from outside with increasing field amplitude – that means that the coercivity increases going toward the center;

- The magnetization reversal occurs via nucleation of a complicated magnetic domain structure;
- The very central regions remain black in all magnetic images. Their size, of about 20–30  $\mu\text{m}$  in diameter, corresponds roughly to the size of the focused beam.

In Figure 5.6 the two images – magnetic and optical, taken at a certain area of the sample ( $S_2$  is the central spot of the view), are compared. At the places corresponding to the centers of the black dots in the magnetic image, in the optical image there are some objects that look like bumps of molten material. These bumps are not symmetrical, sometimes multiple within a single spot. This suggests, that the black central areas of the spots in the remanence images correspond to non-magnetic structures, destroyed by the laser annealing.

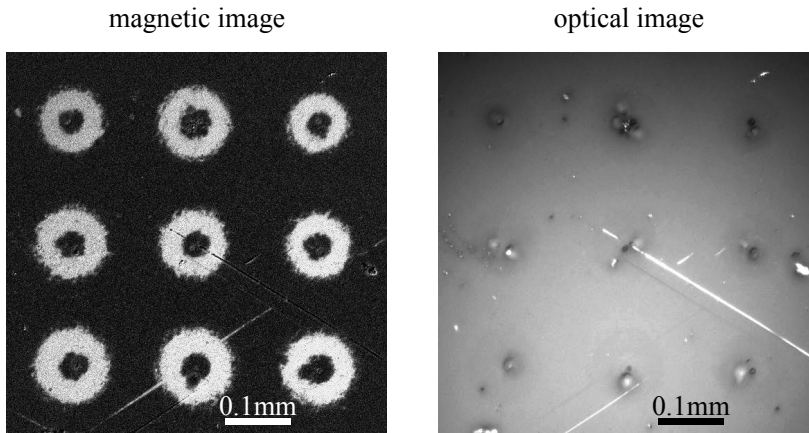


**Figure 5.6:** The magnetic (left) and the optical (right) images of a certain area of the sample (the spot  $S_2$  is visible at the center). In the central area of the spots some bumps of destroyed material appear.

## Summary

Quasi-*CW* laser annealing of the Au/Co/Au structure deposited on the mica substrate results in a creation of the out-of-plane magnetization phase for the extended range of Co thicknesses, as a form of rings around the central non-magnetic area, which corresponds roughly to the size of the focused beam. So the rings of perpendicular magnetization were not irradiated directly, but influenced by the heat transferred from the central area. In that sense it is quite intuitive, that the size of the white area is larger for longer exposure time.

### 5.3 Continuous laser annealing of Pt/Co/Pt structure

Sample #2 (Pt/Co-plane/Pt) has been subjected to *CW* laser annealing. The parameters of the experiment were the following: the incident light power varied in the range of 0.68 – 1.43 W, the exposure time of 1–30 s. Additionally, the energy density change was realized by moving the sample (position  $x$ ) out of the focus. The results have been studied with the Kerr microscope. The remanence images have been taken for the whole sample, as well as for the selected annealed spots. Figure 5.7(a) shows a part of the sample with an array of spots, annealed with the laser dosages of given values of the mentioned parameters. The beam diameter was measured for all the values of  $x$  with the knife-edge method (see Appendix B) and fitted with a single Gaussian shape. Derived values of the beam radius as a function of  $x$  are displayed in Figure 5.7(b).

Again, the most important outcome is the existence of the white color in the remanence image, corresponding to the laser-induced out-of-plane magnetization state. In Figure 5.7(c) the magnified remanence image of a single spot (the top left corner of the array) is shown, taken with a stronger microscope objective. The yellow curve indicates the beam profile, the width of which was determined with the knife-edge method. The size of the induced white spot is much larger than the beam size. Comparing those two quantities for the other spots, there is no clear correlation visible. The only observed tendency is an increasing effect with increasing amount of deposited energy, realized by changing the power or the exposure time.

The optical images (without an analyzer in the Kerr microscope system) also reveal the changes induced by laser annealing. For some spots there appear bumps, similar to the ones reported in the previous Section, of a size corresponding roughly to the central black area in the remanence images. The areas of the induced out-of-plane magnetization state are remarkably darker. It demonstrates a significantly modified structure, partially melted, which is manifested in a changed reflection coefficient.

#### Summary

*CW* annealing of the Pt/Co/Pt structure deposited on the sapphire substrate also leads to a creation of the out-of-plane magnetization phase. Like in the previous experiment, the sizes of the out-of-plane objects are much bigger than the size of the focused beam, which indicates a significant contribution of heat transfer. However, the shapes of the obtained objects are very irregular and no clear correlation between their sizes and beam diameters and powers is visible.

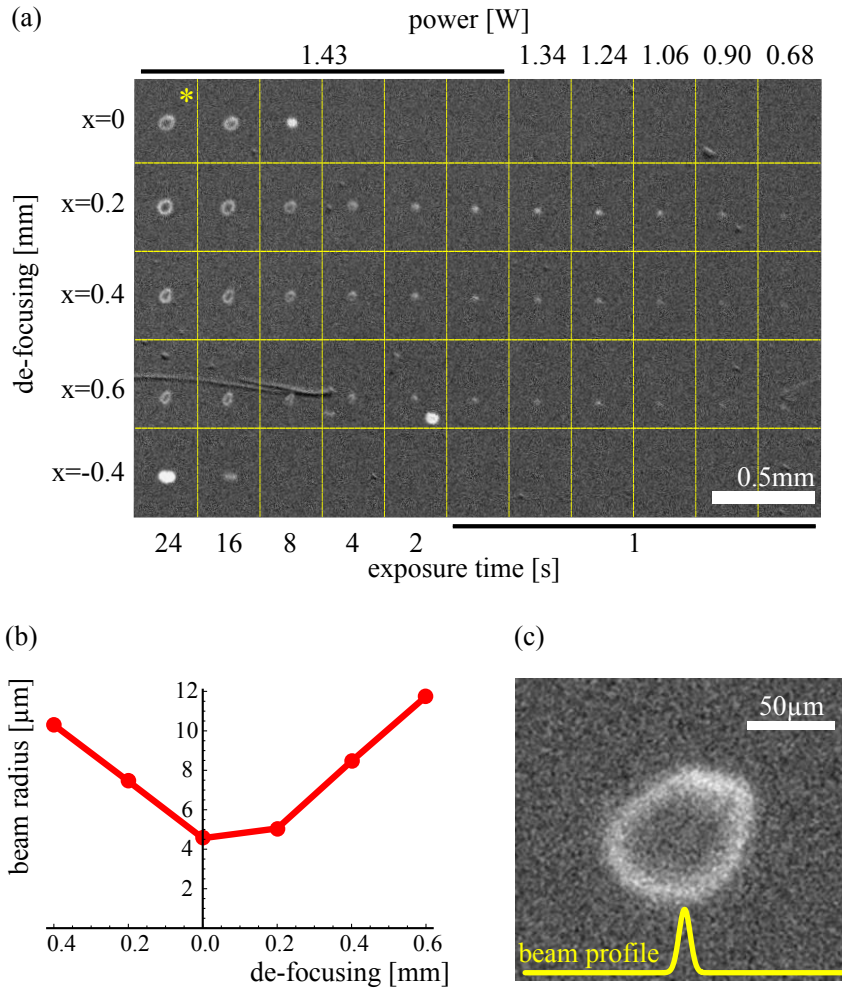


**Figure 5.7:** (a) Remanence image of the array of the spots annealed with CW laser light, for the given values of the light power and the exposure time, and focused to spots of various radii, realized by moving the sample with respect to the focus, with the given values of translation  $x$ ; (b) beam radius, determined with the knife-edge method, as a function of  $x$ ; (c) the top left spot of the array (marked in (a) with an asterisk). The yellow curve shows the beam profile for that spot, with a width determined with the knife-edge method.

## 5.4 Single pulse laser annealing of Pt/Co/Pt structure

The third sample (#3, Pt/Co-wedge/Pt) has been annealed with single laser pulses, as a function of the Co thickness (moving the sample along the Co wedge with 0.2 mm steps) and pulse energy (moving it along the direction perpendicular to the wedge and parallel to the sample plane, and changing the combination of the used optical neutral density filters).

Preliminary characterization of the pulse laser-annealed sample with the optical microscope revealed a lack of optical contrast between irradiated and non-irradiated areas. This means, in contrast to the two previous methods of annealing, that the sample was not destroyed or melted, and the eventual structural changes are rather subtle. Also the Atomic Force Microscope (AFM) measurements, performed on some selected laser-annealed spots, showed no changes in the topography of the sample within those areas – neither etched craters nor bumps of molten material were found.

### 5.4.1 Remanence images of annealed magnetic structures

The magnetic results of the pulse laser-annealed sample #3 were characterized using the polar Kerr microscope, by taking a remanence image of the whole array of annealed spots. The image is shown in Figure 5.8. The white background area at the left means an out-of-plane magnetization state, occurring for thicknesses smaller than  $d_0 = 2.4$  nm (below the SRT thickness). Clearly visible are the dots corresponding to the regions that have been annealed by the laser pulses. Every single spot is indicated with a combination of capital letter from A to F, corresponding to a series of constant pulse energy (called a “row”), and a number, corresponding to the Co thickness (called a “column”). The numbers are counted from the wedge onset and they are consistent with the ones of the initial PMOKE scan (see Figure 5.2). The rows correspond to the pulse energy values decreasing from  $4.64 \mu\text{J}$  for the row A to  $1.25 \mu\text{J}$  for F.

Beside the image of the whole array, the remanence images of every spot have been taken separately using a stronger microscope objective. A closer view at some selected spots is presented in Figure 5.9. For a better contrast a color scale (black–blue–green–yellow–white) instead of gray levels is used. The exterior of each particular image corresponds to the as-deposited structure, that was not affected by the laser pulses. The measured remanence  $\Theta_R$  was related to the saturation rotation of the as-deposited structure  $\Theta_{S0}$ , i.e. the initial out-of-plane region below the SRT thickness corresponds to the value of 1 and the light blue color.

The results of the single pulse laser-annealing, visible in the series of images in Figure 5.9, can be formulated as follows:

- The main and the most striking result is the appearance of the bright areas for Co thicknesses above  $d_0$ , which means the creation of an out-of-plane magnetization state;

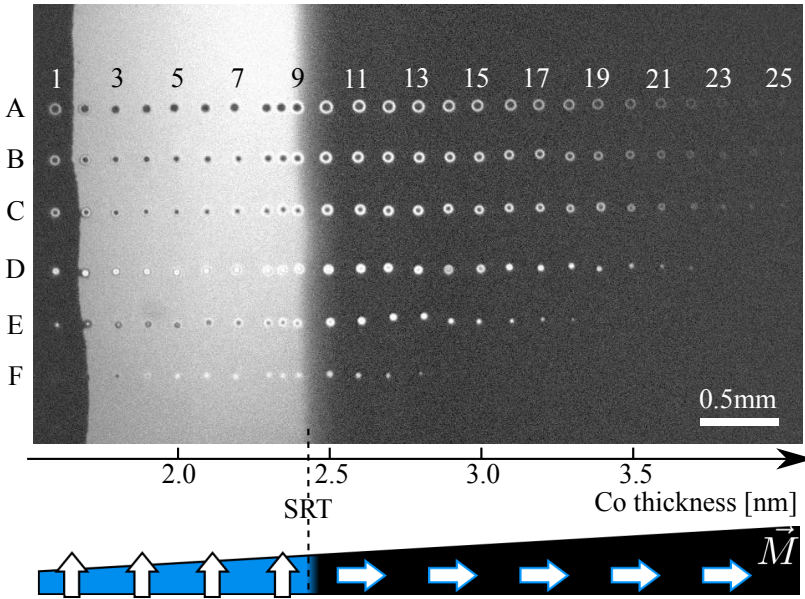


**Figure 5.8:** The remanence image of sample #3 after laser annealing. The white background area at the left corresponds to the out-of-plane magnetization state for the thicknesses below the SRT. The rows of spots marked with the letters A–F were annealed with constant pulse energies of 4.64, 3.76, 3.13, 2.51, 1.88, 1.25  $\mu\text{J}$  per pulse, respectively.

- The annealed spots appear as bright and dark disks and rings, of sizes that strongly depend on the pulse energy and the Co thickness.
- For the highest energies the spots are formed as a bright ring with a dark interior. This kind of structure is best visible for the moderate Co thicknesses.
- For the lowest thicknesses (below the SRT), rings are still visible, being brighter than the exterior, which means an increased magneto-optical signal, compared to the as-deposited structure.
- For the moderate and higher thicknesses one can distinguish even two bright rings, clearly separated by a dark one. Increasing the thickness, the rings disappear, the outer ones first.
- Decreasing the pulse energy, the ratio between the dark and bright areas changes, and the dark interiors disappear (rows D, E). The bright area is still visible up to row F.



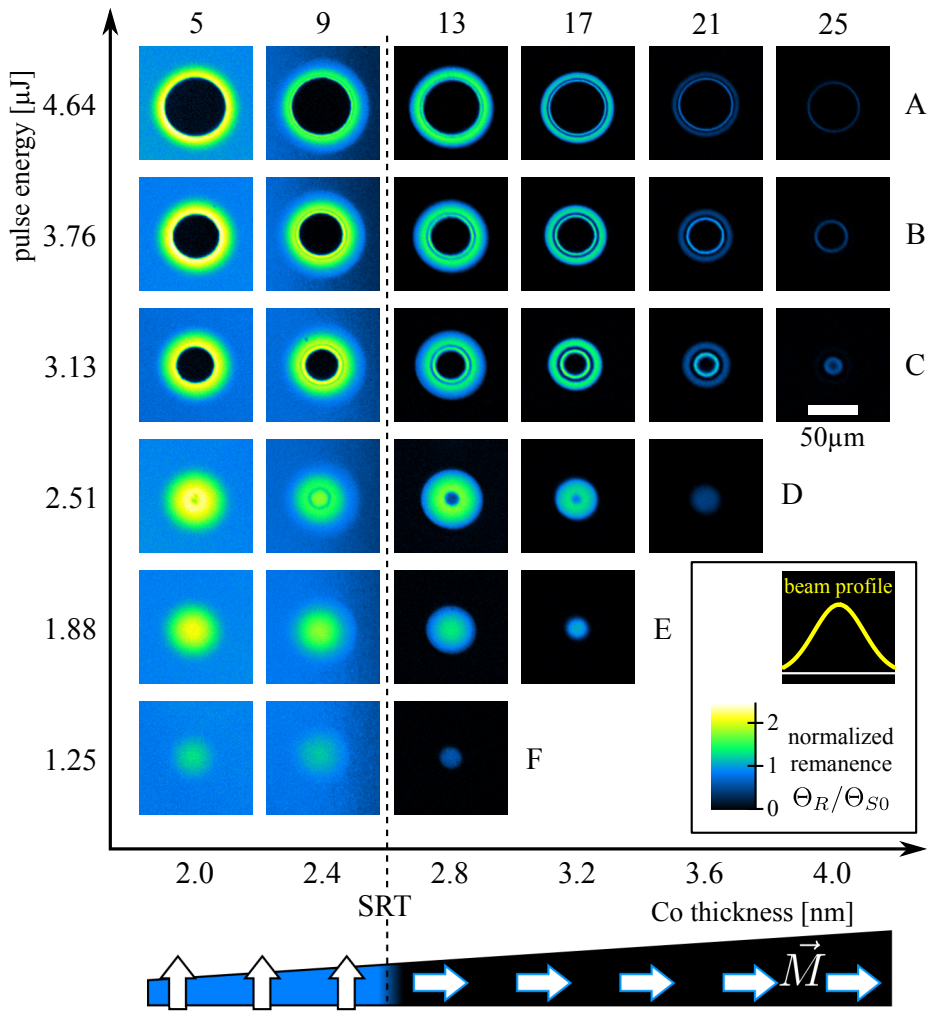


**Figure 5.9:** Detail remanence images of laser-annealed spots for the selected columns. The color scale of the remanence is plotted at the corner. The remanence scale is related to the as-deposited structure (see the text for details).

While the bright area can be easily assigned to a non-zero remanence, connected with the presence of an out-of-plane magnetization phase, about the dark interiors of some annealed spots we can only say that there is no out-of-plane component there. There are several possible explanations for the meaning of “darkness”: an in-plane magnetization state, out-of-plane magnetization state with the coercive field too high to be overcome by the available magnetic field or an absence of magnetic properties at all. To find out which explanation could be valid in our case, we need some additional information. Such information can be provided by spatially-resolved hysteresis measurements.

#### 5.4.2 PMOKE hysteresis curves

The same polar Kerr microscope setup was used in the next stage of the studies. The series of images in the presence of a perpendicular magnetic field have been taken to obtain spatially-resolved hysteresis loops of the laser-annealed spots. 17 spots have been selected for detailed studies: the ones of the rows A, C, D and E, and of the columns 5, 9, 13, 17, 21 (see Figure 5.9 except for the last column and rows B and F).

The procedure of imaging, accompanied by a special system of reference images, as well as the image processing afterwards, in order to eliminate temporal and spatial inhomogeneities of the light, sample drift and the influence of the magnetic field on the microscope objective, are described in detail in Appendix A. As a result, for each of the 17 spots a series of hysteresis curves was obtained, as a one-dimensional profile across the spots – this yielded a set of about 12 thousands loops in total.

In order to visualize the magnetization processes within laser-annealed spots, the data analysis was not confined to the mentioned profiles, it was applied to some of the whole images, selected from the sequences. Figures 5.10 and 5.11 show two examples of the sequences of the field-dependent images processed with this method, for the spots A5 and C17, respectively. The pictures were taken in the presence of the magnetic field of the values given at the axes: the upper series of pictures in decreasing field, while the lower in increasing field, which is also emphasized with the directions of the axes. The different regions of the laser-annealed spots behave differently in a magnetic field. To see those differences more clearly, some hysteresis curves were plotted for the most characteristic regions: the exterior (peripheral part, not affected by laser pulses), the interior (central part), and the ring – the most interesting region with the induced or enhanced out-of-plane magnetization state. Additionally, for spot C17 (Figure 5.11) the outer, the central and the inner rings were distinguished. Note, that the amplitudes of the loops are different for different regions, which can be also seen by eye in the pictures, as a smaller range of gray levels with changing field, e.g. for the exterior in comparison to the ring in Figure 5.10, or for the exterior and interior, in comparison to the rings, in Figure 5.11. Note also the coercive fields, that

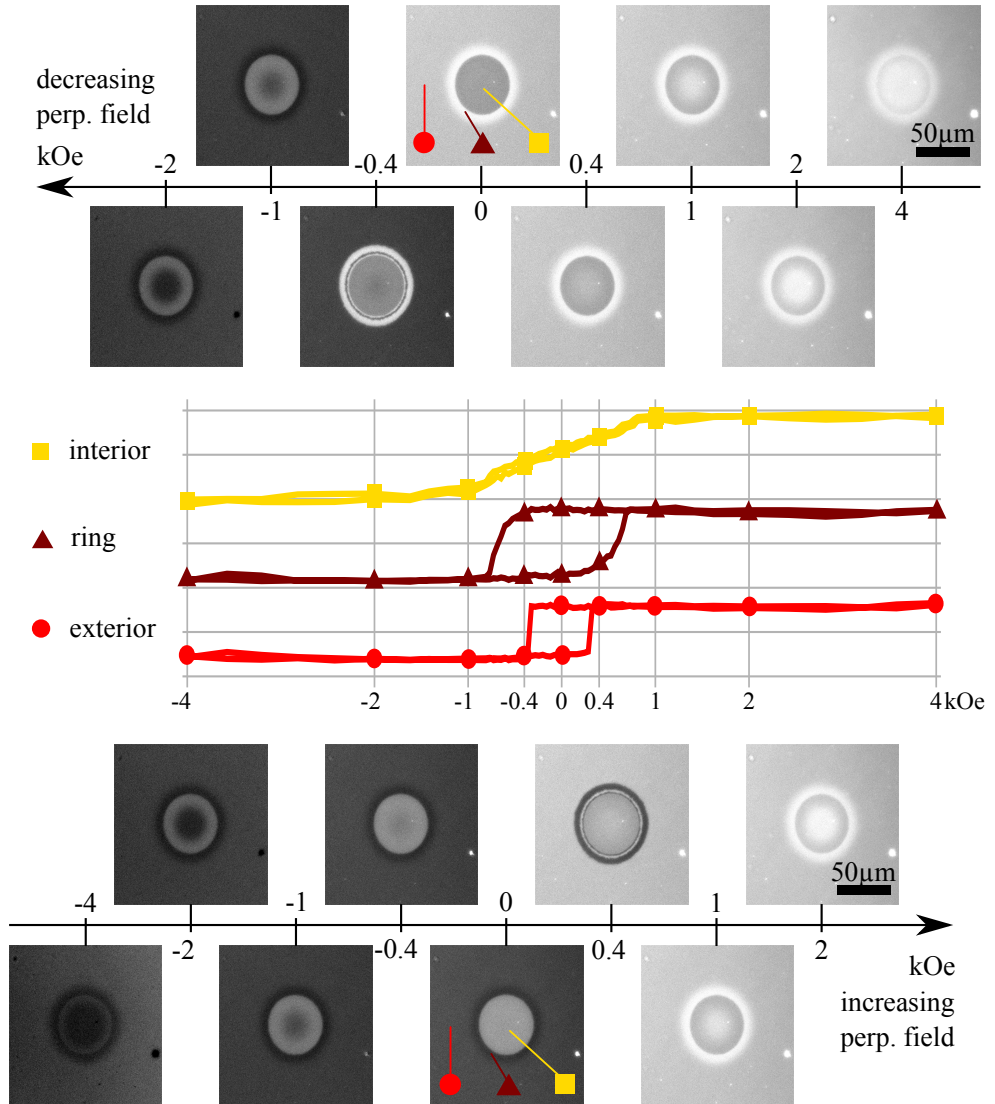


**Figure 5.10:** The top and the bottom: sequences of the images of the spot A5 ( $d_{Co} = 2.0$  nm), taken respectively in a decreasing and increasing perpendicular magnetic field of the amplitude given by the axes. Color of the gray scale is proportional to recorded Kerr rotation. Hysteresis loops for the selected regions of the laser-annealed spots (the exterior, the ring and the interior) are plotted with respective colors and markers.

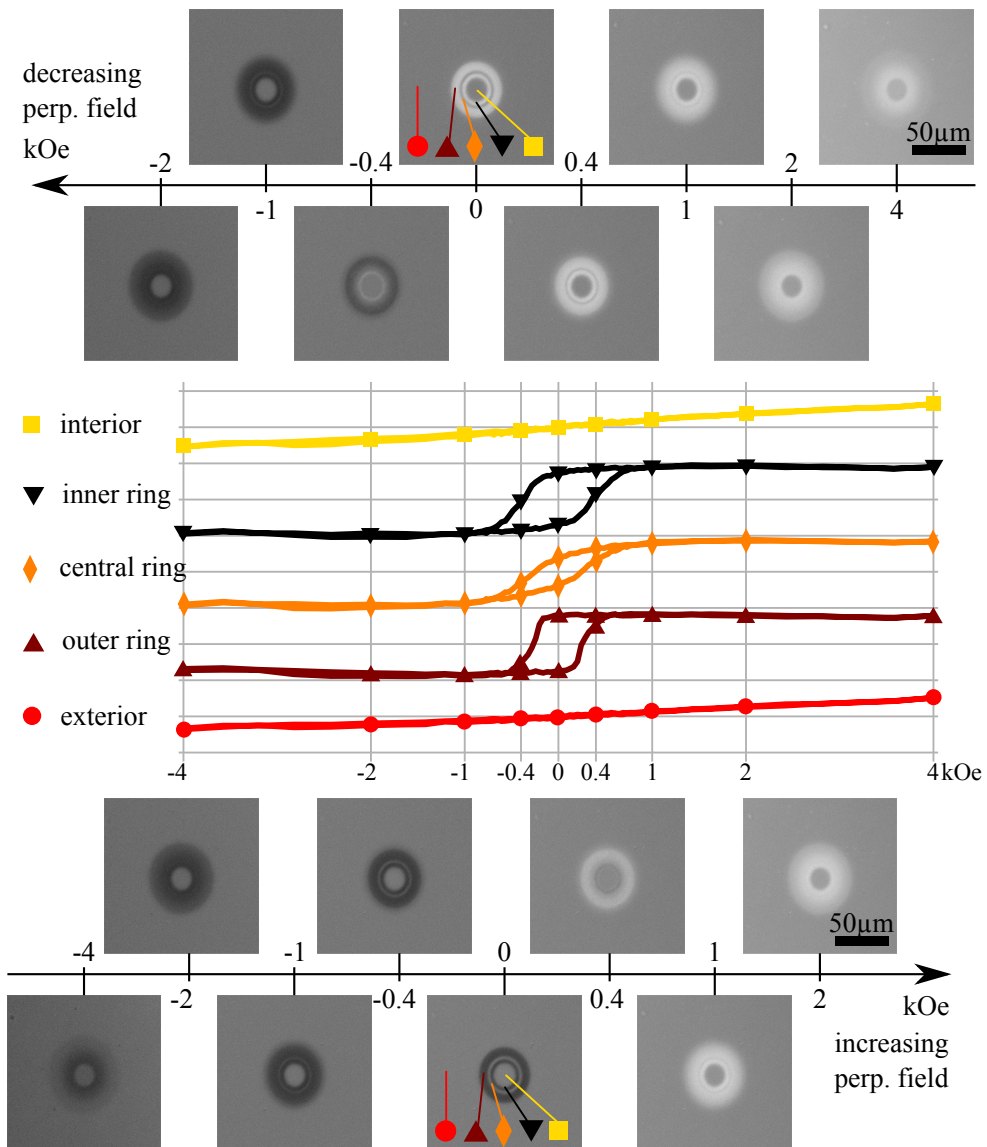


**Figure 5.11:** The top and the bottom: sequences of the images of the spot C17 ( $d_{Co} = 3.2$  nm), taken respectively in a decreasing and increasing perpendicular magnetic field of the amplitude given by the axes. Color of the gray scale is proportional to recorded Kerr rotation. Hysteresis loops for the selected regions of the laser-annealed spots (the exterior, the interior and the outer, central and inner rings) are plotted with respective colors and markers.

are different for the regions, which can be also found at pictures by the field value, at which a given region turns black or white.

The behavior of the magnetization in the outer and inner rings of the spot C17, was additionally studied, taking a series of images at zero field, after field pulses of increasing amplitude. Range of field values was chosen around the coercive field, to visualize the process of the magnetization switching. The series, shown in Figure 5.12, demonstrates this process to occur through a nucleation and propagation of the magnetic domains.

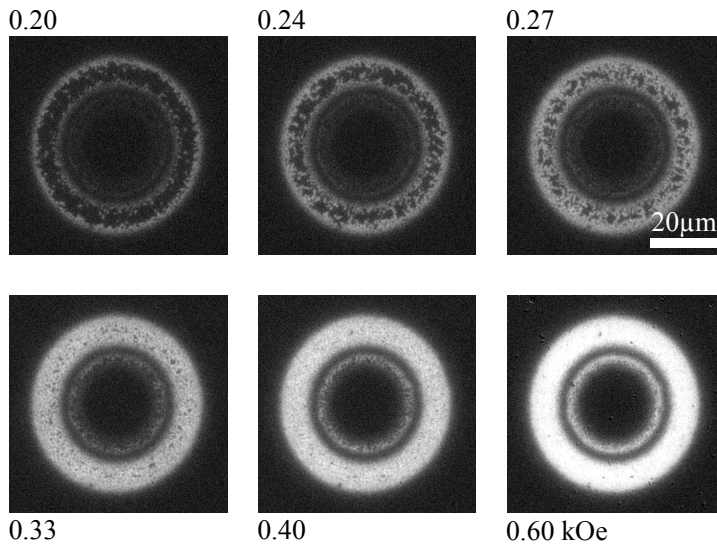


**Figure 5.12:** The series of images of the spot C17 ( $d_{Co} = 3.2$  nm) taken at zero field, after magnetic field pulses of increasing amplitude, of given values. The magnetization switching occurs via nucleation and propagation of magnetic domains.

In order to characterize the magnetization state of the material across the spots, the hysteresis loops derived from the series of images taken at field were treated afterward to derive the parameters: remanence, saturation, coercive field and saturation field. This way the profiles of those parameters were found. Examples for the spots A5 and C17 are displayed in Figure 5.13. Some of the hysteresis loops did not exhibit a saturation (available magnetic field was not high enough to saturate the system), hence there are some breaks within those profiles. Additionally, as the as-deposited sample was initially characterized with the Kerr millimagnetometer with stronger fields available, the value of the saturation field derived from those measurements is also plotted.

Observations that can be concluded from the found profiles, at first confirm the

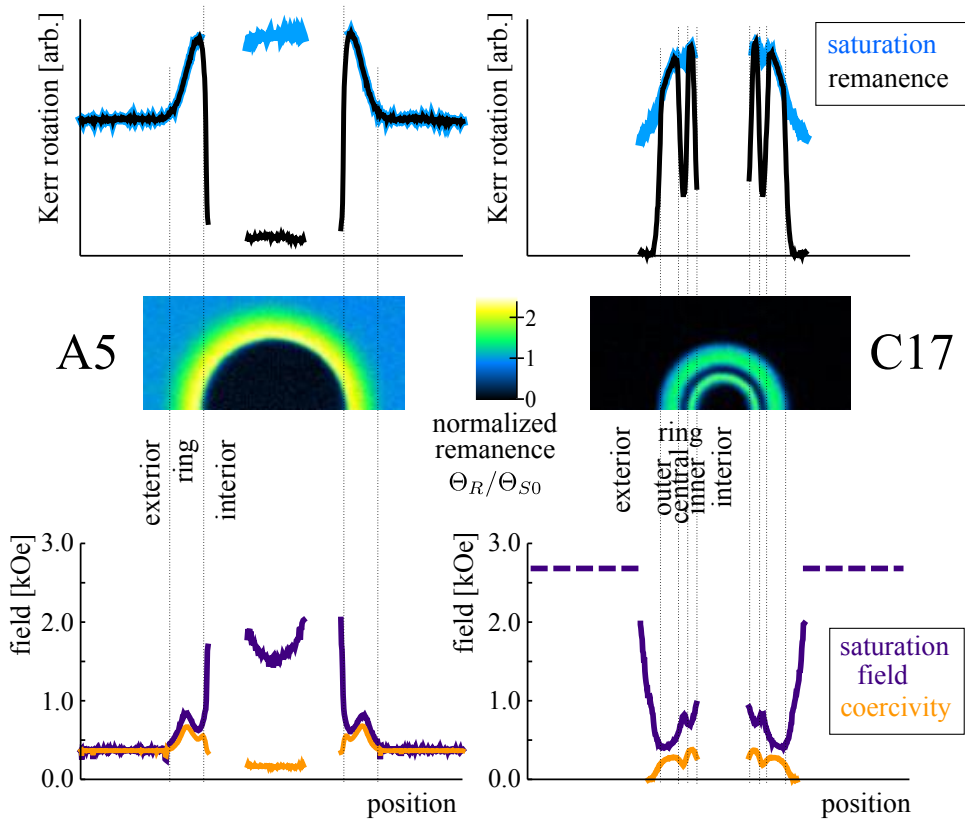


**Figure 5.13:** Examples of the derived parameters of the PMOKE hysteresis loops for the spots A5 (left) and C17 (right): the remanence and the saturation (top), and the coercive field and the saturation field (bottom). With the dashed violet line the value of the saturation field is marked, obtained from the PMOKE millimagnetometer scan for the as-deposited structure. The remanence images of the respective spots are also shown, with vertical dotted lines separating the exterior, the ring(s) and the interior regions.

conclusions of the remanence images: an out-of-plane magnetic phase is induced, with an enhanced magneto-optical signal. Also, the structure of the rings is clearly visible at those profiles. The spatially-resolved hysteresis measurements provide a more precise description of the magnetization state in the annealed spots. In particular, the central ring (in Figure 5.11), characterized as “dark” in the remanence images (Figure 5.9), has been found to have a significant out-of-plane component, quantitatively expressed as a remanence, i.e. an average cosine of the magnetization orientation angle, being approximately equal to  $1/2$ . Another remarkable outcome concerns the interior region. That area exhibits a hard direction-type hysteresis loop, indicating an in-plane magnetization state. Unfortunately, only for the spots of the lowest thickness and the higher pulse energies (A5–A9), the applied magnetic field was high enough to saturate the magnetization in the interiors.

### 5.4.3 LMOKE hysteresis curves

To check out the magnetization state inside the interiors of the laser annealed spots, the longitudinal configuration of the Kerr microscopy was also used for spatially-resolved hysteresis measurements. The magnetic field was applied in the sample plane and in the plane of light incidence, and similarly as before, imaging at the presence of the magnetic field was done, getting hysteresis loops at each single pixel. The loops were also treated with methods described in Appendix A in order to remove the influence of the magnetic field on the microscope objective. The hysteresis loops recorded for the spot C17 in the interior (averaged over the area of the interior) and the exterior (over the area of a comparable size) are shown in Figure 5.14. The shapes of the loops clearly indicate the in-plane magnetization states in both regions.

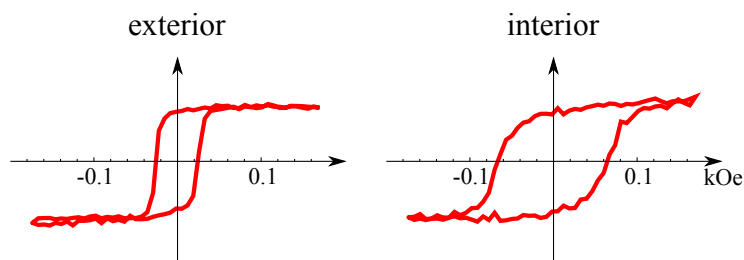


**Figure 5.14:** LMOKE hysteresis loops for the interior and exterior of the spot C17. The loops were averaged over the area of the interior, and over the area of a comparable size at the exterior.

Within an additional series of measurements, a sequence of zero-field images in the LMOKE configuration, after field pulses of the changing amplitude, was taken.

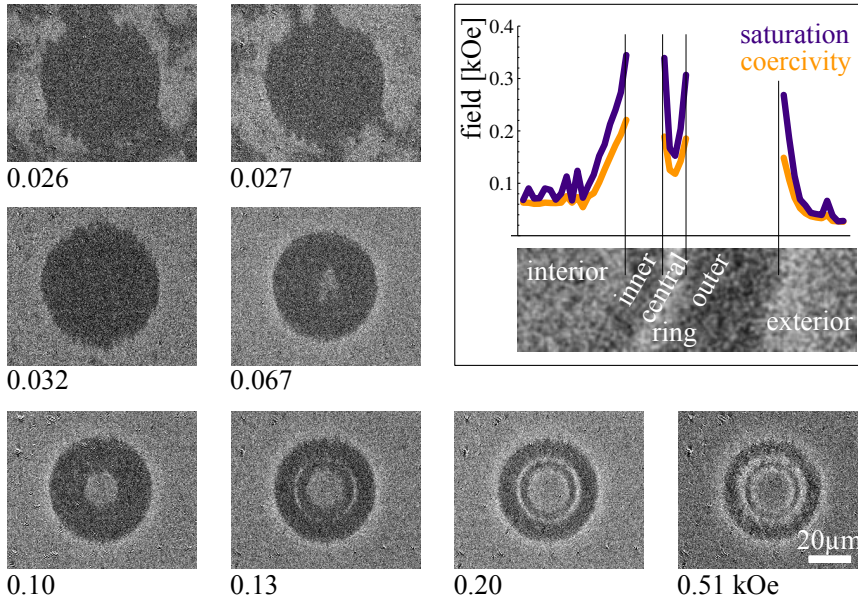


**Figure 5.15:** A sequence of LMOKE-images, taken for the spot C17 at zero field, after field pulses of the given amplitudes (the field direction is vertical with respect to the image frames). Right-top: the profiles of the coercive field and the saturation field, derived from the series of *remanence hysteresis loops*.

The selected images of the sequence are shown in Figure 5.15. Compared to the LMOKE imaging at field, such experiment yielded much better signal-to-noise ratio, what allowed us, taking the light intensity registered in the respective pixels, to create *remanence hysteresis loops* as a function of position across the spot. A remanence hysteresis, through the fact, that images are taken at zero field, is usually different from a “real” hysteresis registered at field – all values of measured signal above the value of the remanence are truncated. The shapes are identical only if the real hysteresis is square. Nevertheless, it reproduces correctly characteristic field-values. The right-top part of Figure 5.15 displays the derived coercive field and the saturation field, as functions of the distance from the spot’s center.

The results confirm first the previous observation, that the exterior and interior regions exhibit a preferred in-plane magnetization state, for their evolution of the domain structure, being switched by the in-plane magnetic field. An interesting conclusion can also be formed for the central ring, which apparently manifests also its in-plane nature, which is present beside the out-of-plane component, whose existence has been proved in the previous Section. The most probably explanation is a conical



phase (a magnetization vector making same acute angle with the sample normal), however at this stage it is impossible to exclude definitely a situation with a sub-micron structure of out-of-plane and in-plane regions.

#### 5.4.4 Energy density profiles

In the previous Section the pulse laser-induced changes of the magnetic properties have been shown. However, the diversity of pulse energies used for annealing, together with the variety of black and white (or dark and bright) structures, seems to be very complicated. In this Section we will try to systematize all results, to form some general observations and conclusions.

Looking at the circular symmetry of the spots, one can associate them with the shape of the laser beam, of a circular symmetry too. The spatial laser pulse shape, more intense at center and decreasing outside, is usually described with a two-dimensional Gaussian distribution. The local energy density, determined at a certain point of the spot, would be possible to connect with a type of induced magnetic state at that point. However, such an approach demands the assumption, that there is no planar heat transfer and all the energy that has been absorbed at a certain point, has been used for a local modification only, not affecting neighboring regions.

A simple estimation of the pulse laser-induced temperature increase and the heat transfer are carried out in Appendix C and it shows that such an assumption makes sense. Speaking roughly, the planar size of the beam is of the order of several micrometers, i.e. much larger than the thickness of the metallic layers, of nanometers. According to the calculations, energy transfer on a scale of nanometers happens on a picosecond time scale, orders of magnitude faster than on a scale of micrometers. As sapphire is a good heat conductor, the substrate is expected to be the main channel of energy dissipation.

The spatial distribution of the energy density of a laser beam can be described with the two-dimensional Gaussian shape:

$$I(x, y) = I_0 e^{-(x^2+y^2)/r_0^2}. \quad (5.1)$$

$I_0$  is the energy density at the center of the beam,  $r_0$  is the radius, defined as the distance from the center, where the energy density drops  $e$  times. Such definition of  $r_0$  has a useful property: the integral of Eq. (5.1) over space yields

$$E = I_0 \pi r_0^2 \quad (5.2)$$

and equals the total energy of a pulse, making  $I_0$  easy to be determined, having  $r_0$ .

Within the experiment the values of the pulse energies  $E$  were measured. To determine the beam radius  $r_0$ , the knife-edge method [8, 9], combined with the Liu's method [10] was applied. Details of these measurements and calculations are presented

in Appendix B. In particular it was found, that the beam in our experiment should be rather described with a linear combination of two Gaussian profiles:

$$I'(x, y) = aI_0e^{-(x^2+y^2)/r_1^2} + (1 - a)I_0e^{-(x^2+y^2)/r_2^2}, \quad (5.3)$$

with the values of parameters:  $r_1 = (33.8 \pm 0.5)\mu\text{m}$ ,  $r_2 = (217 \pm 21)\mu\text{m}$  and  $a = (98.6 \pm 0.4)\%$ . Values of  $I_0$ 's calculated for the rows A–F are listed in Table 5.1.

**Table 5.1:** Values of measured pulse energy and calculated maximal energy density ( $I_0$ ) for the rows A – F.

Row	$E$ [ $\mu\text{J}$ ]	$I_0$ [ $\text{mJ}/\text{cm}^2$ ]
A	4.64	82.3
B	3.76	66.7
C	3.13	55.6
D	2.51	44.5
E	1.88	33.4
F	1.25	22.2

### 5.4.5 Phase diagrams

Having found the parameters of Eq. (5.3), the spatial distribution of the local energy density can be finally determined. Keeping the assumption about the irrelevance of a planar heat transfer, we can determine the magnetization state induced by the laser annealing, as a function of the local energy density, which has induced that state. The magnetization state is quantitatively represented by the remanence, saturation, coercive field and saturation field, derived from the magneto-optical measurements.

To visualize the remanence as a function of the energy density, the remanence image can be superimposed on a double-Gaussian beam profile. This procedure is shown in Figure 5.16. Obviously, the center of the beam profile should be overlapped with the center of the laser-induced pattern visible in the remanence image, to get a symmetrical distribution. This way the connection between energy density (represented by an elevation) and remanence (represented by a color) can be clearly seen. Such procedure of superimposing has been performed for the series of the remanence images for the columns of constant Co thickness with varying the pulse energy (all rows A–F). Examples for two selected values of Co thickness, below and above the SRT (columns 5 and 17) are shown in Figures 5.17 and 5.18, respectively.

Beam profiles for the rows A–F have different  $I_0$ 's, but the same width, so they differ in their height only. For each row a given value of the local energy density is reached at a different distance from the spot's center, or is not reached at all, if  $I_0$  for a certain row is too low. The remanence proves to match perfectly the energy

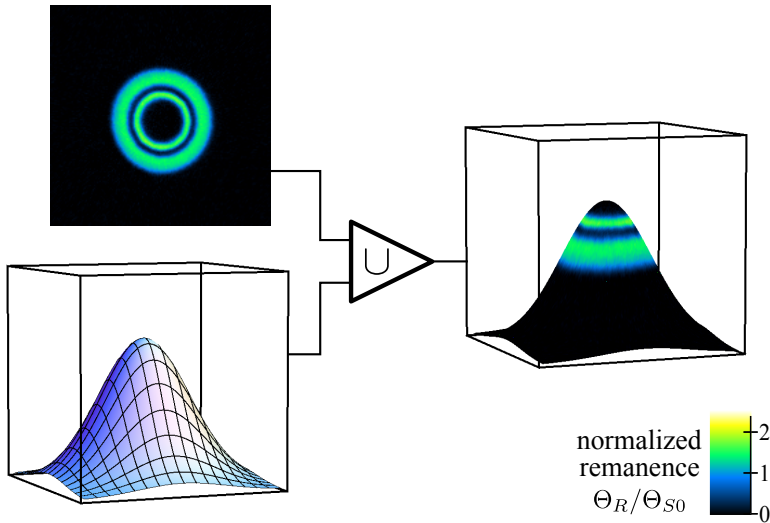


**Figure 5.16:** Superimposing a remanence image (of the spot C17 as an example) on a double-Gaussian beam profile.

density distributions for all the rows – at each plot a given color appears at the same elevation.

The effect of the pulse laser annealing depends significantly on the Co thickness. Nevertheless, presenting the thickness-dependence by a series of several three-dimensional figures would be troublesome and in fact useless. Instead, the most crucial information should be derived from such series and be presented in a concise way. A single remanence image superimposed on an energy density profile can be reduced, due to its circular symmetry, to a one-dimensional dependence of the remanence on the energy density. Such dependencies for columns 5 and 17 are shown in Figure 5.19(a,b), respectively. In Figure 5.19(c–f) the procedure of matching the respective profiles of the remanence and energy density is explained. Apparently, for a given Co thickness, the dependencies for all rows prove to be the same for the different rows A–F, following the same path, however for the different rows they are covered for different ranges of the energy density. This way the problem can be reduced to a two-dimensional dependence of the remanence on the energy density and the Co thickness, averaged over dependencies for particular rows. Such phase diagram carries the important information in a concise way. In Figure 5.20 the phase diagram for the remanence, derived from the series of all the remanence images, is shown. The different ranges of accessible energy densities for the rows A–F are plotted with the orange frames.

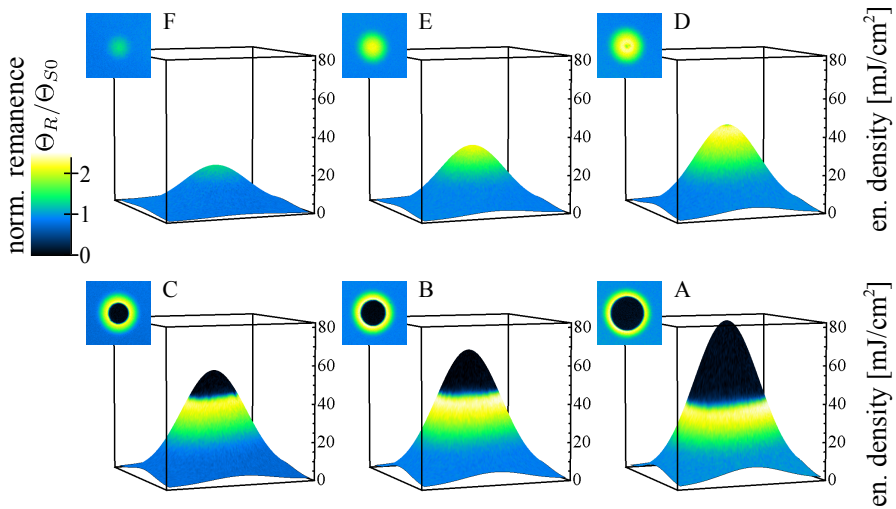


**Figure 5.17:** Superimposing the normalized remanence images on double-Gaussian beam profiles for the constant Co thickness of 2.0 nm (column 5) and different pulse energies (rows A–F).

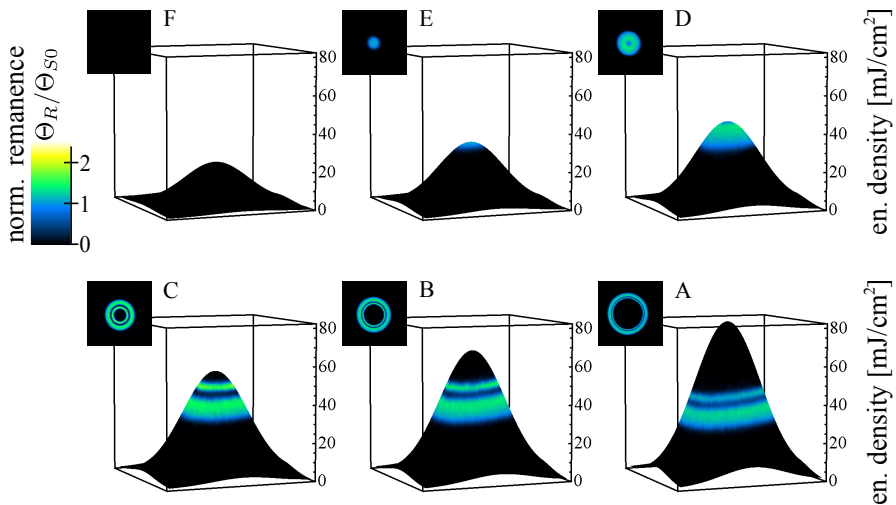


**Figure 5.18:** Superimposing the normalized remanence images on double-Gaussian beam profiles for the constant Co thickness of 3.2 nm (column 17) and different pulse energies (rows A–F).

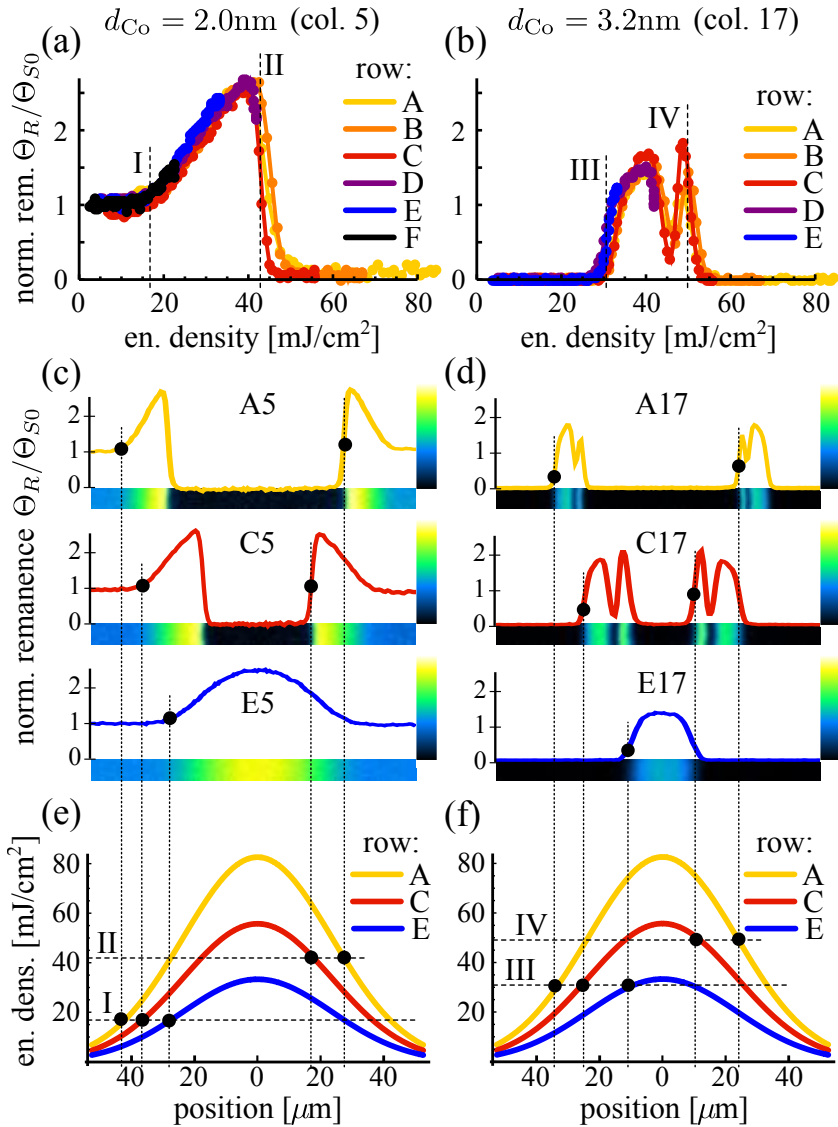


**Figure 5.19:** (a,b) The normalized remanence ( $\Theta_R/\Theta_{S0}$ ) as a function of the laser energy density, determined for the Co thickness of (a) 2.0 nm (below  $d_0$ , column 5) and (b) 3.2 nm (above  $d_0$ , column 17). The analysis was performed using the data from spots A5–F5 and A17–E17, respectively. The idea of the construction is explained in (c–f): exemplary profiles of the normalized remanence for the spots (c) A5, C5, E5 and (d) A17, C17, E17 were combined with (e,f) respective profiles of the energy density, for rows A, C and E. Some characteristic energy densities are marked with lines I–IV in (a, b, e, f).

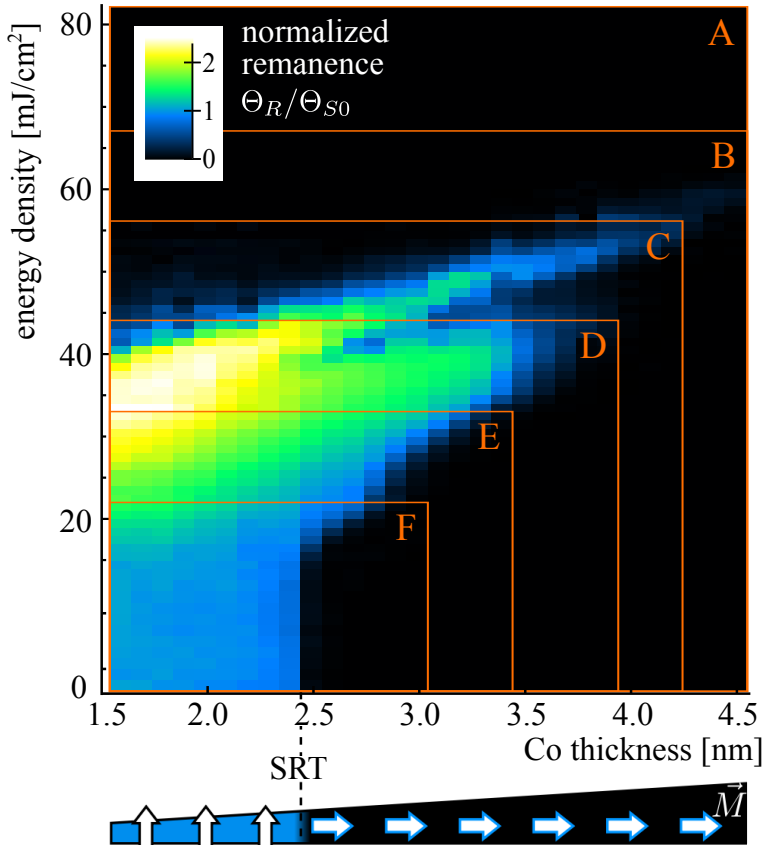


**Figure 5.20:** The phase diagram of the remanence, derived from the series of remanence images, as a function of the Co thickness and the local energy density of the annealing laser pulse. The remanence is related to the as-deposited structure (see Figure 5.9). The orange frames correspond to the ranges of energy densities that are accessible with laser pulses of the rows A–F (listed in Table 5.1). Due to the fact, that for the smaller pulse energies the range of thicknesses with visible effects of annealing is smaller, the respective frames are limited from the right.

The following conclusions can be derived from this diagram:

- Starting from the lowest energy densities (the bottom), up to about  $17 \text{ mJ/cm}^2$ , there are no changes of the magnetic properties. The SRT at the Co thickness of 2.4 nm is clearly visible as a boundary between light blue and black colors;
- For the lowest thicknesses (below the SRT, the left hand side), starting from energy densities of about  $17 \text{ mJ/cm}^2$ , the remanence increases, with a maximum at  $35\text{--}40 \text{ mJ/cm}^2$ , reaching twice the value for the not irradiated area of the same thickness;
- For the higher thicknesses (above the SRT, the right hand side), for increasing fluence the blue area is expanding and subsequently turns green – this is the outer ring, where the out-of-plane magnetization state is being created with the laser-annealing. The remanence reaches values 1.5-times larger compared to the not irradiated area;
- Increasing further the energy density the remanence decreases, reaching the dark blue central ring region. However, some out-of-plane magnetization component is still present, as the remanence does not vanish completely;
- For even higher fluences, the remanence increases again – the second branch of the diagram corresponding to the inner ring is reached. This second branch spreads over larger thicknesses (up to 4.2 nm) than the first one (up to 3.7 nm);
- For the whole range of thicknesses there exists a critical value of the fluence, where the interior turns into an in-plane phase. This transition is rather sharp and the value of this fluence changes linearly with Co thickness, which can be described as an approximate phenomenological dependence:

$$I_{\text{crit}}[\text{mJ/cm}^2] = 6 \cdot d[\text{nm}] + 32. \quad (5.4)$$

In a similar way, the phase diagrams for the parameters derived from the spatially-resolved hysteresis measurements can be composed. As those measurements have been performed for a limited number of Co thicknesses, the thickness-resolution of those diagrams is lower. Figure 5.21 presents the diagrams of the remanence and the saturation (both related to the as-deposited structure) as well as the normalized remanence (i.e. related to the local saturation values). In Figure 5.22 the analogous diagrams for the coercive field and the saturation field are shown.

The following observations can be concluded from these diagrams:

- The remanence obviously behaves similarly to that presented before (Fig. 5.20);
- The saturation confirms the increase of the magneto-optical effect due to the laser-annealing. The two branches are not present in this diagram, which means that the magneto-optical signal is still high in the central ring region;

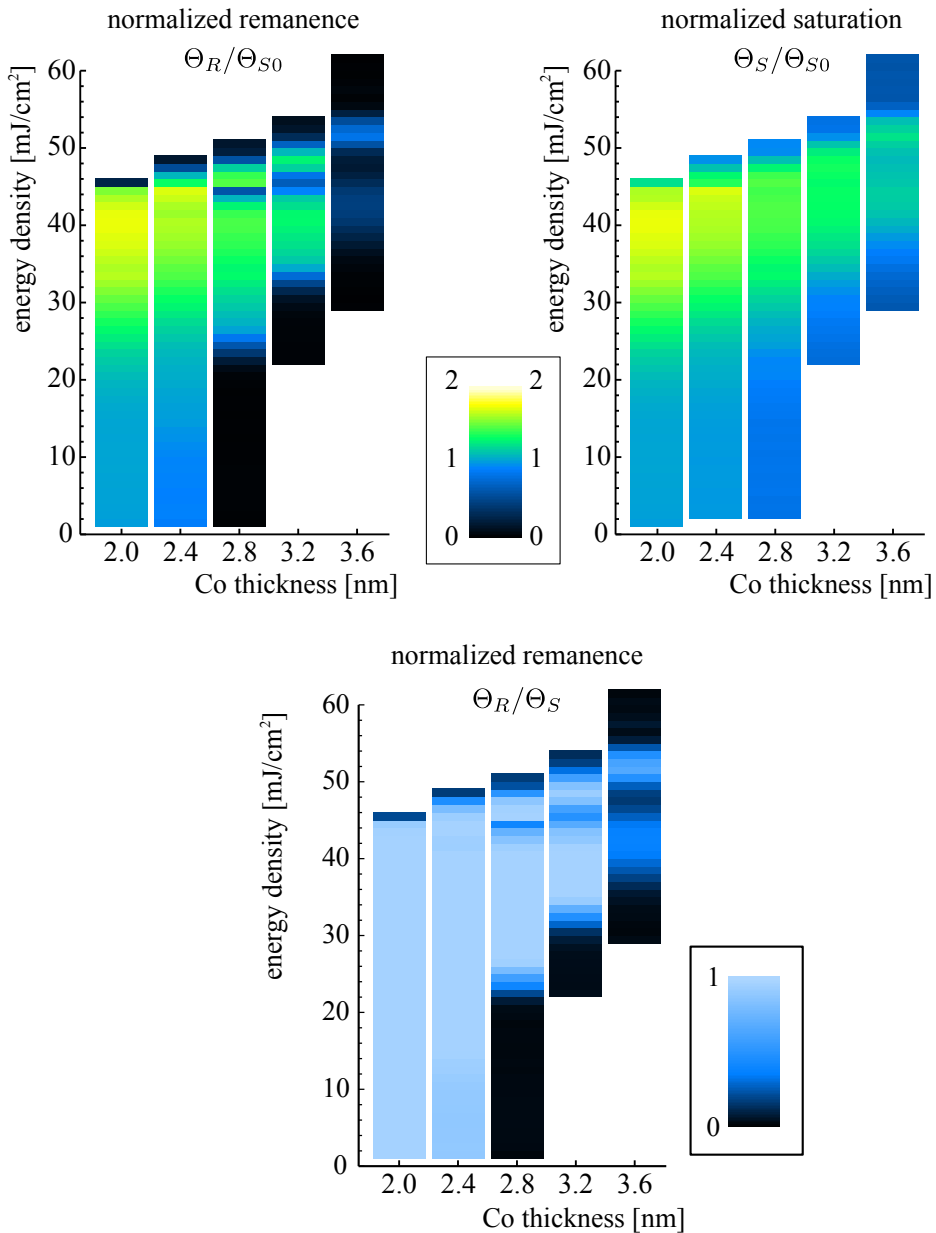


**Figure 5.21:** The phase diagrams of the remanence and the saturation (both related to the as-deposited structure (see Figure 5.9), and the normalized remanence (related to the local saturation values), derived from the spatially-resolved hysteresis measurements, as a function of the Co thickness and the local energy density.



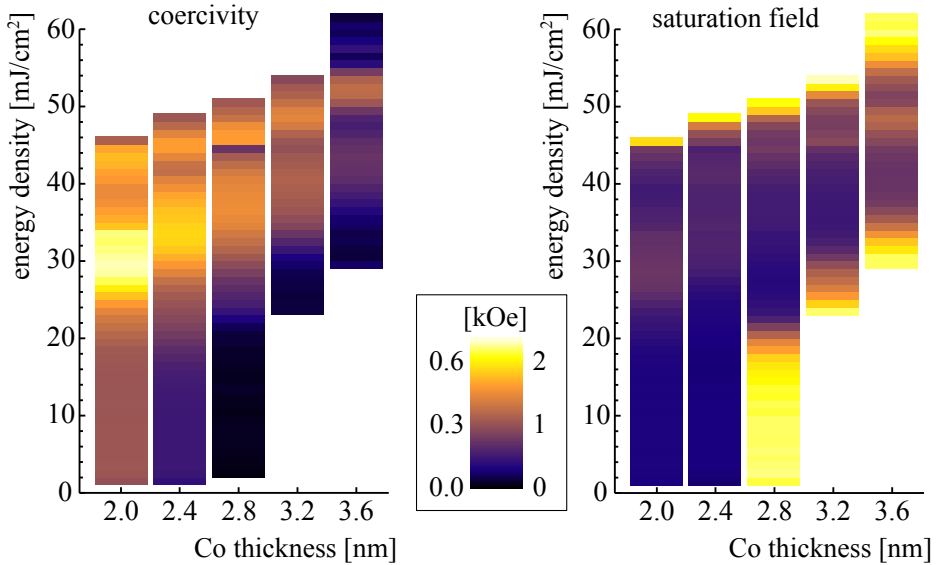


**Figure 5.22:** The phase diagrams of the coercive field and the saturation field, derived from the spatially-resolved hysteresis measurements, as a function of the Co thickness and the local energy density. Note the different color scale for each diagram.

- The normalized remanence (related to the local saturation value), indicates the squareness of the hysteresis loop and the out-of-plane magnetization component. The loops are square and there are pure out-of-plane phases below the SRT for the whole range of energy densities up to  $I_{\text{crit}}$ , as well as in two branches above the SRT, up to the Co thickness of 3.2 nm;
- The coercive field: two branches are visible. The highest values, up to 0.8 kOe, occur for the smallest Co thickness and fluences of about 30 mJ/cm<sup>2</sup>;
- The saturation field: the structure of the diagram is similar to the one for the coercive field. Unfortunately the available field was not sufficiently high to study the behavior within all in-plane regions.

### 5.4.6 Summary

The pulse laser annealing of the Pt/Co/Pt structure deposited on the sapphire substrate yields the creation of the out-of-plane magnetization phase, with remarkably increased magneto-optical signal and increased coercive field. In contrast to the two experiments mentioned above, the use of laser pulses of 60 fs duration allowed to

get very clear patterns, not blurred by planar heat diffusion, with a structure directly related to the spatial distribution of the energy density of the laser pulses. The studies of the remanence images, as well as spatially-resolved hysteresis curves, carried out systematically with various pulse energies and Co thicknesses, revealed a complex phase diagrams, containing out-of-plane and in-plane regions and numerous reorientation transitions in between.

## 5.5 Discussion

In Sections 5.2–5.4 three different methods of laser annealing were presented, performed with different samples. The possibility of the creation of permanent and irreversible microstructures with an out-of-plane magnetization state above the SRT thickness is the common outcome for all of them, however there are also some significant differences.

### **CW heating vs. pulse heating**

The question to be discussed first, is: what is the heating process due to the absorption of the laser energy in the sample? Generally it depends on the way the energy is deposited. In the *CW* laser annealing the energy is pumped continuously, so accumulation of the heat becomes important, and processes like the planar heat transfer and heat conductance to the ambient air play a crucial role. Considering the studied powers, beam sizes and total exposure times in both the *CW* and quasi-*CW* cases, the huge energy densities of  $\text{MJ}/\text{cm}^2$  are reached, however deposited very slowly. The energy density per ultrashort pulse within the quasi-*CW* annealing is only a few  $\text{mJ}/\text{cm}^2$ , but due to a high repetition rate, the sample does not have time to cool down completely after each coming pulse.

In the single pulse laser annealing, the energy is transferred very rapidly, and the temperature dynamics should be treated with the two-temperature model (2TM): the electrons absorb the energy of a laser pulse and heat up to a very high temperatures; next, on the time scale of a few picoseconds, they thermalize with the lattice (see Chapter 1.1.2). As a first approximation, the presented in Appendix C one-temperature model (1TM), which involves an immediate heating up and subsequent thermalizing between the metallic layers, can be checked. From a rough estimation of the temperature increase after a few picoseconds (after the thermalization of the electron and lattice baths, when both the 1TM and 2TM should work consistently), one obtains rather absurd result: an energy density of about  $50 \text{ mJ}/\text{cm}^2$  would be high enough to evaporate the metallic layers of sample #3. Indirectly we know, that in reality the structure is not destroyed with such intense pulses, as some magnetic properties can still be studied.

### Role of substrate

This confusing result can be explained with the role of substrate, which was not taken into account in the calculations above. Sapphire, which is a good heat-conductor, can absorb a part of the energy from the metallic lattice during the first picoseconds, while the latter is heating up by the electrons. This way, the maximum temperature that is reached by the lattice is remarkably lower and the metallic structure can survive.

The heat conductivity of the substrate is a crucial parameter also in the case of the (quasi)-*CW* annealing. It determines the balance between the energies which is pumped and moved out. The mica and sapphire substrates used in our samples exhibit different heat conductivities: for mica it is about 4 and  $0.45 \text{ Wm}^{-1}\text{K}^{-1}$  (parallel and perpendicular to platelets, respectively) [11], for sapphire about  $30 \text{ Wm}^{-1}\text{K}^{-1}$  [12]. This diversity is supposed to be the main reason for the difference of magnetic and structural results observed for the samples #1 (mica) and #2 (sapphire). The metallic films on mica with a poor heat conductivity, are heated more efficiently, which results in an exposure-dependent size of the laser-induced white spots on the sample #1. On the other hand, sapphire transfers the heat more efficiently out of the spot and thus the effects of annealing are much weaker and less-visible.

### Co/Au vs. Co/Pt interface anisotropy

Regardless all the aspects of the temperature dynamics, that may induce some structural changes, finding the link between the induced magnetization states and the structural changes themselves, is a separate challenge. On the basis of available literature, some speculations can be made – laser annealing can be compared to the classical furnace annealing. In the case of Co/Au structures, it has been found to result in sharpening the interface, improving the quality of the sample, which leads to an increase of the magnetic anisotropy, i.e. an increase of the SRT thickness and the creation of the out-of-plane magnetization state [1, 13]. This agrees well with our observations, and can be considered as a reasonable mechanism occurring in the sample #1 upon laser irradiation.

About the two other samples the situation is more complicated. Co and Pt are known to intermix at elevated temperature [14, 15], which is expected to bring a decrease of magnetic anisotropy [16]. Indeed, as a result of nanosecond laser pulse annealing of Co/Pt multilayer structures, the magnetic anisotropy was found to decrease and an in-plane magnetization state was found to appear, where initially the out-of-plane state was present [4, 5]. Although this effect also occurs in our case for the highest energy densities (the very top part of the phase diagram – Figure 5.20), it does not explain the opposite effect of the creation of an out-of-plane phase (for the Co thicknesses, where initially the in-plane state was present). We recall some results of the classic annealing again. Lin et al. [17, 18] studied *in-situ* the magnetic properties of a few-nanometer Co on Pt substrate, as a function of annealing temperature. For

a temperature range of 500–700 K they found an increase of both magneto-optical response (twice) and magnetic anisotropy (creation of an out-of-plane phase). The effects were explained in terms of Co-Pt alloy creation. Increasing the temperature further (above 800 K), the Kerr effect and magnetic anisotropy decreased – in a narrow range of annealing temperatures the sample appeared to prefer the in-plane magnetization state, and next the magnetic properties disappeared, what was explained by dissolving of Co atoms in the Pt substrate. In some sense our results are very similar – the out-of-plane magnetization phase is created, followed by the in-plane state, while increasing the local light energy density. However there are also significant differences. There is limited amount of Pt in our case, so Co cannot dissolve completely and the system stays still magnetic for high light energies. Second, laser annealing takes drastically shorter time, probably much higher temperatures are reached. Intermixing is obviously also expected, but it occurs much more rapidly, and such non-equilibrium processes may have a crucial impact on the appearing structures, resulting in creation of disordered alloys and non-homogeneous phases.

Magnetic properties of Co-Pt alloys, originating from hybridization of electronic orbitals and inducing large magnetic moments on Pt, are very sensitive to the changes of Co and Pt concentration [19–21], crystallographic structure [22], as well as a degree of order [23]. The anisotropy of Co may vary in a very broad range, dependent on a neighborhood: from 0.05 meV/atom for hcp Co, through 0.8 for ordered tetragonal  $L1_0$  CoPt, to 2.0 for a one-dimensional chain of Co atoms and 9.3 for a single Co atom on a Pt(111) film [24]. Taking this all into account, after laser annealing we can expect at the interfaces a mixture of Co-Pt alloy phases of various concentrations, degrees of order and homogeneities. They exhibit different magnetic properties and interact with each other, contributing to the total effect, which we observe in our experiments. Particularly, some specific combinations of alloy phases could be responsible for the observed two branches of the out-of-plane magnetization state.

Another hint is given by Maziewski et al. [3], who studied the influence of ion-bombardment on Pt/Co/Pt structures. As a result, the authors also found an increase of the magnetic anisotropy and a creation of the out-of-plane magnetization phases. Moreover, a two-dimensional phase diagram of the remanence as a function of Co thickness and ion fluence has a similar form to ours, with the two branches of perpendicular magnetization present (see Figure 2.4). The given explanation concerns the creation of the two ordered Co-Pt alloys, which exhibit a large perpendicular anisotropy [17–20]: the CoPt and CoPt<sub>3</sub> alloys would be responsible then for the first and second branch, respectively. Sakamaki et al. [25] suggest ion irradiation-induced stresses as a mechanism of the magnetic anisotropy changes in Pt/Co/Pt systems, however they studied the appearance and disappearance of the first out-of-plane branch only.

Although the microscopic mechanisms of laser annealing and ion-irradiation are remarkably different, in both cases there is some deposition of energy, and some

intermixing occurs. In that sense the given explanations of Co-Pt alloys creation and/or stresses can be adopted as a possible mechanisms of the structural changes happening upon the pulse laser irradiation. To decide, which scenario is realized in our case and what alloy phases are responsible for the induced out-of-plane magnetization states, some microscopic data is required. Unfortunately the fact, that the light-induced changes happen at buried interfaces, and moreover within a planarly-limited area, eliminates the techniques typically used for an *in-situ* characterization of the surface structure, like scanning tunneling microscopy, reflection high-energy electron diffraction, low-energy electron diffraction or Auger electron spectroscopy.

### Enhanced Kerr response

Some attention should be also paid to the increased magneto-optical response and its correlation with the magnetic anisotropy. The observed enhanced Kerr rotation should not be interpreted as an increase of the magnetization (as it was presented in Chapter 3.2). This works only in a situation, when the structure of a material does not change, which is evidently not the case. A change of the electronic structure, particularly of the spin-orbit coupling, results in a change of the magneto-optical constants. However, a modification of the magnetization itself may also occur. Magnetic moments on Co atoms in certain Co-Pt alloys are being reported to increase, also the induced moments on Pt atoms are observed [21]. Nevertheless the magnetization, expressed as the total magnetic moment per unit volume of an alloy, is usually lower for alloys compared to pure Co.

For the common origin in the spin-orbit coupling, the magnetic anisotropy and the magneto-optical signal are closely connected to each other [20]. The correlation is visible in Figure 5.21, in a similarity of the diagrams for the remanence (which represents a preferred magnetization state and thus the anisotropy) and for the maximal Kerr rotation. So both quantities are correlated indeed for most of the ranges of available Co thicknesses and energy densities. The exception is the area between the branches (or between the inner and outer rings), where the magnetic anisotropy slightly decreases compared to the branches, while the Kerr rotation does not. For a more quantitative comparison, some more systematical measurements should be performed, like spatially-resolved hysteresis with a broader range of magnetic fields (which was unavailable in the current setups), to observe a full dependence of the anisotropy field and maximal Kerr rotation on the Co thickness.

### Conclusions

To conclude, laser-induced modification of the magnetic anisotropy and magneto-optical response in ultrathin Au/Co/Au and Pt/Co/Pt samples has been reported. For both systems the out-of-plane magnetization phase was found to be created permanently, for Co thicknesses far above the SRT thickness, however the mechanisms of

the structural changes in both cases are supposed to be different. Due to the deposited energy and locally increased temperature, the immiscible Co and Au atoms diffuse “back” at interfaces of initial poor quality, making them more sharp and causing an increase of the magnetic anisotropy; oppositely, Co/Pt interfaces degrade, which lowers the anisotropy for the highest pulse laser energy densities. Nevertheless, for medium energies the Co-Pt alloys can possibly form, contributing to the increased perpendicular magnetic anisotropy, as well as the enhanced magneto-optical signal and coercive field.

Comparing (quasi)-*CW* annealing and single pulse laser annealing, the latter method only seems to be practical. As the obtained objects were regular, of predictable shapes not blurred by the heat transfer, this opens an unusual opportunity to produce nanostructures in a desired way. Using relatively simple methods, like interference lithography, one could produce easily regular arrays of perpendicularly or planarly magnetized nanostructures, choosing a proper energy density distribution. On the other hand, new interesting experimental and theoretical tasks are appearing, concerning details of the light-induced structural changes and the mechanisms of anisotropy alteration.

## References

- [1] F. J. A. den Broeder, D. Kuiper, A. P. van de Mosselaer, and W. Hoving, *Phys. Rev. Lett.* **60**, 2769 (1988).
- [2] J. Jaworowicz, A. Maziewski, P. Mazalski, M. Kisielewski, I. Sveklo, M. Tekielak, V. Zablotskii, J. Ferré, N. Vernier, A. Mougin, et al., *Appl. Phys. Lett.* **95**, 022502 (2009).
- [3] A. Maziewski, P. Mazalski, Z. Kurant, M. O. Liedke, J. McCord, J. Fassbender, J. Ferré, A. Mougin, A. Wawro, L. T. Baczewski, et al., *Phys. Rev. B* **85**, 054427 (2012).
- [4] A. Aktag, S. Michalski, L. Yue, R. D. Kirby, and S.-H. Liou, *J. Appl. Phys.* **99**, 093901 (2006).
- [5] C. Schuppler, A. Habenicht, I. L. Guhr, M. Maret, P. Leiderer, J. Boneberg, and M. Albrecht, *Appl. Phys. Lett.* **88**, 012506 (2006).
- [6] W. J. M. de Jonge, P. J. H. Bloemen, and F. J. A. den Broeder, *Ultrathin Magnetic Structures* (Springer-Verlag, 1994), chap. Experimental investigations of magnetic anisotropy.
- [7] R. Allenspach, M. Stampanoni, and A. Bischof, *Phys. Rev. Lett.* **65**, 3344 (1990).

- 
- [8] J. M. Khosroffian and B. A. Garetz, *Appl. Opt.* **22**, 3406 (1983).
- [9] M. A. C. de Araújo, R. Silva, E. de Lima, D. P. Pereira, and P. C. de Oliveira, *Appl. Opt.* **48**, 393 (2009).
- [10] J. M. Liu, *Opt. Lett.* **7**, 196 (1982).
- [11] A. S. Gray and C. Uher, *Journal of Materials Science* **12**, 959 (1977).
- [12] D. G. Cahill, S.-M. Lee, and T. I. Selinder, *J. Appl. Phys.* **83**, 5783 (1998).
- [13] M. Speckmann, H. P. Oepen, and H. Ibach, *Phys. Rev. Lett.* **75**, 2035 (1995).
- [14] R. Oriani and W. Murphy, *Acta Metall.* **10**, 879 (1962).
- [15] M. Galeotti, A. Atrei, U. Bardi, B. Cortigiani, G. Rovida, and M. Torrini, *Surf. Sci.* **297**, 202 (1993).
- [16] H. J. G. Draaisma, F. J. A. den Broeder, and W. J. M. de Jonge, *J. Appl. Phys.* **63**, 3479 (1988).
- [17] M.-T. Lin, C. C. Kuo, H. Y. Her, Y. E. Wu, J. S. Tsay, and C. S. Shern, *J. Vac. Sci. Technol. A* **17**, 3045 (1999).
- [18] M.-T. Lin, H. Her, Y. Wu, C. Shern, J. Ho, C. Kuo, and H. Huang, *J. Magn. Magn. Mat.* **209**, 211 (2000).
- [19] D. Weller, H. Brändle, G. Gorman, C.-J. Lin, and H. Notarys, *Appl. Phys. Lett.* **61**, 2726 (1992).
- [20] D. Weller, H. Brändle, and C. Chappert, *J. Magn. Magn. Mat.* **121**, 461 (1993).
- [21] P. Pouloupoulos, M. Angelakeris, E. T. Papaioannou, N. K. Flevaris, D. Niarchos, M. Nyvlt, V. Prosser, S. Visnovsky, C. Mueller, P. Fumagalli, et al., *J. Appl. Phys.* **94**, 7662 (2003).
- [22] H. Sato, T. Shimatsu, Y. Okazaki, H. Muraoka, H. Aoi, S. Okamoto, and O. Kitakami, *J. Appl. Phys.* **103**, 07E114 (2008).
- [23] J. M. Sanchez, J. L. Moran-Lopez, C. Leroux, and M. C. Cadeville, *J. Phys. C* **21**, L1091 (1988).
- [24] P. Gambardella, S. Rusponi, M. Veronese, S. S. Dhesi, C. Grazioli, A. Dallmeyer, I. Cabria, R. Zeller, P. H. Dederichs, K. Kern, et al., *Science* **300**, 1130 (2003).
- [25] M. Sakamaki, K. Amemiya, M. O. Liedke, J. Fassbender, P. Mazalski, I. Sveklo, and A. Maziewski, *Phys. Rev. B* **86**, 024418 (2012).





## APPENDIX A

---

### Analysis of magneto-optical images

---

The spatially-resolved hysteresis measurements using the Kerr microscope require a complicated analysis to obtain valuable physical information. To make quantitative analysis possible, some steps should be taken at the stage of performing the experiment. Every single picture, taken at a certain magnetic field value  $H$ , should be accompanied by two pictures taken in the saturation state, i.e. within  $\pm H_{\max}$  – the maximal available field amplitude. The sequence of taking the images at  $H$ ,  $+H_{\max}$  and  $-H_{\max}$  is important to recover the magnetic history of the sample in every single step<sup>1</sup>. The crucial property of the reference images is that they all are taken in the same magnetic state of the sample and thus they are theoretically identical across the long process of recording the hysteresis loops (taking usually several minutes). By comparing how they change in reality, one can recognize and eliminate several effects that occur and perturb the measurements: a drift of the sample, a spatial inhomogeneity of the illumination, long-time fluctuations of the light intensity, and a direct influence of the magnetic field on the microscope objective.

The procedure of the analysis of magneto-optical images will be demonstrated using the images of the pulse laser-annealed sample #3, discussed in Chapter 5.

---

<sup>1</sup>see the discussions about hysteresis loops (Chapter 1.1), as well as about remanence images, (Chapter 3.3)

## A.1 Drift

Within the time of the single measurements the sample was found to drift quite significantly, in the order of several micrometers, i.e. comparably to the size of the annealed spots. Figure A.1 shows two reference images taken at the beginning (a) and at the end (b) of a sequence, as well as the difference between them (c), demonstrating the relevance of the problem.

The drift can be eliminated using a series of reference images. At first, one of the defects at the sample surface (visible as a black dot a speck of dust) is chosen and its position was determined for every image of the sequence. Tracing the position is realized by fitting the two-dimensional Gaussian surface to the selected area of every image (the orange frame in Figure A.1(a-c)). This way the path of drift can be found (Figure A.1(d)). For further processing, every image is being cropped in the manner defined by that path, to contain exactly the same region of the sample (the black-white dashed frames in Figure A.1(a,b)).

## A.2 Inhomogeneity of illumination

The light from a halogen lamp illuminates the sample spatially inhomogeneously – brighter at the center. Moreover, its intensity exhibits the tendency to fluctuate in the time domain. These changes happen relatively slowly and are small ( $\ll 1\%$ ), however the changes of the light intensity due to the Kerr rotation in the sample are supposed to be of the same order of magnitude, or even smaller.

Within the development of the theory of a Kerr microscope, presented in Chapter 3.3, one can involve also the mentioned temporal and spatial dependencies. The light intensity recorded at a certain pixel of coordinates  $(x, y)$  originates from:

- the intensity of the incident light,  $L(x, y, t)$ , dependent on position and time. We assume, that the variables can be separated into parts responsible for spatial inhomogeneities and temporal fluctuations:  $L(x, y, t) = P(x, y) \cdot T(t)$ ;
- the magneto-optical response,  $M(x, y, H)$  (discussed in Chapter 3), dependent on a position at the sample and the applied magnetic field.

The taken image can be expressed as:

$$I(x, y, t, H) = P(x, y) \cdot T(t) \cdot M(x, y, H). \quad (\text{A.1})$$

Assuming that a drift has been already corrected, as described in the previous Section, from the reasoning above the following observations can be made:

- every image of a sequence has an identical  $P(x, y)$ ;

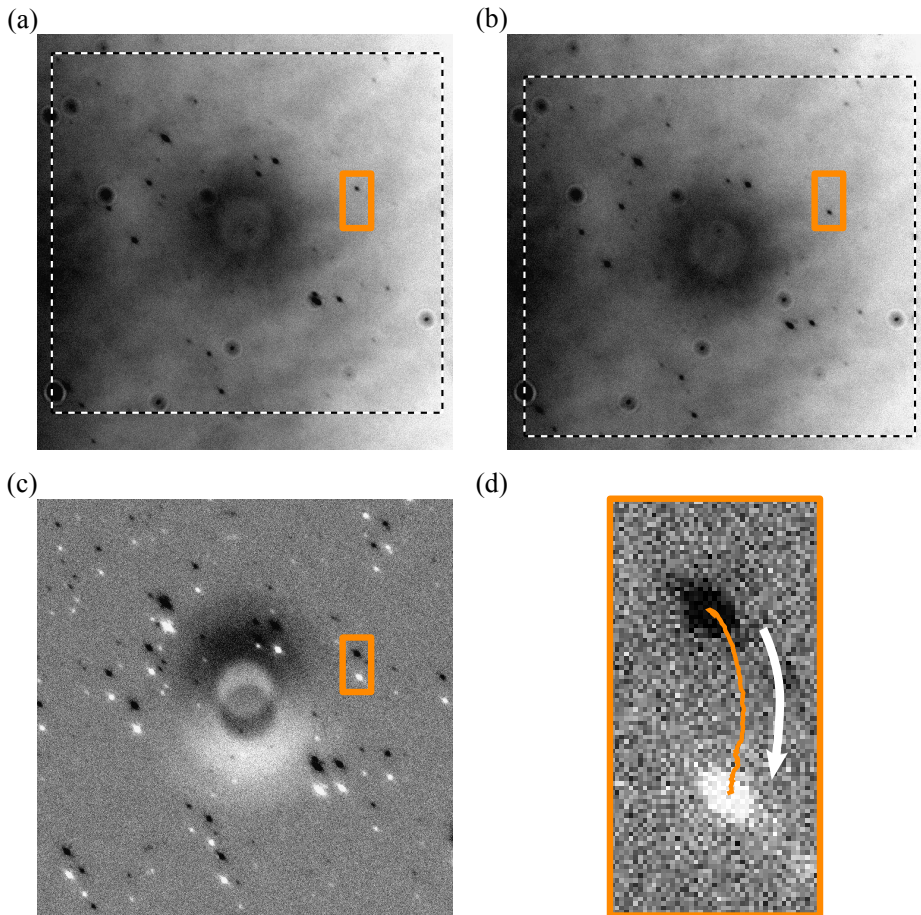


**Figure A.1:** (a, b): The two reference images taken at the same field  $-H_{\max}$  at the beginning and at the end of a sequence of the measurement; (c): the difference between these two images (gray scale was adjusted to keep a proper contrast). One of the defects (framed with the orange line; note, that some defects do not move, being connected rather with the optics or the CCD sensor) is used to follow the drift of the sample during the measurement. According to the found path (d), every image of the sequence is being cropped for further processing (the black-white dashed frames in (a) and (b)).

- as the temporal fluctuations are relatively slow, the neighboring images have practically the same  $T(t)$ ;
- all reference images, taken at the same field ( $+H_{\max}$  or  $-H_{\max}$ ), have identical  $M(x, y, \pm H_{\max})$ 's.

Thus, dividing one image by any other, the  $P(x, y)$  factor should vanish, and additionally dividing it by a neighboring one,  $T(t)$  should vanish too. To derive the magneto-optical contribution, a given image, taken at a certain field  $H$  was divided by the sum of the two accompanying reference images, taken at  $\pm H_{\max}$ . An example of such image processing is shown in Figure A.2.

At this stage, after the elimination of drift and inhomogeneities of the incident light, the set of images is ready to be converted into a set of hysteresis loops: light intensity, as a gray level recorded at a certain pixel of a given image, can be plotted as a function of the magnetic field that was applied during the taking of that image.

In the case of the analysis applied in Chapter 5, images of the 17 spots, of a size of about  $700 \times 700$  pixels, would yield about 8 million hysteresis loops. However, to treat a reasonable amount of data, profiles across annealed spots were analyzed only, as the laser-induced structure has a circular symmetry. Each profile was created by averaging the intensity over  $15 \times 1$ -pixels stripes (perpendicular to the direction of a taken profile). This way the number of loops was limited to about 12 thousands, without limiting the region of interest, moreover, improving significantly the quality of every single loop.

### A.3 Influence of magnetic field on microscope objective

Getting a higher magnification in a microscope requires a stronger microscope objective and usually a closer distance between the objective and the sample. It means also a closer distance between the objective and the electromagnet used for the experiment.

Although the electromagnet used in our experiment has been designed to produce a maximal field inside and a minimal field outside the poles (see Ref. [1]), the field outside was still high enough to affect the glass of the microscope objective. Paramagnetic glass reacts on the field with a Faraday effect. This means, that observed hysteresis loops contain two contributions: a Kerr rotation from the sample and a Faraday rotation from the glass objective. An example of a measured hysteresis loop, derived from gray levels of pixels of a certain area across a series of images taken in a magnetic field, is presented in Figure A.3(a).

To overcome the problem of the influence of the external magnetic field on the microscope objective, a following method is applied. As was mentioned, the exterior part of the images corresponds to a region beyond the area annealed by the laser pulse, i.e. a not modified structure. As the sample was initially characterized with a PMOKE scan (Chapter 5.1), the shape of the hysteresis loops is already known

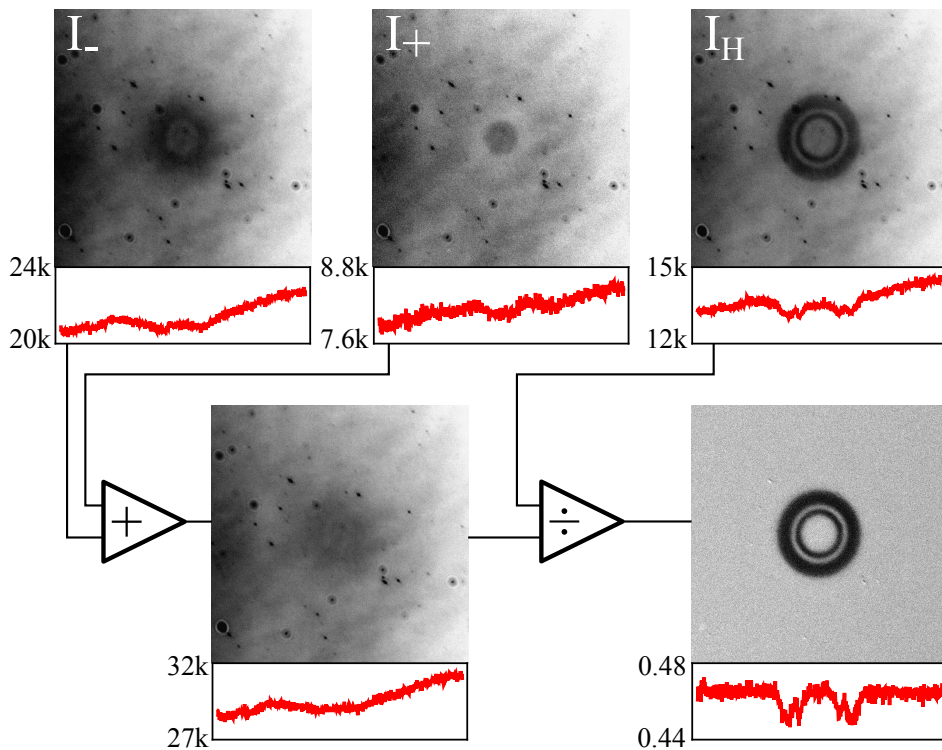


**Figure A.2:** Image processing in order to eliminate spatial and temporal inhomogeneities of the incoming light intensity: image  $I_H$  (recorded at a certain field value  $H$ ) is divided by a sum of two reference images  $I_{\pm}$  (recorded at  $\pm H_{\max}$ ). Gray levels of each presented image were adjusted separately to keep reasonable contrasts. Below the images the profiles of the gray level along a horizontal line through the center of the image are plotted, with the scales (represented by minimal and maximal values) given at the left.

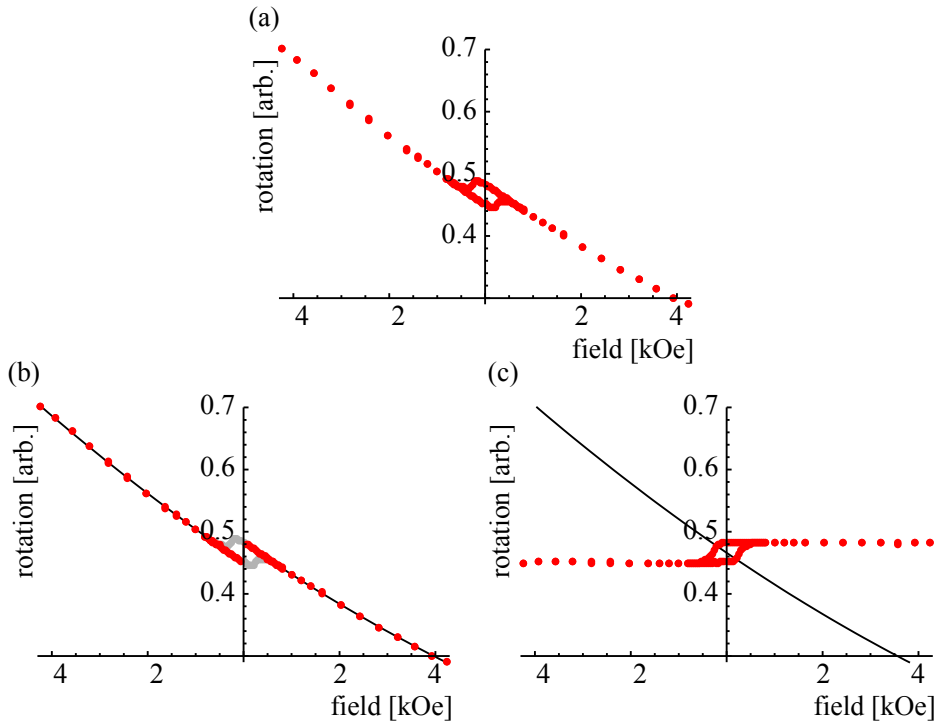


**Figure A.3:** (a) The hysteresis loop obtained for the exterior of the spot A5. The loop contains the ferromagnetic Kerr contribution from the sample and the paramagnetic Faraday contribution from the microscope objective's glass affected by the magnetic field; (b) the points marked in red were used to fit the parabolic function (Eq. (A.2)), in order to eliminate the glass contribution; black solid line: the found fit; (c) red points: the obtained hysteresis loop for the pure sample contribution (see footnote 2 on page 111); black solid line: the function that has been subtracted.

there. In particular, for the spots no. 5 and 9, the hysteresis loop is square, and above a relatively low saturation field the line is flat (see Figure 5.2). It means, that the change of rotation above the saturation field comes from the glass contribution only. The hysteresis loop shown in Figure A.3(a) comes from the exterior region of the spot A5. The paramagnetic contribution is visibly non-linear. The parabolic shape agrees well with our understanding of Eq. (3.9), where the recorded light intensity is proportional to the square of the polarization rotation angle (beyond the small angle approximation, Eq. (3.10)).

To get rid of a paramagnetic contribution, at first a parabolic function was fitted:

$$f(x) = ax^2 + bx + \begin{cases} c & \text{for } x < -x_0 \\ d & \text{for } x > +x_0 \end{cases} \quad (\text{A.2})$$

The data used in the fitting procedure is restricted to the points, about which we are sure of the squareness of the loop (the respective region was defined by the value of  $x_0$ ). For the cited example of the spot A5, that range corresponds to the red points in Figure A.3(b). In this Figure the found fit is also displayed as a black solid line. Finally, the parabolic function  $ax^2 + bx + |c + d|/2$  (i.e. Eq. (A.2), averaged over the two branches) with the found values of the parameters ( $a$ ,  $b$ ,  $c$  and  $d$ ) was subtracted from the data, to obtain a pure Kerr contribution, with the influence of the magnetic field on the optics eliminated. Figure A.3(c) shows the obtained hysteresis loop<sup>2</sup> (red points) as well as the parabolic curve that has been subtracted (black solid line).

The parabolic fit, found for the limited squared-loop-region of the spot image, was applied afterward to eliminate the paramagnetic contribution in all curves for the given spot (assuming a homogeneous Faraday response of glass). Such procedure was repeated for all studied spots, however the regions of square loops were different for different spots. In particular, for the spots above the SRT (columns 13, 17 and 21) the square-loop-region corresponds to the laser-induced rings, visible as bright in the remanence images.

## References

- [1] D. Lukáš, K. Postava, O. Životský, and J. Pištora, *J. Magn. Magn. Mat.* **322**, 1471 (2010), proceedings of the Joint European Magnetic Symposia.

---

<sup>2</sup>For the sake of clarity of that Figure, the hysteresis loop shown here was obtained by subtracting from the original data the  $(ax^2 + bx)$  term only. Subtracting the full form  $ax^2 + bx + |c + d|/2$  yields the loop that is centered vertically at 0.





## APPENDIX B

---

### Beam size determination

---

Determining the beam size is crucial for finding the energy density within the laser pulse, necessary to describe the thermally induced changes of the magnetic anisotropy (Chapter 4), as well as the structural modification by laser pulses (Chapter 5). The procedure will be demonstrated using the data obtained for the pulse laser-annealed sample #3 (Chapter 5).

The spatial distribution of the energy density (energy per area unit)<sup>1</sup> of a laser beam can be described with the two-dimensional Gaussian shape:

$$I(x, y) = I_0 e^{-(x^2+y^2)/r_0^2}. \quad (\text{B.1})$$

The integral of Eq. (B.1) over space yields the total energy of a pulse:

$$E = I_0 \pi r_0^2. \quad (\text{B.2})$$

The radius  $r_0$  of the annealing laser beam can be determined using two techniques: the Liu's method [1] and the knife-edge method [2, 3].

### B.1 Liu's method

In this method it is assumed that some threshold energy density  $I_t$  is required to induce a phase transformation in a material. As the energy density changes spatially

---

<sup>1</sup> *SI*-units for  $I$  are  $\text{J}/\text{m}^2$  or, traditionally,  $\text{mJ}/\text{cm}^2$ .

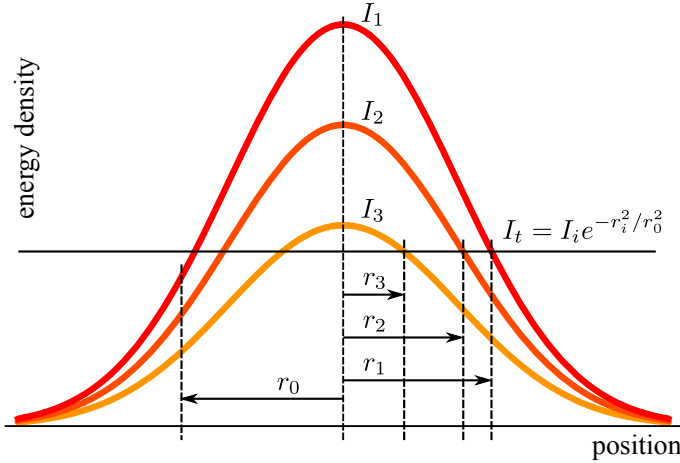


**Figure B.1:** Application of the Liu's method. For  $I_i$  ( $i = 1, 2, 3$ ), the energy density  $I_t$ , necessary to induce some changes in a material, is reached inside a circle of a radius  $r_i$ .

within a laser pulse according to the two-dimensional Gaussian shape (Eq. (B.1)), inside a circle of a certain threshold radius  $r_t$  the energy is high enough to induce that transformation:

$$I_t = I_0 e^{-r_t^2/r_0^2}. \quad (\text{B.3})$$

The laser pulses with different  $I_0$  result in different radii of the modified area. This is demonstrated in Figure B.1. Eq. (B.3) can be rewritten in the form:

$$\log I_0 = \frac{r_t^2}{r_0^2} + \log I_t. \quad (\text{B.4})$$

According to this formula, the experimental dependence of  $r_t^2$  vs.  $\log I_0$  is a linear function, which can be used for determining  $r_0$  and  $I_t$ . Values of  $r_t$  are measurable; values of  $I_0$  in our case are unknown, however in order to determine  $r_0$  only, any arbitrary unit of energy can be used instead, particularly the measured total pulse energy (which is proportional to  $I_0$ )<sup>2</sup>.

All laser-induced dark and bright rings and disks (see Figure 5.9) have been treated as separate structures, that require a certain threshold energy density for their creation. The respective radii have been determined for several spots of various pulse energies and Co thicknesses. All studied dependences  $r_t^2$  vs.  $\log I_0$ , according to Eq. (B.4), are plotted in Figure B.2. The remanence image of an exemplary spot

<sup>2</sup>As a logarithm of  $I_0$  is used in Eq. (B.4), multiplying  $I_0$  by any arbitrary number only shifts the linear dependence ( $\log ab = \log a + \log b$ ), whose gradient is only important for determining  $r_0$ .

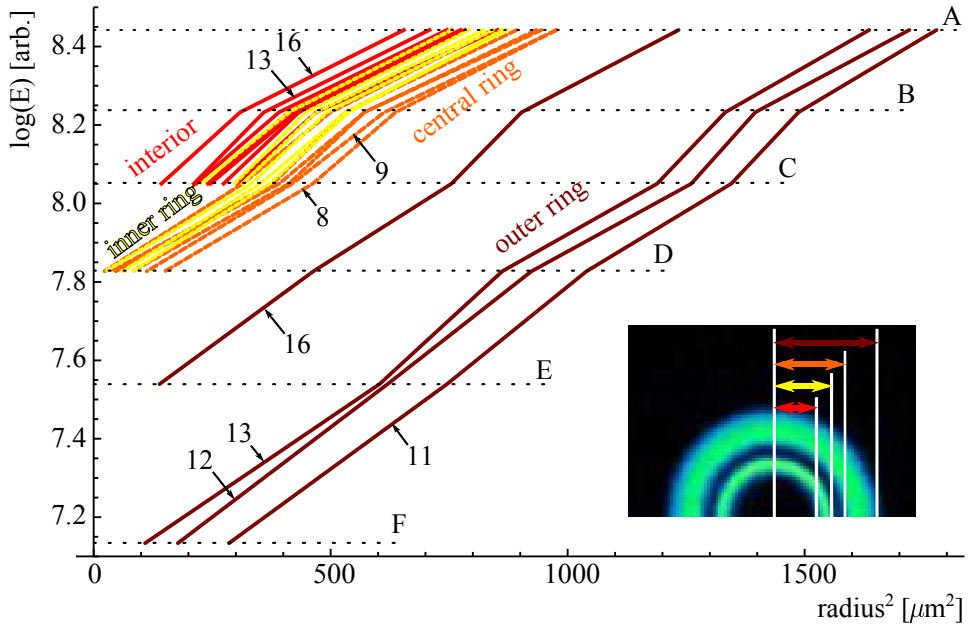


**Figure B.2:** The measured dependencies  $r_t^2$  vs.  $\log I_0$ , determined for several selected spots. Each line has been taken from one series of spots of constant Co thickness (columns). The constant pulse energies (rows) are represented by horizontal dotted lines A–F. Colors denote the respective types of laser-induced structures: brown - the outer ring, orange - the central ring, yellow - the inner ring and red - the interior.

(C17), with relevant radii marked with different colors, is also presented. The threshold energy density is obviously different for each type of dark-bright area transition, and it also varies with the Co thickness. The beam radius, represented by the gradient, is kept constant for all dependencies. From the linear fits to all presented data, a value of  $r_0 = (34.2 \pm 0.6)\mu\text{m}$  has been determined.

## B.2 Knife-edge method

The knife-edge method can be also employed to measure the beam radius. A blade, placed at the focus of the lens (at the position where the sample has been placed) and eclipsing partially the beam, is moved in the direction perpendicular to the beam with a micrometer screw. The intensity of the light that passes is measured with a power meter, as a function of the blade position. The scheme of this experiment is presented in Figure B.3.

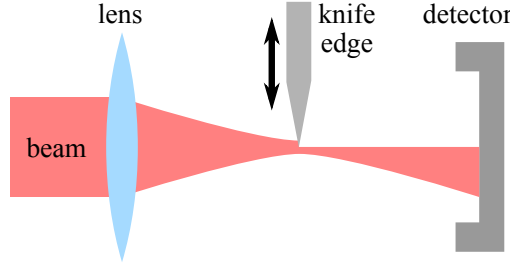


**Figure B.3:** The idea of the knife-edge method. The blade moves perpendicularly to the beam, to eclipse partially the beam. The intensity of the light is measured as a function of the blade position.

Mathematically, the energy measured by a detector after the edge, that partially eclipses the beam, is an integral of the Gaussian shape of the energy density (Eq. (B.1)) over a half-plane, limited by  $x$ , the position of the blade<sup>3</sup>:

$$E(x) = \int_{-\infty}^x \int_{-\infty}^{+\infty} I(x', y) dy dx'. \quad (\text{B.5})$$

The result of that integration, after normalization (marked with an index  $N$ ) is a sigmoid function:

$$E_N(x) = \frac{1}{2} \left( 1 + \operatorname{erf} \left( \frac{x}{r_0} \right) \right). \quad (\text{B.6})$$

$\operatorname{erf}$  is the error function, which is not analytical, which makes it unpractical for fitting procedures. Following the approach proposed by Khosroffian and Garetz [2], it can be replaced by an analytical approximation:

$$E_N(x) \approx \left( 1 + \exp \sum_i a_i s^i \right)^{-1}, \quad (\text{B.7})$$

with

$$s = \sqrt{2} \frac{x}{r_0}. \quad (\text{B.8})$$

Values of the phenomenological parameters  $a_i$ , that reproduce Eq. (B.6) better than the ones proposed originally by Khosroffian and Garetz, were determined by de Araújo et al. [3]:  $a_1 = -1.597106847$ ,  $a_3 = -7.0924013 \times 10^{-2}$ , with zeros for the rest of the  $a_i$ 's. For practical reason  $x$  in the above equations is replaced by  $(x - x_0)$ , as the blade position is arbitrarily shifted with some  $x_0$  with respect to the center of the beam.

<sup>3</sup>For the sake of convenience, the variable  $r$  was converted into the pair  $(x, y)$ , using  $r^2 = x^2 + y^2$ .

The measured dependence of the light intensity on the knife-edge position, shown as black points in Figure B.4(b), was fitted using Eq. (B.7), but unfortunately, the found curve did not reproduce the measured points with satisfactory accuracy, and the obtained value of  $r_0 = 58 \mu\text{m}$  is far from the one found with the Liu's method. It means, that apparently the beam does not satisfy a single Gaussian shape. Slow changes of the measured energy with the edge position within the peripheral points may indicate a kind of background, coming for instance from imperfections of the optics causing extra reflections. That background can be approximated by another Gaussian profile, of much bigger radius and a smaller intensity. The new energy density profile would be composed then of two Gaussian profiles:

$$I'(x, y) = aI_0e^{-(x^2+y^2)/r_1^2} + (1-a)I_0e^{-(x^2+y^2)/r_2^2}. \quad (\text{B.9})$$

The energy dependence, measured with the knife-edge method, would also contain two contributions:

$$E'_N(x) = bE_N(x, r_1) + (1-b)E_N(x, r_2). \quad (\text{B.10})$$

The parameters  $a$  and  $b$  are not the same, as  $a$  defines the contribution to the energy density, but  $b$  the contribution to the integral of the energy density (i.e. to the total energy). According to Eq. (B.2), both contributions to the total energy are:

$$\begin{aligned} E_1 &= aI_0\pi r_1^2 \\ E_2 &= (1-a)I_0\pi r_2^2 \end{aligned} \quad (\text{B.11})$$

Thus, the relation between  $a$  and  $b$ , normalizing  $b$  to 1, is:

$$b = \frac{ar_1^2}{ar_1^2 + (1-a)r_2^2}. \quad (\text{B.12})$$

Within the previously described Liu's method a single Gaussian profile was assumed. However, the data (the sizes of the rings and disks) came from a relatively narrow range of radii of about 5–40  $\mu\text{m}$  (see the horizontal axis in Figure B.2), so rather the central than the peripheral part of the profile was probed. To make both methods consistent, the double Gaussian profile should follow closely the single one with the previously found  $r_0 = 34.2 \mu\text{m}$ , in the range up to 40  $\mu\text{m}$ . This restriction was kept in the fitting procedure by controlling the “effective” width of the double Gaussian distribution (i.e. the distance of  $1/e$ -drop). This way the values of  $r_1 = (33.8 \pm 0.5)\mu\text{m}$ ,  $r_2 = (217 \pm 21)\mu\text{m}$  and  $a = (98.6 \pm 0.4)\%$  were found. The obtained energy density profiles are displayed in Figure B.4(a). The background component may seem to be irrelevant, however due to its large radius  $r_2$  it contributes significantly to the energy – according to Eq. (B.12),  $b$  is only 64%. In Figure B.4(b) both components to the energy, as a function of the blade position, are shown, as well as their sum, that was

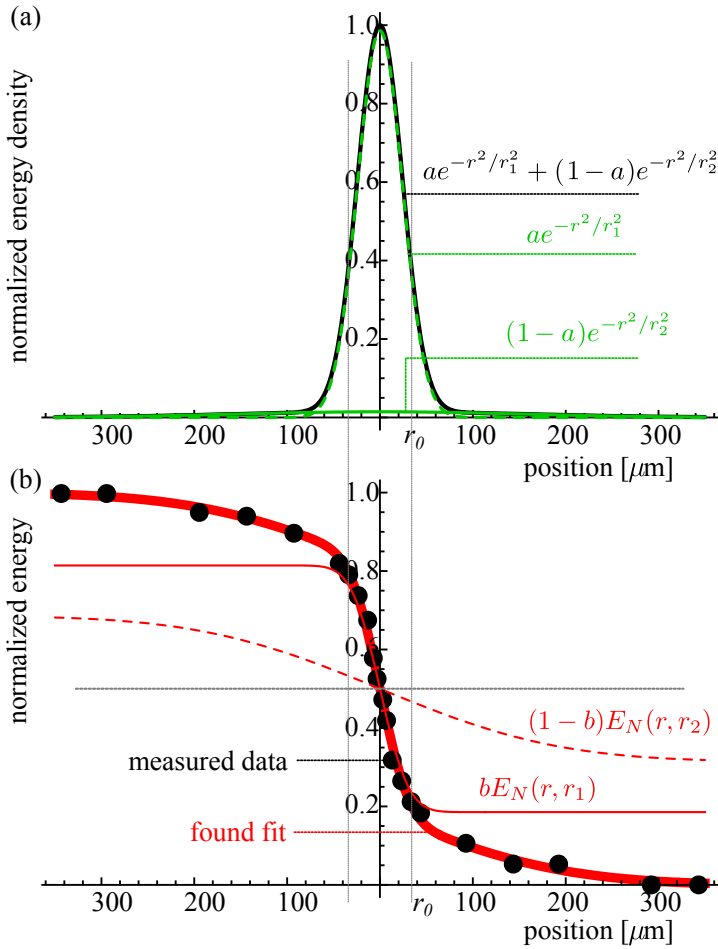


**Figure B.4:** (a) Double-Gaussian energy density profile (solid black line); two components are displayed with green lines; (b) the found fit within the knife-edge method, using a double Gaussian beam profile (thick red line) and the measured data (black points); two contributions are displayed with red thin lines; for better clarity they are shifted vertically and centered at 0.5.

used in the fitting procedure. The agreement with the experimental points is visibly good.

To calculate the amplitude of the energy density  $I_0$ , both Gaussian components are taken into account. The total pulse energy  $E$  measured in the experiment is a sum of  $E_1$  and  $E_2$  from Eqs. (B.11), and thus from these equations we can derive  $I_0$ :

$$I_0 = \frac{E}{\pi(ar_1^2 + (1-a)r_2^2)}. \quad (\text{B.13})$$

## References

- [1] J. M. Liu, *Opt. Lett.* **7**, 196 (1982).
- [2] J. M. Khosrofian and B. A. Garetz, *Appl. Opt.* **22**, 3406 (1983).
- [3] M. A. C. de Araújo, R. Silva, E. de Lima, D. P. Pereira, and P. C. de Oliveira, *Appl. Opt.* **48**, 393 (2009).





---

## Calculations of laser-induced temperature dynamics

---

The calculations of the laser-induced temperature dynamics in ultrathin films can be performed relatively easily within the one-temperature model (1TM), not taking into account the separate electron and lattice (and spin) baths described by the two/three-temperature model. Nevertheless, the 1TM involves a serious restriction, that limits its validity. In this model electrons, lattice and spins have one common temperature, which is not true for ultrafast heating processes that happen on a time scale below single picoseconds (see Chapter 1.1.2). For the longer time scales, after the thermalization of the three mentioned baths, both the 1TM and 2TM/3TM produce consistent results. For this Thesis, we will not be concerned with the ultrafast temperature dynamics active on the sub-picosecond time scale. Instead, we will investigate in detail how an absorbed laser pulse energy will affect the temperature distribution in a multilayer thin film structure.

General steps of the calculations are the following: at first, the amount of absorbed energy, deposited with a laser pulse, is calculated, as a function of position and depth in a sample. Within the next step, this energy is converted into a temperature increase, assuming immediate conversion (neglecting the real heating process that takes a few picoseconds). Such assumption is valid for ultrashort laser pulses only (shorter than a few picoseconds). Finally, using a standard heat equation, the heat flow and the cooling process are considered. The presented model does not take into account the heat accumulation, so it is not applicable for *CW* heating, which in fact is much more complicated to calculate. As an example, the calculation procedure will be demonstrated for the sample studied in Chapter 4.

## C.1 Absorbed energy

The laser light penetrates a metallic structure several tens of nanometer deep, being absorbed and also reflected from the interfaces. To describe this process in detail, usually a standard matrix method is applied, which in its general form for magneto-optical media is presented in Refs. [1–4]. In this case we consider the normal angle of incidence, and as a result, a depth-profile of the light intensity is obtained, calculated as  $\varepsilon(z) = |E_x(z)|^2 + |E_y(z)|^2$  ( $E_{x,y}$  are amplitudes of the eigenwaves of orthogonal polarizations at certain depth  $z$ ). Due to the cylindrical symmetry, for further calculations we use a two-dimensional  $(r, z)$  coordinate system. In this system  $\varepsilon$  is a function of the depth  $z$  only. Within the matrix formalism an incident intensity is normalized to 1, thus  $\varepsilon(z < 0) = 1$ . An example of  $\varepsilon(z)$  calculated for the sample studied in Chapter 4, for the Co thickness of 2 nm, is shown in Figure C.1.

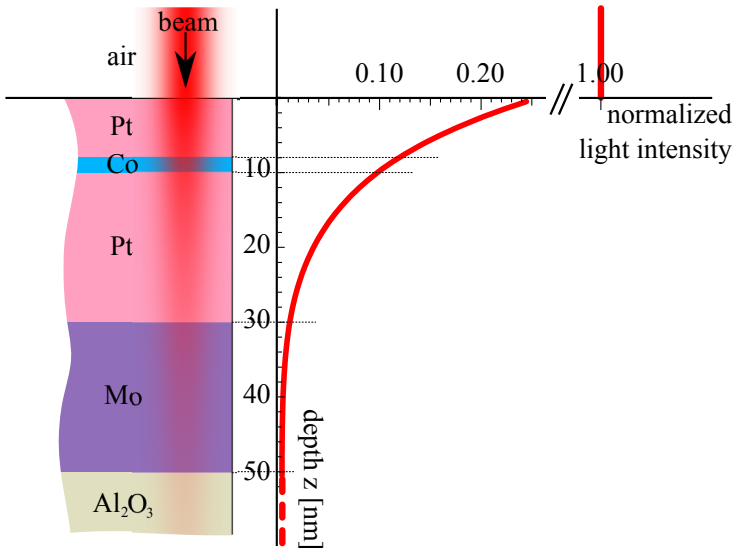


**Figure C.1:** The depth-profile of the light intensity, calculated with a standard matrix method.

A spatial energy density distribution (energy per area unit) is usually described with a two-dimensional Gaussian profile (see Chapter 5.4.4 and Appendix B). Hence in our coordinate system:

$$I(r, z < 0) = I_0 e^{-r^2/r_0^2}. \quad (\text{C.1})$$

The dependence of the volume energy density in material (for  $z > 0$ ) is:

$$D(r, z) = \varepsilon(z) \cdot I(r) \cdot n(z) \cdot \frac{1}{dz}, \quad (\text{C.2})$$

where  $n$  is the real part of the refractive index (determining the “density” of an electromagnetic wave in a material),  $dz$  is an element of a thickness. Units of  $D$  are  $\text{J}/\text{m}^3$ . Employing an absorption coefficient

$$\alpha(z) = \frac{4\pi}{\lambda_0} k(z), \quad (\text{C.3})$$

with a wavelength in vacuum  $\lambda_0$  and an imaginary part of the refractive index  $k$  (the extinction coefficient), the volume energy density, that is absorbed in element  $dz$  is<sup>1</sup>:

$$A(r, z) = D(r, z) - D(r, z + dz) = D(r, z) \cdot \alpha(z) \cdot dz. \quad (\text{C.4})$$

Summarizing,

$$A(r, z) = \varepsilon(z) I(r) n(z) \frac{4\pi}{\lambda_0} k(z). \quad (\text{C.5})$$

## C.2 Temperature increase

The absorbed volume energy density  $A(r, z)$  is assumed to be converted into heat at a certain position of the sample. For small energies, a simple formula for the temperature increase with the specific heat  $C$  can be used<sup>2</sup>:

$$\Delta T(r, z) = \frac{A(r, z)}{C(z)}, \quad (\text{C.6})$$

The term “small energies” means a temperature increase which is small enough to assume a constant specific heat – in this approximation  $C$  is temperature-independent. For higher energies the temperature changes of  $C$  become relevant, and then the experimental tables of standard enthalpy can be used instead. This enthalpy determines the energy per unit volume of matter, related to its temperature – in our case we just need to invert that function. It automatically includes the  $C(T)$  dependence (as a gradient of the curve), as well as all phase transitions. The data for the calculations was taken from Refs. [5–7]. An example of such curve for Co is shown in Figure C.2.

Figure C.3 shows the initial temperature increase occurring in the sample, heating with the laser pulse. The calculations were performed for the Co thickness of 2 nm and the energy density of 2.6  $\text{mJ}/\text{cm}^2$ , used in the experiment (see Chapter 4). The

<sup>1</sup> $D(z) - D(z + dz) = D(z) (1 - e^{-\alpha(z)dz}) \simeq D(z)\alpha(z)dz.$

<sup>2</sup>For this formula the specific heat should be expressed in units of *energy per volume per temperature*, e.g.  $\text{Jm}^{-3}\text{K}^{-1}$ .

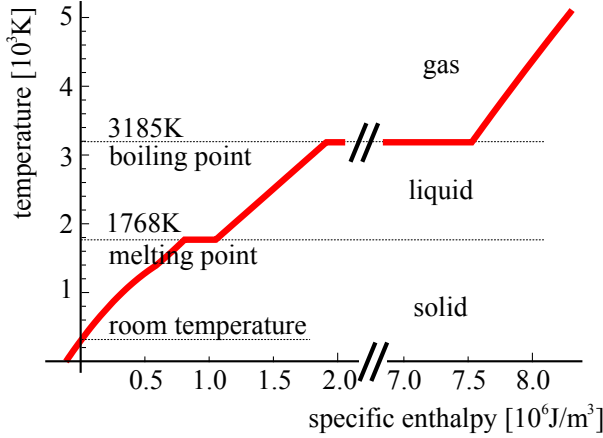


**Figure C.2:** An example of the inverted temperature vs. standard enthalpy dependence for Co, related to the room temperature value. The data was taken from Ref. [5].

curve is broken at the various interfaces due to the different specific heats for the constituent layers. However, this is a specific property of the 1TM. In reality the steps are not infinitely sharp, as the heating takes some time and involves interaction between the baths, and meanwhile between the neighboring layers.

### C.3 Heat equation

In the next step, there is no more pumping of energy by the laser pulse and the layers are assumed to thermalize with each other. The general form of the heat equation, for isotropic media, without any external heat sources, is:

$$\frac{dT}{dt} = \kappa \nabla^2 T, \quad (\text{C.7})$$

where

$$\kappa = \frac{\tau}{C} \quad (\text{C.8})$$

is called the thermal diffusivity, with the thermal conductivity  $\tau$  and the specific heat  $C$ . In our three-dimensional case with cylindrical symmetry the heat equation becomes more complicated:

$$\frac{\partial T(r, z, t)}{\partial t} = \frac{1}{C(z)} \left[ \tau(z) \left( \frac{\partial^2}{\partial r^2} + \frac{1}{r} \frac{\partial}{\partial r} + \frac{\partial^2}{\partial z^2} \right) T(r, z, t) + \frac{\partial \tau(z)}{\partial z} \frac{\partial T(r, z, t)}{\partial z} \right]. \quad (\text{C.9})$$

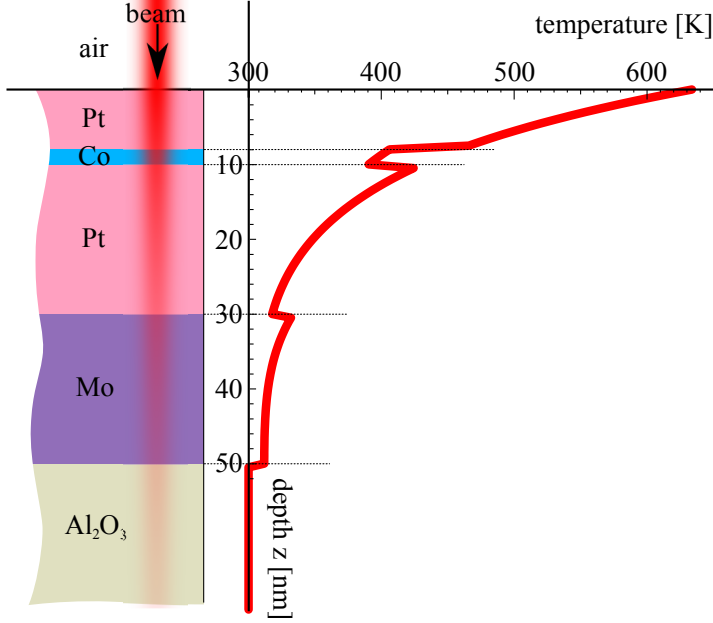


**Figure C.3:** The initial temperature depth-profile of the sample heated with ultrashort laser pulse of the energy density of  $2.6 \text{ mJ/cm}^2$ , calculated with the 1TM.

The heat equation is solved numerically, with all the variables  $(r, z, t)$  quantized, with reasonable  $\Delta r$ ,  $\Delta z$  and  $\Delta t$  values. Two special cases can be distinguished: perpendicular and planar heat transfer.

### C.3.1 Perpendicular heat transfer

It is assumed that the sample is an infinite plane, with planarly homogeneous initial temperature increase. It means, that

$$T(r, z, t) = T(z, t), \quad (\text{C.10})$$

i.e. there is no planar heat transfer, so Eq. (C.9) can be rewritten in a simpler form:

$$\frac{\partial T(z, t)}{\partial t} = \frac{1}{C(z)} \left[ \tau(z) \frac{\partial^2 T(z, t)}{\partial z^2} + \frac{\partial \tau(z)}{\partial z} \frac{\partial T(z, t)}{\partial z} \right]. \quad (\text{C.11})$$

For the structure of the mentioned sample, a depth-profile of the temperature would vary in the manner shown in Figure C.4. According to the calculations, the temperature is supposed to equilibrate on a few picosecond time scale. After about

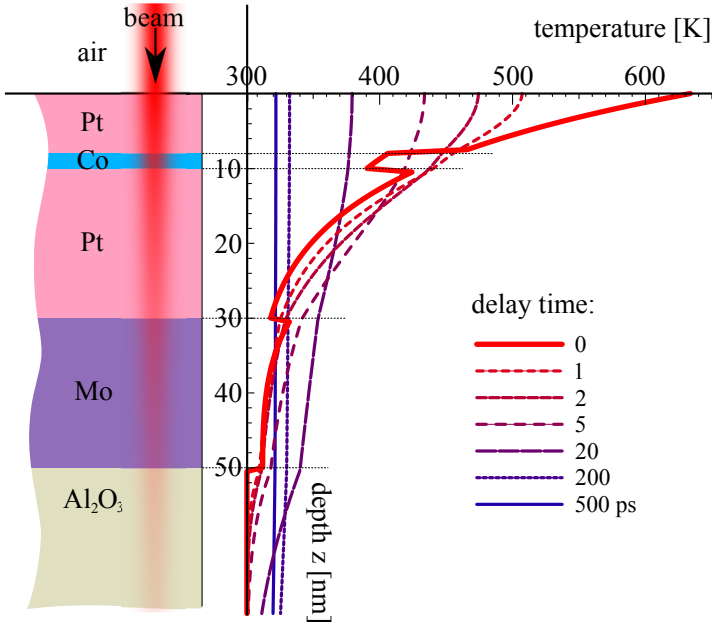


**Figure C.4:** The temperature depth-profiles for selected time delays after the heating laser pulse of  $2.6 \text{ mJ/cm}^2$ , calculated with the 1TM.

20 ps it equalizes in all metallic layers and then the sample cools down homogeneously in several hundreds picoseconds, due to the heat transfer to the substrate.

### C.3.2 Planar heat transfer

Now the sample is assumed to be an infinite plane as well, with a certain planar and depth-independent initial temperature distribution:

$$T(r, z, t) = T(r, t). \quad (\text{C.12})$$

The plane is isolated, so there is no perpendicular heat transfer to the substrate. The heat equation takes a simpler form again:

$$\frac{\partial T(r, t)}{\partial t} = \frac{\tau}{C} \left( \frac{\partial^2}{\partial r^2} + \frac{1}{r} \frac{\partial}{\partial r} \right) T(r, t). \quad (\text{C.13})$$

As an initial profile of a temperature increase the Gaussian profile was taken<sup>3</sup>, with an exemplary amplitude of 100 K and a radius of 30  $\mu\text{m}$  (i.e. the experimental value of the pump beam radius in Chapter 4). Values of thermodynamic constants were averaged over the ones for the constituent materials. The results of calculations are shown in Figure C.5. A typical time scale of such dynamics is several tens of microseconds.

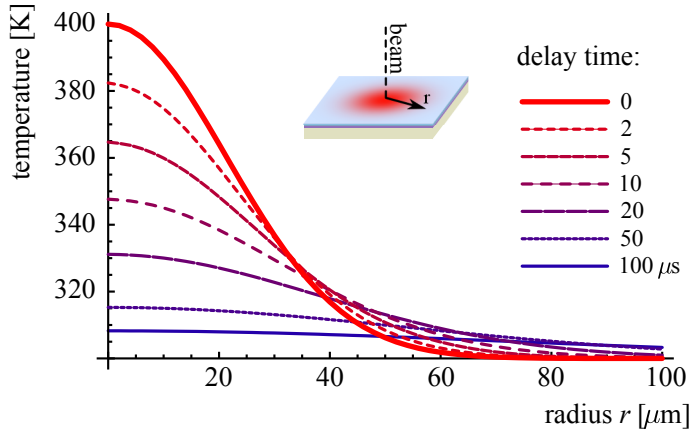


**Figure C.5:** The radial temperature profiles in metallic layers, for selected time delays after the heating laser pulse, calculated with 1TM.

However, the rate of temperature drop depends strongly on the width of the initial temperature distribution. The dependence, as was checked numerically, is a quadratic function, i.e. reducing the width twice, the changes are four time faster.

In real samples both processes, the perpendicular and the planar heat transfer, occur simultaneously. Nevertheless, for most cases, unless the beam size is reduced to sub-micrometer size, the planar heat transfer happens much more slowly, and thus usually can be neglected.

## References

- [1] P. Yeh, Surf. Sci. **96**, 41 (1980).
- [2] Š. Višňovský, Czech. J. Phys. **36**, 625 (1986).
- [3] Š. Višňovský, Czech. J. Phys. **41**, 663 (1991).
- [4] M. Nyvlt, Ph.D. thesis, Charles University, Prague (1996).

<sup>3</sup>In an approximation of  $C(T) = \text{const.}$  the temperature profile has the same shape as the energy density.

- [5] M. W. Chase, *NIST-JANAF Thermochemical Tables, Fourth Edition, J. Phys. Chem. Ref. Data, Monograph 9* (1998).
- [6] *NIST-JANAF thermochemical tables*, URL <http://kinetics.nist.gov/janaf/>.
- [7] *Research Information Database of National Institute of Advanced Industrial Science and Technology*, URL <http://riodb.ibase.aist.go.jp/>.



---

## Summary

---

Magnetic materials are extensively applied in various magnetic devices, like memories or sensors. Properties of these materials, both statics and dynamics, are ruled by the magnetic anisotropy. The challenge is to be able to modify the magnetic anisotropy in order to get a material of desired properties, suitable for applications.

This Thesis treated some possibilities of controlling the magnetic anisotropy. After the introductory Chapter 1, which explained the basic ideas of the magnetization and the magnetic anisotropy, in Chapter 2 a review of well-known techniques of tuning the magnetic anisotropy in ultrathin metallic layers was given. Even at the stage of sample preparation, the magnetic properties are strongly influenced by the chosen method of production, the type and structure of the substrate, buffer and cover layers, as well as the conditions during growth. Among the methods of treatment of already-prepared samples, we distinguished ones leading either to reversible or irreversible modifications of the magnetic anisotropy.

The experimental part of this Thesis was divided into two parts, devoted to reversible and irreversible modifications. In both cases, similar ultrathin Pt/Co/Pt systems were considered, and the laser irradiation was the factor, whose influence on magnetic properties was studied. Experimental methods used in the frame of the Thesis were presented in Chapter 3. All of them were based on the magneto-optical Kerr effect, which is a very powerful and universal tool to probe magnetic properties, from statics to ultrafast dynamics.

In Chapter 4 the reversible modification of the magnetic anisotropy was discussed. Illuminating a sample with ultrashort laser pulses of relatively low energy densities, a precession of the magnetization was found to occur. Amplitude and frequency of this precession was strongly dependent on the Co layer thickness and the amplitude

of the externally applied magnetic field. This dependence was successfully explained with a simple model, which involved the laser-induced temperature increase, while the thermal changes of the effective anisotropy field was considered as a mechanism of triggering the precession. Using this model, we also answered a question concerning the thermal behavior of the surface contribution to the anisotropy. Moreover, as the model is quite universal, it can be potentially used for the determination of other magnetic or thermodynamic parameters of magnetic materials.

Increasing the fluence of the laser pulses, at a certain point the energy density is high enough to bring some irreversible changes of the structure, via interdiffusion and mixing at the interfaces of the multilayer samples. The effect of such laser-annealing was studied in Chapter 5. Together with structural modifications, permanent changes of the magnetic anisotropy were observed. Particularly, the out-of-plane magnetization state was found to be created for Co thicknesses, where normally the in-plane phase occurs. These light-induced changes happen locally, limited to a few-micrometers area of a certain energy density of the focused light beam, and ultrafast – after a single 60 fs laser pulse. This opens a unique opportunity of producing perpendicularly magnetized nanostructures, with relatively simple methods – using the light.

---

## Samenvatting

---

Magnetische materialen worden veelvuldig toegepast in diverse magnetische apparaten, zoals geheugens of sensoren. De eigenschappen van deze materialen, zowel de statische als de dynamische, worden bepaald door de magnetische anisotropie. De uitdaging is om de anisotropie zo te manipuleren dat een materiaal met de gewenste eigenschappen wordt verkregen voor een specifieke toepassing.

Dit proefschrift behandelt een aantal mogelijkheden om de magnetische anisotropie te manipuleren. Na het inleidende hoofdstuk 1, waar de basis ideeën van magnetisatie en de magnetische anisotropie wordt uitgelegd, wordt in hoofdstuk 2 een overzicht gegeven van welbekende technieken waarmee de magnetische anisotropie van ultradunne metallische lagen kan worden veranderd. Zelfs op het moment van het maken van het preparaat, worden de magnetische eigenschappen ervan sterk beïnvloed door de gekozen productie methode, het type en de structuur van het substraat, de buffer- en afdekklagen en ook door de condities gedurende de groei. Onder de manipulatiemethodes voor preparaten die klaar zijn, maken we onderscheid tussen methodes die omkeerbare en niet omkeerbare veranderingen aanbrengen in de magnetische anisotropie.

Het experimentele deel van dit proefschrift is in twee stukken verdeeld, welke toegewijd waren aan omkeerbare en niet omkeerbare veranderingen in de anisotropie. In beide gevallen werden vergelijkbare systemen van ultradunne Pt/Co/Pt beschouwd, en werd de invloed van laser bestraling op de magnetische eigenschappen bestudeerd. De experimentele methoden die in dit proefschrift zijn gebruikt werden gepresenteerd in hoofdstuk 3. Allen waren gebaseerd op het magneto-optisch Kerr effect. Dit is een erg krachtig en universeel effect waarmee zowel statische als dynamische magnetische eigenschappen gemeten kunnen worden.

In hoofdstuk 4 werd de omkeerbare verandering van de magnetische anisotropie behandeld. Na de belichting van het preparaat met ultra korte laser pulsen met een relatief lage energie dichtheid, is er een precessie van de magnetisatie waargenomen. De amplitude en frequentie van deze precessie hing sterk af van de Co laagdikte en de amplitude van het extern aangelegde magnetische veld. Deze afhankelijkheid kon succesvol worden verklaard met een eenvoudig model dat de laser geïnduceerde temperatuur verandering bevatte en welke de thermische veranderingen van het effectieve anisotropie veld beschouwde als een mechanisme om de precessie te starten. Gebruikmakend van dit model hebben we ook de vraag beantwoord over het thermische gedrag van de bijdrage van het oppervlak aan de anisotropie. Bovendien kan het model, aangezien het vrij universeel is, potentieel gebruikt worden voor het bepalen van andere magnetische of thermodynamische parameters van het materiaal.

Met toenemende laser intensiteit is de energie dichtheid op een gegeven moment hoog genoeg om onomkeerbare veranderingen in de structuur aan te brengen, door interdiffusie en menging bij de grenslagen. Het effect van deze laser-annealing is bestudeerd in hoofdstuk 5. Samen met een verandering van de structuur is er ook een permanente verandering van de magnetische anisotropie waargenomen. Voor Co lagen met een dikte waar normaal gesproken een in het vlak magnetisatie gevonden wordt, werd nu een uit het vlak magnetisatie waargenomen. Deze licht geïnduceerde veranderingen gebeuren lokaal, begrensd tot een gebied ter grootte van een paar micrometer dat wordt bepaald door de gefocuseerde laser straal, en ultra snel – na één enkele 60 fs laser puls. Dit opent een unieke mogelijkheid voor het produceren van loodrecht gemagnetiseerde nano structuren, gebruik makend van relatief eenvoudige methodes – werkend met licht.

Materiały magnetyczne są szeroko stosowane w różnych urządzeniach magnetycznych, takich jak pamięci lub czujniki. O właściwościach tych materiałów, zarówno statycznych jak i dynamicznych, decyduje anizotropia magnetyczna. Możliwość swobodnego modyfikowania anizotropii magnetycznej pozwoliłaby uzyskiwać dowolne materiały o właściwościach, na które byłoby zapotrzebowanie w danym urządzeniu.

W niniejszej Rozprawie opisane zostały sposoby modyfikacji anizotropii magnetycznej. Po Rozdziale 1, przedstawiającym podstawowe pojęcia związane z magnetyzmem, Rozdział 2 zawiera przegląd dobrze znanych technik, pozwalających na zmianę anizotropii w ultracienkich warstwach metalicznych. Już na etapie produkcji próbki, o właściwościach magnetycznych decyduje wybór metody preparacji, typ i struktura podłoża, warstwy buforowa i przykrywająca, a także w dużej mierze warunki w trakcie procesu wytwarzania. Metody, którymi można traktować już gotowe próbki, sklasyfikowane zostały na prowadzące do odwracalnych i nieodwracalnych zmian anizotropii magnetycznej.

Część doświadczalna Rozprawy również została podzielona na dwie części, poświęcone zmianom odwracalnym i nieodwracalnym. W obu przypadkach badane były podobne ultracienkie struktury Pt/Co/Pt, a czynnikiem, który wywoływał zmiany właściwości magnetycznych, było światło laserowe. Użyte techniki pomiarowe zostały przedstawione w Rozdziale 3. Wszystkie one bazowały na magneto-optycznym efekcie Kerra, który stanowi uniwersalne narzędzie do badania właściwości magnetycznych, od statyki po ultraszybką dynamikę.

W Rozdziale 4 badane były odwracalne zmiany anizotropii magnetycznej. Naświetlanie próbki za pomocą ultrakrótkich impulsów laserowych o względnie niskiej gęstości energii prowadziło do precesji namagnesowania. Amplituda i częstotliwość

precesji okazała się być silnie zależna od grubości warstwy kobaltu oraz od amplitudy zewnętrznego pola magnetycznego. Zależności te zostały opisane za pomocą prostego modelu, który zakłada zmianę temperatury próbki, wywołaną impulsem światła – nagle zmiana termiczna efektywnego pola anizotropii uruchamia precesję. Korzystając z przedstawionego modelu, udzielono odpowiedzi na pytanie dotyczące zależności od temperatury powierzchniowego wkładu do anizotropii. Z racji na swą uniwersalność, zaprezentowany model może być potencjalnie wykorzystywany do wyznaczania także innych parametrów magnetycznych czy termodynamicznych materiałów.

Zwiększając natężenie światła w impulsie laserowym, w pewnym momencie gęstość energii staje się wystarczająco duża, by wywołać zmiany nieodwracalne w strukturze próbki, polegające na dyfuzji atomów między sąsiednimi warstwami. Taki efekt wygrzewania laserowego został opisany w Rozdziale 5. Wraz z modyfikacją struktury, pojawiają się także trwałe zmiany anizotropii magnetycznej. W szczególności, w wyniku naświetlania została wyindukowana faza prostopadła namagnesowania, dla przedziału grubości kobaltu, dla których normalnie występuje faza płaszczyznowa. Zmiany te są lokalne, ograniczone do kilku-mikrometrowego obszaru, odpowiadającemu danej gęstości energii padającej skupionej wiązki laserowej, i następują już po naświetleniu pojedynczym impulsem o czasie trwania rzędu 60 fs. Zaobserwowany efekt otwiera nowe możliwości wytwarzania nanostruktur z namagnesowaniem prostopadłym, przy użyciu stosunkowo prostej techniki, jaką jest operowanie światłem.

---

## List of Publications

---

- [1] **J. Kisielewski**, W. Dobrogowski, Z. Kurant, A. Stupakiewicz, M. Tekielak, A. Kirilyuk, A. V. Kimel, T. Rasing, L. T. Baczewski, A. Wawro, and A. Maziewski, “Irreversible modification of magnetic properties of Pt/Co/Pt ultrathin films by femtosecond laser pulses,” (submitted).
- [2] **J. Kisielewski**, A. Kirilyuk, A. Stupakiewicz, A. Maziewski, A. Kimel, T. Rasing, L. T. Baczewski, and A. Wawro, “Laser-induced manipulation of magnetic anisotropy and magnetization precession in an ultrathin cobalt wedge,” *Physical Review B*, vol. 85, p. 184429, 2012.
- [3] **J. Kisielewski**, A. Maziewski, K. Postava, A. Stupakiewicz, A. Petroutchik, L. T. Baczewski, and A. Wawro, “Platinum overlayer-induced changes of magnetic and magneto-optical properties of ultrathin Co layer,” *Journal of Magnetism and Magnetic Materials*, vol. 322, pp. 1475–1477, 2010.
- [4] **J. Kisielewski**, K. Postava, I. Sveklo, A. Nedzved, P. Trzciński, A. Maziewski, B. Szymański, M. Urbaniak, and F. Stobiecki, “Magnetic anisotropy of Co films annealed by laser pulses,” *Solid State Phenomena*, vol. 140, pp. 69–74, 2008.
- [5] P. Kuświk, A. Ehresmann, M. Tekielak, B. Szymański, I. Sveklo, P. Mazalski, D. Engel, **J. Kisielewski**, D. Lengemann, M. Urbaniak, C. Schmidt, A. Maziewski, and F. Stobiecki, “Colloidal domain lithography for regularly arranged artificial magnetic out-of-plane monodomains in Au/Co/Au layers,” *Nanotechnology*, vol. 22, no. 9, p. 095302, 2011.
- [6] P. Kuświk, B. Szymański, M. Urbaniak, F. Stobiecki, I. Sveklo, **J. Kisielewski**, A. Maziewski, and J. Jagielski, “The influence of He<sup>+</sup> ion bombardment on

magnetic properties of NiFe/Au/Co/Au multilayers,” *Acta Physica Polonica A*, vol. 115, no. 1, pp. 352–354, 2009.

- [7] P. Kuświk, B. Szymański, M. Urbaniak, J. Dubowik, F. Stobiecki, **J. Kisielewski**, M. Tekielak, A. Maziewski, T. Weis, and A. Ehresmann, “He<sup>+</sup> ion bombardment induced effects on magnetic properties, of Ni-Fe/Au/Co/Au films,” *Acta Physica Polonica A*, vol. 113, no. 2, pp. 651–656, 2008.



---

## Curriculum Vitae

---

**Name:** Jan Kisielewski  
**Date of birth:** 15 April 1982  
**Place of birth:** Pruszków, Poland

- 1997–2001      Highschool, III Liceum Ogólnokształcące, Białystok, Poland
- 2001–2006      M.Sc. studies at Department of Physics, University of Białystok, Poland.
- 2006–            Research position at the Laboratory of Magnetism, University of Białystok, Poland, in the group of Prof. A. Maziewski
- 2009–2012      Ph.D. studies at Radboud University Nijmegen, The Netherlands, in the group of Prof. Th. Rasing